UNIVERSITY OF VERONA

DEPARTMENT OF MEDICINE

PhD in Inflammation, Immunity and Cancer

XXXV CYCLE

Malignant and fibroblast programs in aggressive PDAC molecular subtypes

S.S.D.MED\46

Coordinator: Prof. Vincenzo Corbo

Supervisor: Prof. Vincenzo Corbo

PhD Candidate: Dr. Lisa Veghini

ABSTRACT

Pancreatic Ductal Adenocarcinoma (PDAC) is the deadliest cancer worldwide. Late diagnosis and a complex biology make this a difficult-to-treat disease. PDAC displays extensive heterogeneity both in the malignant and non-malignant compartments. Of the non-malignant cells, cancer-associated fibroblasts (CAFs) are the most abundant cell type which critically influences tumour biology and response to treatments. The different PDAC cell states are shaped by the integration of cell intrinsic and cell extrinsic inputs. It is now well established that the transcriptional cell state (basal-like/squamous) displaying suppression of pancreatic endodermal gene programs has the most aggressive biological behaviour. Whether and how basal-like/squamous cells instruct the CAFs differently from the less aggressive classical phenotype remains to be elucidated. In this thesis work, we sought to disclose novel determinants of cell lineage specification as well as to identify subtype-specific stromal phenotypes. Receptor-Tyrosine Kinases (RTKs) are a large family of metazoan-specific plasma-membrane receptors that control several cellular processes including cell fate determination. Therefore, we focused on the potential role of RTKs in defining or sustaining aggressive molecular phenotypes of neoplastic cells. We found that the expression of *FGFR4* was significantly elevated in the classical PDAC subtype and associated with better outcomes. In highly aggressive basal-like/squamous PDAC, reduced *FGFR4* expression aligned with hypermethylation of the gene and lower levels of histone marks associated with active transcription in its regulatory regions. Regardless of the genetic background, the increased proliferation of FGFR4-depleted PDAC cells correlated with hyperactivation of the mTORC1 pathway both *in vitro* and *in vivo*. Downregulation of *FGFR4* in classical cell lines invariably led to the enrichment of basal-like/squamous gene programs and associated with either partial or full switch of phenotype. Whole-genome sequencing of advanced PDAC tissues and functional interrogation of organoid-based xenotransplantation have suggested RAS hyperactivation as a determinant of the basal-like/squamous subtype. Here, we used pathway mapping analysis and context-dependent pathway response signatures to infer MAPK activity and dependency in heterogeneous expression

data from models and patients' samples. *In situ* expression analyses complemented this approach, which undisclosed an important role for the MAPK signalling pathway in the definition of PDAC CAFs phenotypes. We found that the epithelial activity of MAPK did not discriminate basal-like from classical tumours. Conversely, hyperactivation of MAPK signalling occurred in myCAFs populating basal-like/squamous tumour niches. Short-term inhibition of MAPK was invariably associated with a dramatic change of the myCAFs/iCAFs ratio in mouse PDAC tissue due to a unique dependency of myCAF on a proficient MAPK signalling. Gene expression signatures of MAPK^{high} CAFs (sMEK) from mouse tumours suggested metabolic rewiring and immunoregulatory function. Finally, we found that the sMEK signature correlated with poor prognosis in several cancer conditions, including PDAC, and with reduced response to immunecheckpoint inhibition in bladder cancers

LIST OF CONTENT

__INTRODUCTION__

PANCREAS

The pancreas is a glandular organ located in the abdominal cavity. Anatomically, it is divided into 5 parts: the head, the uncinate process, the neck, the body, and the tail. The pancreas is made of two components: the exocrine and the endocrine part. The exocrine component is made of ductal cells and acinar cells. Acinar cells represent the 85% of the total pancreas and their function is to produce digestive enzymes, such as trypsin, amylase, and lipase that are secreted from the ductal tree into the duodenum. Ductal cells form the epithelium of branched tubes which have the role to deliver the enzymes produced by acinar cells to the digestive tract and to produce bicarbonate. The endocrine compartment is formed by the islet of Langerhans, which comprises around 1-2% of the pancreas. Those glands are composed by different cell types that are involved in the secretion of hormones, such as insulin (β-cells), glucagon (α-cells), pancreatic polypeptide (γ- cells) and somatostatin (δ-cells) (Atkinson et al., 2020).

PANCREATIC NEOPLASM

The two functional components of the pancreas can give rise to different neoplasms. From the exocrine compartment originates the pancreatic ductal adenocarcinoma (PDAC), which is the prevalent malignant pancreatic tumour, and a minority of other rare tumours, such as solid-pseudopapillary neoplasm, acinar cell carcinoma, and pancreatoblastoma (Hackeng et al., 2016). Pancreatic neuroendocrine tumours (pNETs) arise from the endocrine component and are considered heterogeneous in terms of clinical and pathological features. Generally, pNETs have a relatively slow clinical course (Ma et al., 2020).

PANCREATIC DUCTAL ADENOCARCINOMA

Pancreatic Ductal Adenocarcinoma (PDAC) is one of the most aggressive cancers with a 5-year survival rate of 11% (Siegel et al., 2022). This dismal prognosis is mainly due to the lack of specific symptoms that leads to a late diagnosis, with only 15-20 % of the patients presenting with a resectable disease (Gobbi et al., 2013). For the patients who are not eligible for surgery, standard chemotherapy provides a modest survival benefit (Conroy et al., 2011; Von Hoff et al., 2013). Beside familiar history, several factors can increase the risk of PDAC development, such as smoke, obesity, diabetes, and pancreatitis (Klein, 2021). Pancreatic cancer can arise from three kind of precursor lesions: Pancreatic intraepithelial neoplasia (PanIN), Intraductal papillary mucinous neoplasm (IPMN), and Mucinous cystic neoplasm (MCN) (Hezel et al., 2006). PanINs are microscopic lesions initiating in pancreatic ducts. They are classified in four stages: PanIN 1 (1A and 1B), PanIN 2, and PanIN 3. These lesions have a progression from moderate dysplasia to high-grade dysplasia till the invasive carcinoma, and during this progression also the number of genetic mutations raises (Hruban et al., 2001; Distler et al., 2014). PanIN1 are flat (PanIN 1A) or papillary (PanIN 1B) lesions. Cells are characterized by columnar shape and uniform basally oriented nuclei. Genetically, those lesions show telomere shortening and mutation in the most frequently altered gene in PDAC *K-RAS* (Distler et al., 2014; Zhang et al., 2016). PanIN 2 are mostly papillary lesions and manifest high nuclear atypia, loss of nuclear polarity, nuclear crowding, nuclear hyperchromasia and nuclear pseudostratification (Zhang et al., 2016; Hruban, Maitra & Goggins, 2008). PanIN 2 usually harbours mutations of *p16INK4a* that is inactivated in more than 50% of pancreatic cancers (Hruban, Maitra & Goggins, 2008; Waddell et al., 2015). PanIN 3 is also known as "carcinoma *in situ*". Those non-invasive lesions are characterized by high mitotic figures and severe architectural atypia. Accumulation of genetic alterations in both oncogenes and tumour suppressor genes (such as *TP53*, *SMAD4*, and *BRCA2*) can drive the progression from PanIN 3 to the invasive malignant cancer (Distler et al., 2014; Zhang et al., 2016; Hruban, Maitra & Goggins, 2008). Unfortunately, PanIN lesions are not detectable on imaging such as computerized tomography (CT), magnetic resonance imaging (MRI) or endoscopic ultrasound (EUS) (Muniraj et

al., 2013). IPMNs have a bigger size compared to PanIN but are less frequent as precursor lesion for pancreatic tumour. Those lesions have a papillary architecture and are characterize by mucin production. Imaging technologies are now available to detect IPMN Zhang et al., 2016; Hruban, Maitra & Goggins, 2008; Muniraj et al., 2013). MCN is more common in females, it's characterized by mucinous cytology and no connection with the pancreatic ducts (Distler et al., 2014).

MOLECULAR ALTERATION OF PDAC

Genetic analysis of pancreatic cancer has indicated that multiple mutations accumulate over time. PDAC shows an average of 63 genetic alterations that are involved in 12 functional pathways such as DNA repair, cell cycle regulation, axon guidance, chromatin remodelling, and proliferation. Among those, mutations of *K-RAS, TP53, SMAD4,* and *CDKN2A* are the most frequent genetic alterations in PDAC (Waddell et al., 2015; Jones et al., 2008; Gil et al., 2021).

- **K-RAS**

  K-RAS is mutated in the majority of pancreatic tumours (more than 90%) (Waddell et al., 2015). The most frequent activating K-RAS mutations are point mutations that occur at codon 12 (in 80-90% of pancreatic cancers) and less likely at codons 13 and 61 (Waters & Der, 2018). Point mutations in codon 12 are detected in ∼30% of early neoplasms, while in advanced PDAC the frequency can reach the 100% (Hezel et al., 2006). K-RAS is a member of the RAS family of GTP-binding proteins that are involved in signal transduction across the membrane in response to a signal induced by a growth factor (Maitra & Hruban, 2008). This mediates several cellular functions including proliferation, differentiation, cell shape, migration, endocytosis, cell survival and cell cycle progression or senescence (Rajalingam et al., 2007). In a normal cell, wild type K-RAS binds to GTP and activates a variety of effectors in response to mitogenic stimuli. Following exhaustion of the stimulus, GTP is hydrolysed to GDP and K-RAS is shut off. Although it was

thought that mutated K-RAS is constitutively active, recent evidence showed that K-RAS mutations significatively reduce the hydrolysis rate of GTP, hence sustaining the signalling downstream (Kemp et al., 2023; Hallin et al., 2020; Lito et al., 2016). K-RAS activates several downstream pathways, the most important ones are: Mitogen-Activated Protein Kinase (MAPK), Phosphoinositide 3-Kinase (PI3K), and Nuclear factor κB (NFκB) (Eser et al., 2014).

- **TP53**

TP53 is a tumour suppressor gene that encodes for a transcription factor involved in the control of cell cycle and apoptosis. It becomes activated in response to DNA damage and form a tetramer that binds to DNA and induces the expression of several genes. It has a short half-life and is present in a low concentration in the cell. TP53 half-life is controlled by the oncogene MDM2, which ubiquitinates TP53 and therefore determines its proteasomal degradation. MDM2 itself is under tight transcriptional control by TP53, which establish a feedback loop mechanism to regulate its own expression and activity. *TP53* is mutated in 50-75% of PDAC cases and generally is inactivated by intra-genic mutation combined with loss of the second wild-type allele. *TP53* mutations generally occur in the exon that encodes for the DNA binding domain and most of them are point mutations, while a minority consists in intragenic deletions or insertions. When TP53 is mutated, it cannot bind the DNA to promote expression of target genes. Its inactivity has an impact on DNA damage and leads to uncontrolled cell growth and increase in cell survival, beside promoting genetic instability. Inactivation of TP53 is a late event in PDAC progression, in fact it has been detected overall in advanced PanIN3 (Magee et al., 2001; Gil et al., 2021; Guo, Xie & Zheng, 2016).

- **CDKN2A/p16**

p16 is a tumour suppressor gene that encodes for a cyclin-dependent kinase (CDK) inhibitor that slows down the cell cycle by prohibiting

progression from G1 phase to S phase. It acts by impairing Retinoblastoma Protein (RB) phosphorylation by cyclin D and CDK4/6. RB blocks elongation factor 2 (E2F) activity, which is a transcriptional factor that regulates expression of genes essential for DNA replication. Hyper-phosphorylation of Rb, induced by mitogenic stimuli, prevents its interaction with E2F; in this way pRB-E2F complex dissociates and E2F mediates transcription of genes responsible for DNA synthesis. p16 keeps pRB in a hypo-phosphorylation state so it can bind and block E2F activity (Maitra & Hruban, 2008; Magee et al., 2001). p16 is inactivated in 90% of PDAC patients and this event happens in PanIN2 stage of PDAC development. Usually, the inactivation occurs by point mutations, allelic losses or by promotor silencing through hyper-methylation of CpG islands (Maitra & Hruban, 2008; Magee et al., 2001; Guo, Xie & Zheng, 2016).

- **SMAD4/DPC4**

DPC4 is a tumour suppressor gene that encodes for SMAD4, a 64 kDa protein that has inhibitory effects on cell growth and angiogenesis. SMAD4 proteins are involved in transducing signals from the TGFβ-TGFRβ axis (Maitra & Hruban, 2008; Sarkar, Banerjee & Li 2007). Normally, TGFβ has a tumour suppressor activity, leading to growth arrest. Nevertheless, in late tumour development, when cancer cells become intolerant to TGFβ-mediated growth inhibition, it exerts a pro-tumorigenic effect by promoting angiogenesis, invasion and metastatization (Connolly, Freimuth & Akhurst, 2012). *DPC4* is deleted in almost 55% of PDAC cases, and the inactivation mainly occurs by homozygous deletion or by intragenic mutations and loss of heterozygosity. The loss is a late event in tumorigenesis, in fact it occurs normally during late PanIN3 lesions. Generally, loss of SMAD4 expression is higher in poorly differentiated PDAC accompanied by poor prognosis and widespread metastasis (Maitra & Hruban, 2008; Sarkar, Banerjee & Li 2007).

MOLECULAR SUBTYPES OF PDAC

Beside histological classification, PDAC has been classified based on transcriptomic profiles. In the last years, several classifications have emerged. The first classification was proposed in 2011 by Collisson, who described three PDAC subtypes: classical, quasi-mesenchymal, and exocrine-like (Collisson et al., 2011). In 2015, Moffitt classified PDAC as classical or basal-like based on virtual microdissected data of pancreatic gene expression microarrays (Moffitt et al., 2015). Bailey and colleagues in 2016 described four PDAC subtypes: pancreatic progenitor, squamous, immunogenic, and aberrantly differentiated endocrine exocrine (ADEX) (Bailey et al., 2016). An integrated multi-platform analysis performed by The Cancer Genome Atlas Research Network (TCGA) in 2017 provides a better insight into molecular classification of PDAC (The Cancer Genome Atlas Research Network, 2017). They applied clustering techniques to reproduce the classification of Collisson (Collisson et al., 2011), Moffitt (Moffitt et al., 2015), and Bailey (Bailey et al., 2016) on a cohort of 150 PDAC specimens (The Genome Atlas Research Network, 2017). They reported a strong overlap between the classical subtypes proposed by Collisson and Moffitt (Collisson et al., 2011; Moffitt et al., 2015) with the pancreatic progenitor subtype proposed by Bailey (Bailey et al., 2016). In addition, the basal-like subtype defined by Moffitt (Moffitt et al., 2015) significantly overlaps with the squamous subtype from Bailey (Bailey et al., 2016) and partially with the quasi-mesenchymal subtype from Collisson (Collisson et al., 2011) (The Cancer Genome Atlas Research Network, 2017). TCGA also reported that tumour purity can affect the molecular classification of PDAC. In particular, samples classified as immunogenic from Bailey (Bailey et al., 2016) and a portion of samples classified as quasi-mesenchymal from Collisson (Collisson et al., 2011) showed low neoplastic purity and high leukocyte infiltration (Genome Atlas Research Network, 2017). Furthermore, the ADEX subtype from Bailey (Bailey et al., 2016) and the exocrine-like from Collisson (Collisson et al., 2011) significant overlap and show low tumour purity, suggesting a possible contamination from non-neoplastic cells (The Genome Atlas Research Network, 2017) (**Figure 1.1**). Other studies support the evidence that ADEX and exocrine-like subtypes from Bailey and Collisson respectively

(Collisson et al., 2011; Bailey et al., 2016) are potentially a consequence of contamination with acinar cells from normal pancreas (Moffitt et al., 2015; Puleo et al., 2018; Lautizi et al., 2022). Therefore, samples with high tumour purity (i.e. non contaminated from non-neoplastic cells) can be consistently classified in two consensus clusters: basal-like/squamous and classical/progenitor (The Cancer Genome Atlas Research Network, 2017).
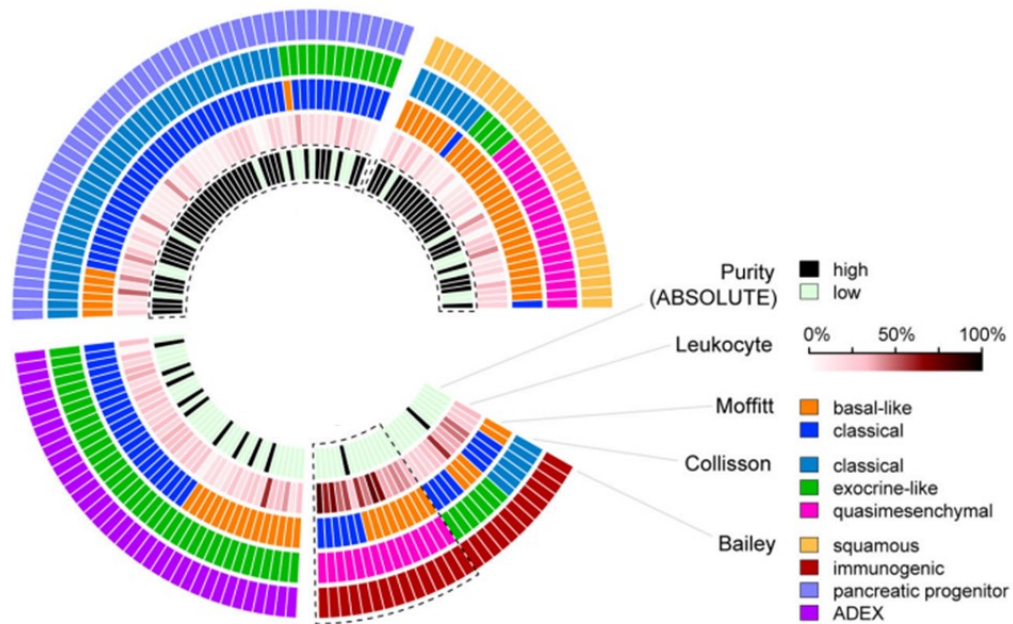

Figure 1.1 Impact of purity on molecular analysis (From The Cancer Genome Atlas Research Network, 2017)

More recently, Chan-Seng-Yue proposed a classification derived from RNA-seq data of microdissected epithelium from primary resected and advanced PDAC patients that highlights the intra-tumoural heterogeneity of PDAC. They proposed five classes: classical A, classical B, hybrid, basal-like A, and basal-like B (Chan-Seng-Yue et al., 2020). The classical A-B and the basal-like A-B subtypes overlap with the previously defined classical/progenitor and basal-like/squamous clusters respectively (Chan-Seng-Yue et al., 2020; The Cancer Genome Atlas Research Network, 2017) (**Figure 1.2**). The hybrid subtype is described as an intermediate phenotype between the classical/progenitor and basal-like/squamous (Chan-Seng-Yue et al., 2020; The Cancer Genome Atlas Research Network, 2017) and it

represent samples with uncertain and discordant classification by Collisson, Moffitt and Bailey (Chan-Seng-Yue et al., 2020; Collisson et al., 2011; Moffitt et al., 2015; Bailey et al., 2016). The existence of a gene expression continuum driven by a mixture of intra-tumoral subpopulations was further confirmed by single-cell analysis (Chan-Seng-Yue et al., 2020). The existence of a hybrid subtype with a concomitant expression of classical/progenitor and basal-like/squamous genes has also been reported by Thopam in 2021 (Thopam et al., 2021). They collected sequencing data from 574 PDAC and, consistently with Chan-Seng-Yue data (Chan-Seng-Yue et al., 2020), they observed the hybrid phenotype in those samples with subtype-discordant calls across different classificators (Thopam et al., 2021; Collisson et al., 2011; Moffitt et al., 2015; Bailey et al., 2016). In 2021, Raghavan et al. provided a molecular classification at single cell resolution, maximizing the contribution of neoplastic cells to the classification (Raghavan et al., 2021). They derived three signatures: single cell classical (scClassical) which represent the classical/progenitor subtype, single cell basal (scBasal) representative of the basal-like/squamous subtype, and intermediate coexpressor (IC) (Raghavan et al., 2021). The IC identify cells with expression of both scBasal and scClassical genes, with intermediate features of both programs, and poorly described by previously reported classifications (Raghavan et al., 2021; Chan-Seng-Yue et al., 2020; Collisson et al., 2011; Moffitt et al., 2015; Bailey et al., 2016). This study highlights even more the inter- and intra-tumoural heterogeneity of PDAC and support the idea that the molecular subtype is a plastic cell state rather than a mutually exclusive classification (Raghavan et al., 2021). An alternative to the binary classification classical/progenitor - basal-like/squamous was proposed by Nicolle et colleagues (Nicolle et al., 2020). Using Patient-derived xenografts (PDX) they derived a PDAC molecular gradient (PAMG) which unify all PDAC pre-existing classifications. The molecular subtype is defined as a continuum, which includes tumours with mixed features, with classical/progenitor and basal-like/squamous identities at the opposite ends of the spectra (Nicolle et al., 2020).
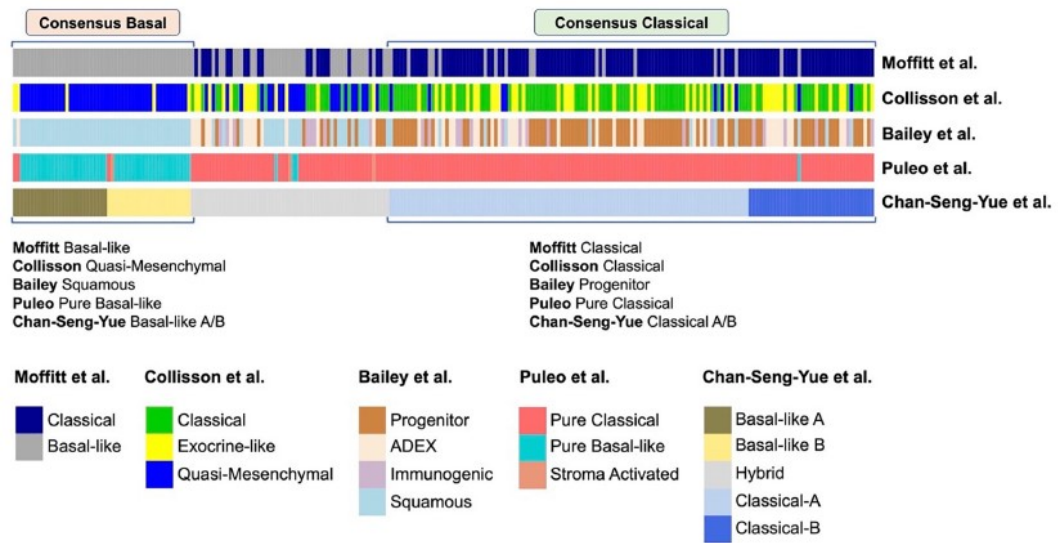
Figure 1.2 Comparison of different transcriptional classifications of PDAC (From Zhou et al., 2021)

Intrinsic determinants of PDAC subtypes

The molecular phenotype is a cell state driven by both intrinsic and extrinsic factors. Transcription factors and epigenetic determine the intrinsic cell identity. The classical/progenitor subtype is enriched for gene programs driven by endodermal transcription factors (e.g., GATA6, GATA4, HNF1A, HNF4A, and PDX1) (de Andrés et al., 2023; Kloesch et al., 2022; Bailey et al., 2016). It shows a more favourable prognosis and is enriched for inactivation of SMAD4 (Chan-Seng-Yue et al., 2020; Collisson et al., 2011; Moffitt et al., 2015; Bailey et al., 2016). Conversely, the more aggressive basal-like/squamous subtype is characterized by the loss of endodermal identity and the acquisition of squamous programs, such as those driven by ΔNP63 (Somerville et al., 2018; Bailey et al., 2016). Other transcription factors that drive this subtype are c-MYC (Bailey et al., 2016) and GLI2 (Adams et al., 2019). In addition, the basal-like/squamous subtype is driven by the super enhancer MET (Lomberk et al., 2018) and is enriched for mutations in chromatin modifying enzymes such as KDM6A, MLL2, and MLL3 (Bailey et al., 2016). The basal-like/squamous subtype correlates with a worse prognosis, chemoresistance, and immune exclusion (Moffitt et al., 2015; Bailey et al., 2016; Chan-Seng-Yue et al., 2020).

Extrinsic determinants of PDAC subtypes

Exogen stimuli can be involved in shape PDAC molecular phenotypes as well. In the last years, several studies highlight the influence of the tumour microenvironment (TME) on the molecular subtype of neoplastic cells. Miyabayashi and colleagues set up an *in vivo* xenograft model that could recapitulate the basal-like/squamous and classical/progenitor subtypes of PDAC. They injected Patient-derived organoids either directly in the pancreatic interstitium ("orthotopically grafted organoid" (OGO)) or into the main pancreatic ducts ("intraductally grafted organoid" (IGO)) of immunodeficient mice (Miyabayashi et al., 2020). They observed differences in the molecular subtypes between OGO and IGO, with OGO being more basal-like/squamous. Only OGO are exposed to the cues from TME which drive the aggressive basal-like/squamous subtype of PDAC. This effect is explained by the autocrine and paracrine effect of transforming growth factor β1 (TGF-β1) on stromal and cancer cells (Miyabayashi et al., 2020). Raghavan and colleagues, using Patient-derived organoids and matched biopsies, showed that the culture medium can affect the transcriptional state of cancer cells, introducing a culture-specific bias driven by altered TME signals (Raghavan et al., 2021). The *in vitro* models retain genetic fidelity, but the lack of cancer niche induces skewed phenotypes with altered pharmacologic sensitivity. In particular, in agreement with Miyabayashi et al. (Miyabayashi et al., 2020), they identified a key role of TGF-β1 in inducing the basal-like/squamous subtype (Raghavan et al., 2021). Shinkawa and colleagues took advantage of the organoid technology as well to study the niche dependency of cancer cells (Shinkawa et al., 2022). They identified cancer associated fibroblasts (CAFs) as the source of R-spondin 3 which is needed for the maintenance of a well differentiated phenotype (defined as classical/progenitor) of PDAC. Well differentiated tumours (i.e. classical/progenitor) are strongly niche-dependent and the removal of CAFs can drive the progression to a poor differentiated (defined as basal-like/squamous) disease. Of note, poor differentiated tumours (i.e. basal-like/squamous) are niche independent and CAFs are not able to drive a conversion to a well differentiated (i.e. classical/progenitor) phenotype (Shinkawa et al., 2022). Beside CAFs, other stromal populations can affect the molecular subtype of cancer cells. CSFR1+

macrophages and CXCR2 neutrophils have been shown to promote the basal-like/squamous subtype of PDAC (Candido et al., 2018; Steele et al., 2016). Similarly, Tu and colleagues defined TNF-α+ macrophages as source of TNFα which force classical/progenitor PDAC cells to an aggressive basal-like/squamous phenotype (Tu et al., 2021). TNF-α+ macrophages are recruited by cancer cells through secretion of CCL2. They integrated extrinsic and intrinsic PDAC subtypes determinants demonstrating that the basal-like/squamous neoplastic state is sustained via BRD4-mediated cJUN/AP1 expression, which induces CCL2 expression and, as consequence, the recruitment of TNF-α+ macrophages (Tu et al., 2021).

<u>Stromal molecular classification of PDAC</u>

Given the low neoplastic content of PDAC and the functional role of TME, some molecular classifications take into account also the stromal features for subtype definition. Moffitt et al., proposed two stromal subtypes named "normal" and "activated", with the latter associated with activate inflammatory stromal response and tumour promotion (Moffitt et al., 2015). In 2018, Puleo and colleagues classified PDAC in five subtypes. Of those, three subgroups are representative of the previously describes classical/progenitor (pure classical/immune classical) and basal-like/squamous (pure basal-like) lineages (**Figure 1.2**). On the other hand, two new subtypes named "stroma activated" and "desmoplastic" reflect different features of the microenvironment. In particular, the stroma activated subtypes is enriched in activated stroma components with high levels of α-SMA, SPARC, and FAP, while the desmoplastic subtype is associated with immune and inflammatory content with high expression of vascular and structural components (Puleo et al., 2018). Lastly, in 2019 another classification was proposed by Maurer et al. in which they highlighted the existence of two stromal subtypes: ECM-rich and immune-rich (Maurer et al., 2019). The ECM-rich subtype is the most aggressive one and is enriched for genes involved in extra cellular matrix pathways. The immune-rich subtype is enriched in immune related pathways and correlate with a better prognosis (Maurer et al., 2019). Those stromal signatures are often combined with the conventional PDAC classification to add prognostic information from the microenvironment.

THE TUMOUR MICROENVIRONMENT

The tumour microenvironment (TME) is composed by non-neoplastic cells (such as fibroblasts, endothelial cells, and immune cells) embedded in an extracellular matrix (ECM). The ECM is composed by structural proteins (e.g. collagen, fibronectin, proteoglycans, and hyaluronic acid) that retains several enzymes, and molecules, like cytokines and growth factors. In pancreatic cancer, stroma can comprise up to 80-90% of the tumour bulk, and fibroblasts are the most abundant stromal population, often outnumbering neoplastic cells (Kalluri & Zeisberg, 2006; Feig et al 2012).

CAFs: definition and origin

Fibroblasts are elongated cells with a spindle-like shape usually identified by the expression of specific markers such as, fibroblast-specific protein 1 (FSP-1), platelet-derived growth factor receptor β (PDGFRβ), and fibroblast activation protein (FAP). Fibroblasts that are found in the tumoral bulk are named cancer associated fibroblasts (CAFs) (Öhlund, Elyada & Tuveson, 2014). CAFs can originate from different cell types upon recruitment and reprogramming by cancer stimuli, such as secreted factors, reactive oxygen species (ROS), or hypoxia. Although historically it was thought that pancreatic stellate cells (PSCs) are the main source of CAFs, recent evidence show that PSCs (Fabp4+) give rise only to a small subset of them (Helms et al., 2022) (**Figure 1.3**). In healthy pancreas, PSCs are quiescent, store Vitamin A in lipid droplets, and are involved in maintaining tissue homeostasis. Upon exposure to tissue damage or cancer-derived stimuli, they acquire myofibroblastic features and become active (Riopel et al., 2013). The majority of CAFs arise from resident fibroblasts (Han et al., 2023; Garcia et al., 2020). They are found in normal pancreas, however, unlike PSCs, they do not store lipid droplets (Garcia et al., 2020). It has been reported that resident fibroblasts in normal pancreas originate from splanchnic mesenchyme (i.e the layer of mesoderm adjacent to the foregut endoderm during fetal development), they expand during cancer development and give rise to around half of CAFs (Han et al., 2023). Two lineages of resident fibroblasts have been identified: Gli+ and Hoxp6+. Gli+ fibroblasts are the origin of the majority of CAFs, they expand during tumorigenesis

and acquire expression of α-SMA. Hoxp6+ CAFs are found in the tumour bulk, although in a very low number as Hoxp6+ fibroblasts do not expand during cancer development (Garcia et al., 2020) (**Figure 1.3**). Other minor sources of CAFs are bone marrow and mesothelial cells (WT1+) (Han et al., 2023; Huang et al., 2022) (**Figure 1.3**).

CAFs: functions

Upon reprogramming and activation, CAFs undergo morphological changes, and start to secrete ECM molecules and growth factors. This intense reaction leads to a dense matrix deposition called desmoplasia (Öhlund, Elyada & Tuveson, 2014). Beside creating an inflammatory environment, the desmoplastic reaction increases the interstitial fluid pressure, leading to vessel compression, reduced tissue perfusion, and hypoxia. It has been hypothesized that the desmoplastic reaction could reduce chemotherapy delivery in the tumour site by creating a physical barrier, therefore exerting a protective function for cancer cells. In the last decade, several approaches aimed to reduce this fibrotic reaction by targeting ECM components or directly CAFs in order to obtain an improved disease outcome. In 2012, Provenzano and colleagues targeted hyaluronic acid (HA), one of the main ECM components, and combined its depletion with gemcitabine administration (Provenzano et al., 2012). Using autochthonous PDAC models, they demonstrated that enzymatic targeting of stromal HA restores tumour interstitial fluid pressure and functional perfusion. Moreover, the combination of HA depletion with chemotherapy resulted in increased overall survival of mice (Provenzano et al., 2012). In line with those findings, Jacobetz et al. showed that HA enzymatic depletion leads to the re-expansion of PDAC blood vessels and increased the delivery of two chemotherapeutic agents in a genetically engineered mouse model of PDAC (Jacobetz et al., 2013). Other approaches aimed to deplete CAFs by targeting CAFs-specific pathways like the Sonic Hedgehog pathway (SHH). In literature, different outcomes have been reported from this targeting strategy. In 2009, Olive and colleagues demonstrated that pharmacologic ablation of CAFs increase tumour perfusion and reduce stromal content (Olive et al., 2009). This effect is driven by the inhibition of Smoothened (Smo), a protein that mediates the downstream signalling of SHH. The treatment with Smo inhibitor alone did not

improve survival, while its combination with the chemotherapeutic agent gemcitabine lead to a better outcome for treated mice (Olive et al., 2009). This promising strategy has been translated into clinical trial, although it resulted in a failed Phase II as no improvement in response rate or overall survival was detected in patients with metastatic PDAC (Catenacci et al., 2015). In 2014, Rhim and colleagues sought to interrogate the role of the tumour stroma by using both genetic deletion and pharmacologic inhibition of SHH pathway (Rhim et al., 2014). They found that genetic depletion of SHH accelerates PDAC progression leading to the development of undifferentiated tumours with low stromal content. This effect might be a consequence of increased perfusion, as it provides increased delivery of nutrients at tumour site (Rhim et al., 2014). The pharmacologic approach used by Rhim et al. is similar to the one proposed by Olive et al., with the only difference in duration (Olive et al., 2009; Rhim et al., 2014). Unlike short-term, the long-term Smoothened inhibition tested by Rhim and colleagues, yields poorly differentiated tumours with increased proliferation and vascularity (Rhim et al., 2014). Those data show that, despite short-term Smo inhibition provides a beneficial effect due to increased drug delivery, in long-term treatment this advantage is overcome by the harmful effects of stroma ablation. This provides evidence that stroma act to restrain rather than promote tumour (Rhim et al., 2014). Similar results have been reported by Lee and colleagues in the same year (Lee et al., 2014). Genetic depletion of SHH accelerates PDAC progression and decreased the overall survival in genetically engineered mouse (GEM) model of pancreatic cancer (Lee et al., 2014). Pharmacologic inhibition of SHH, through SHH antagonist, affected the balance between epithelial and stromal elements leading to depletion of desmoplasia, prevalence of the epithelium compartment and a worse disease outcome (Lee et al., 2014). Conversely, the pharmacological activation of the pathway yields stromal hyperplasia and reduced epithelial growth. This study reinforces the observation of Rhim and colleagues providing additional evidence that CAFs might have a protective role in PDAC (Rhim et al., 2014; Lee et al., 2014). A different approach to deplete CAFs was proposed by Ozdemir et al. in 2014 by using transgenic mice with ability to delete α-SMA+ fibroblasts in pancreatic cancer (Ozdemir et al., 2014). The depletion of α-SMA positive cells enhanced the tumour invasion and

reduced the survival in animals of the experimental cohort (Ozdemir et al., 2014). Of note, this targeting approach did not increase tumour perfusion and the additional administration of gemcitabine did not improve the survival of mice (Ozdemir et al., 2014). Those different stromal targeting strategies have highlighted the presence of both tumour-promoting and tumour-restraining components in the PDAC stroma, however, in recent years, the concept of CAFs heterogeneity have been introduced which shed light on the functional role of CAFs in PDAC.

CAFs: heterogeneity

Two main subtypes of CAFs have been defined: inflammatory CAFs (iCAFs) and myofibroblasts (myCAFs) (Ohlund et al., 2017). iCAFs arise from resident fibroblasts (Han et al., 2023; Garcia et al., 2020; Dominguez et al., 2020) and are found distant from cancer cells (Ohlund et al., 2017) (**Figure 1.3**). They present low α-SMA level and are characterized by the secretion of inflammatory molecules, such as IL6, CXCL1, and LIF (Ohlund et al., 2017). The iCAF phenotype is induced by cancer through the secretion of IL1 which activate the JAK-STAT signalling pathway (Biffi et al., 2019). They are defined as tumour promoting population and are potentially involved in chemoresistance and immune suppression (Biffi et al., 2019). Additional evidence of their pro-tumorigenic role derived from the existence of subtypes of inflammatory CAFs with specific functions. Djurec and colleagues identified PDGFRα+ CAFs as a subcluster of CAFs with inflammatory phenotype that exert a pro-tumorigenic function through secretion of the apolipoprotein Saa3 (Djurec et al., 2018). Zhang et al. identified a subset of iCAFs that mediate platinum resistance in PDAC patients through the secretion of IL8 (Zhang et al., 2022). In addition, it has been reported that iCAFs sustain tumour progression through the secretion of hepatocyte growth factor (HGF) (Bhattacharjee et al., 2021). On the other hand, myCAFs can originate both from resident fibroblasts and PSCs (Han et al., 2023; Garcia et al., 2020; Dominguez et al., 2020; Helms et al.,2022). They surround the neoplastic cells, present high expression of α-SMA and are mainly involved in ECM deposition and remodelling (Ohlund et al., 2017) (**Figure 1.3**). The myCAF phenotype is TGF-β1 driven: cancer cells secrete TGF-β1 which antagonize the iCAF phenotype by downregulating the receptor of IL1. The short-range activity of TGFβ explains the localization of myCAFs in proximity of

neoplastic cells (Biffi et al., 2019). myCAFs are defined as a tumour-restraining population (Rhim et al., 2014; Ozdemir et al., 2014; Biffi et al., 2019) Accordingly, it has been recently reported that myCAFs exert an antitumoral effect by secreting Collagen I which limits cancer spreading (Bhattacharjee et al., 2021). Conversely, they promote tumour progression through the secretion of hyaluronan (Bhattacharjee et al., 2021). Additional evidence of tumour promoting functions of myCAFs have provided by the identification of LRRC15+ myofibroblasts (Dominguez et al. 2020). LRRC15+ myofibroblasts are defined as an aggressive TGF-β1-driven myCAFs subpopulation and are involved in poor response to immunotherapy in several cancer types (Dominguez et al., 2020). LRRC15+ phenotype is TGFBR2 dependent, and LRRC15+ CAFs exert their immune modulatory function by directly suppressing CD8+ T cells (Krishnamurty et al., 2022). Those data highlight that myCAFs have a greater functional heterogeneity compared to iCAFs. Of note, myCAFs and iCAFs are not two different lineages, they are shaped by different stimuli from the cancer niche and their phenotypes are plastic (Ohlund et al., 2017; Biffi et al., 2019). Those new insight into CAFs heterogeneity allow a better explanation to the contradictory results obtained with SHH inhibition (Olive et al., 2009; Lee et al., 2014; Rhim et al., 2014). In 2021, Steele and colleagues demonstrated that the SHH pathway is more active in myCAFs than iCAFs (Steele et al., 2021). Pharmacological SHH inhibition with Smoothened antagonist reduced the amount of myCAF while the number of iCAFs increased. iCAFs accumulation correlates with the reduction of cytotoxic T cells with concomitant expansion of regulatory T cells (Treg) (Steele et al., 2021). Therefore, the detrimental effect observed with SHH inhibition might be a consequence of the specific depletion of myCAFs, with the persistence of tumour promoting iCAFs (Olive et al., 2009; Lee et al., 2014; Rhim et al., 2014; Steele et al., 2021). In the last years, two additional subtypes that co-exist with myCAFs and iCAFs have been described: antigen presenting CAFs (apCAFs) (Elyada et al., 2019) and metabolic CAFs (meCAFs) (Wang et al., 2021). apCAFs originate from mesothelial cells (Huang et al., 2022; Dominguez et al., 2020) (**Figure 1.3**). During tumour progression, they downregulate mesothelial markers and acquire fibroblastic features under paracrine stimulation from cancer cells (Huang et al.,

2022). In addition, they express class II MHC and CD74 without co-stimulatory molecules (Elyada et al., 2019). apCAFs are involved in immune modulation by direct ligation and induction of naive CD4+ T cells into Tregs (Huang et al., 2022). meCAFs are a subset of CAFs characterized by high metabolic activity, in particular glycolysis. They are found in immune hot, low desmoplastic regions and correlates with poor prognosis but better immunotherapy response (Wang et al., 2021).

CAFs: other classifications

Beside iCAFs-myCAFs dichotomy, other classifications with functional significance have been proposed for CAFs. Fibroblasts can be classified in two subtypes accordingly to their expression of α-SMA and FAP (**Figure 1.3**). FAP high (FAP[hi]) CAFs have been reported to be involved in ECM remodelling and exert tumour promoting functions (Avery et al., 2017; McAndrews et al, 2022). α-SMA high (α-SMA[hi]) CAFs mediate contraction and are defined as a tumour-restraining population (Avery et al. 2017; McAndrews et al, 2022; Chen et al., 2021). In particular, it has been reported that α-SMA[hi] CAFs ablation decrease survival *in vivo* (McAndrews et al, 2022) and that depletion of type I collagen (Col1) in α-SMA[hi] fibroblasts accelerates progression of pancreatic cancer through the recruitment of myeloid-derived suppressor cells (Chen et al., 2021). In addition, IL6 produced specifically by α-SMA[hi] fibroblasts mediates chemoresistance in murine models of PDAC (McAndrews et al, 2022).

In 2019, Mizutani and colleagues defined cancer-restraining CAFs (rCAFs) and cancer-promoting CAFs (pCAFs) based on their expression of Meflin (Mizutani et al., 2019). They reported that infiltration of Meflin+ CAFs (rCAFs) correlated with favourable patient outcome, while the presence of pCAFs or genetic ablation of rCAFs led to significant tumour progression with poorly differentiated histology in a PDAC mouse model (Mizutani et al., 2019). Functionally, Meflin suppress the activity of the lysyl oxidase (LOX) thus impairing collagen cross-linking (Mizutani et al., 2019; Iida et al., 2021). Together with MRXA8 (a specific marker for rCAFs), Meflin is downregulated upon exposure to specific stimuli, such as hypoxia and TGF-β1 (Mizutani et al., 2019; Ichihara et al., 2022). In agreement with its tumour

restraining function, it has been reported that induction of Meflin expression in pCAFs increase chemosensitivity of mouse PDAC (Iida et al., 2021).

Another classification distinguishes two non-convertible CAFs lineages based on CD105 expression: CD105 negative fibroblasts suppress tumour growth by supporting anti-tumour immunity, while CD105 positive are tumour permissive (Hutton et al., 2021) (**Figure 1.3**).

Beside the increasing interest in unveiling CAFs heterogeneity, it has been reported differences in the quality of stroma within tumour bulk. The intra-tumour heterogeneity highlighted the co-existence within the same tumour of reactive and deserted areas (Grünwald et al, 2021). In the reactive sub-TME, CAFs are activated, and the microenvironment is inflammatory and pro-tumorigenic. While the deserted regions are chemoprotective, ECM-rich, with low cellular content, and fibroblasts are thin and dedifferentiated (Grünwald et al, 2021). It has been reported that the co-existence of different sub-TMEs is more prognostically relevant that the type of sub-TME (Grünwald et al, 2021).
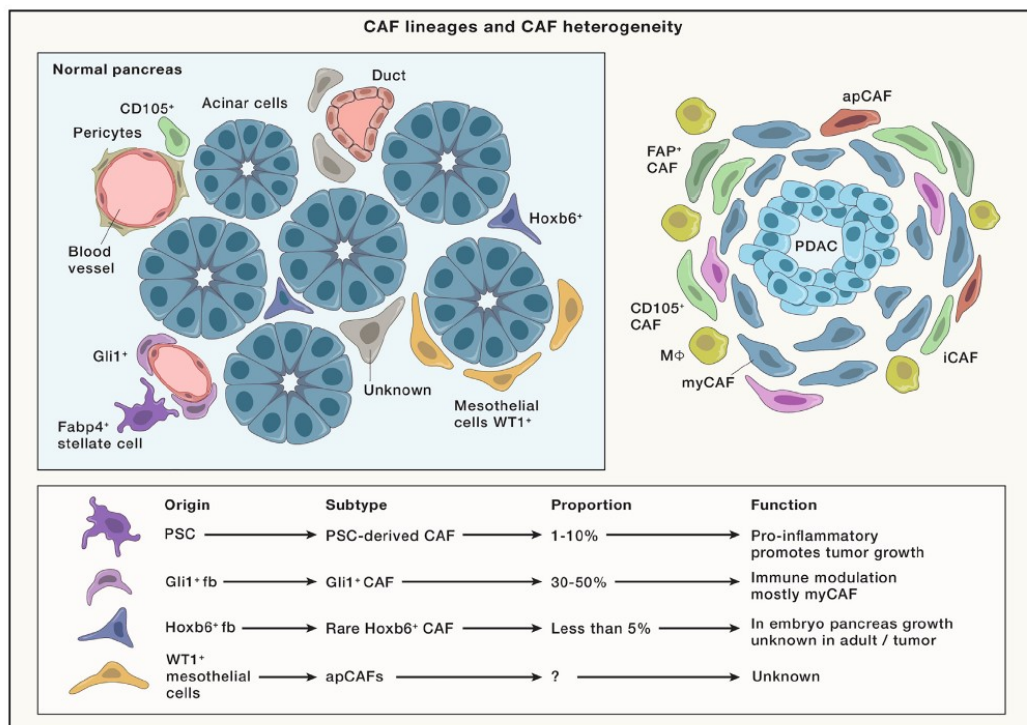

Figure 1.3 Cancer-associated fibroblast origin and heterogeneity (From Halbrook et al., 2023)
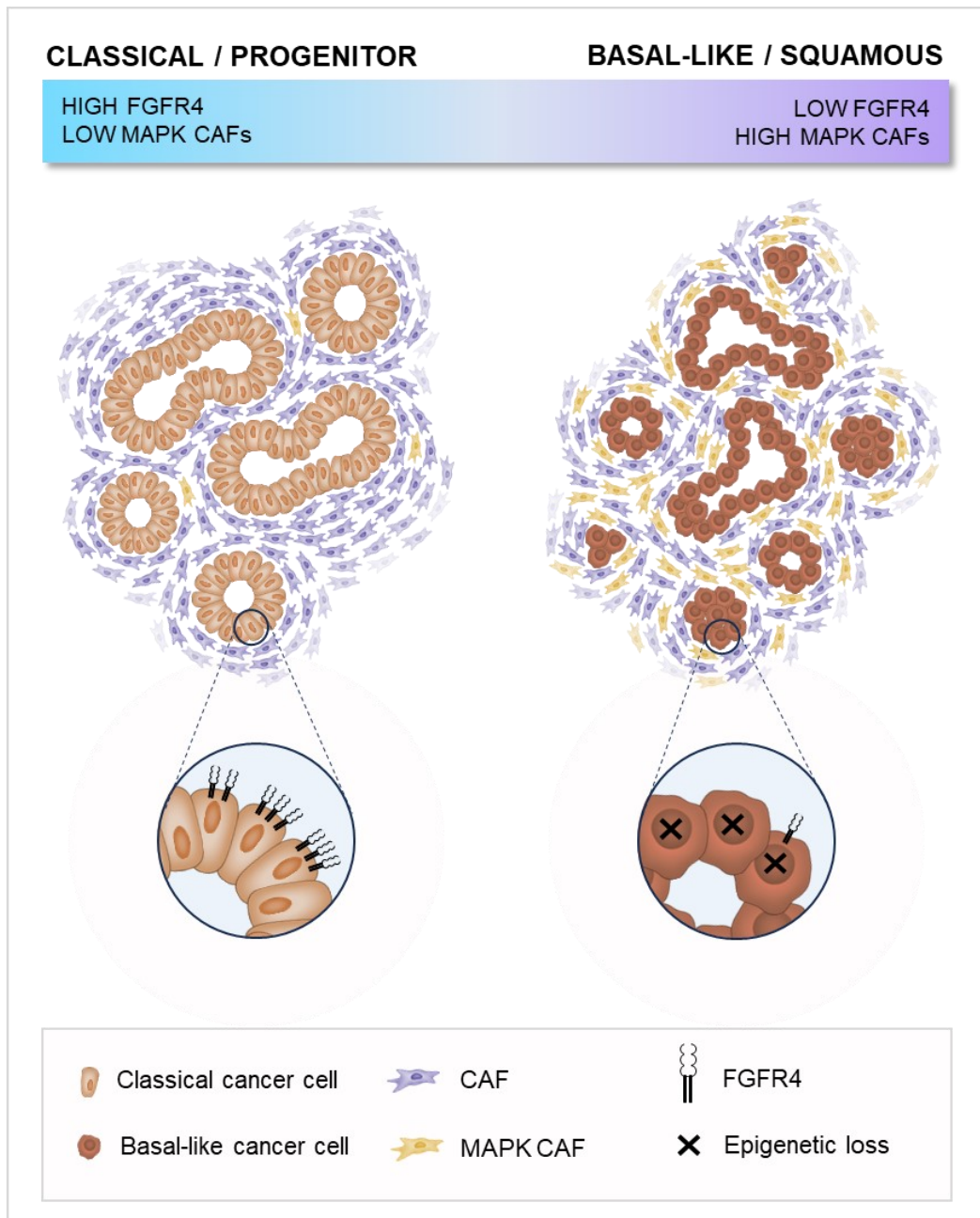
AIM

Two consensus molecular subtypes of PDAC have been identified: the classical/progenitor and the basal-like/squamous, the latter being associated with a worse prognosis. It is also clear that the integration between intrinsic and extrinsic inputs shapes the transcription cell states of cancer cells. Therefore, several attempts have been made to identify molecular determinants of cell lineage which could be used as potential targets to modulate the aggressiveness of neoplastic cells.

Historically, the study of intrinsic determinants of subtypes has focused on dissecting the role of transcriptional factors (TFs) which regulate epithelial cell identity. Receptor-Tyrosine Kinases (RTKs) are a large family of metazoan-specific plasma-membrane receptors that control several cellular processes including cell fate determination. While TFs are notoriously difficult targets for small molecules, a growing number of therapeutic compounds is approved to target RTK. Therefore, we sought here to investigate the potential role of RTKs in defining or sustaining aggressive molecular phenotypes of neoplastic cells.

However, we did not set to limit our investigation to the malignant compartment considering the importance of the tumour microenvironment in this dismal disease.

A dense desmoplastic reaction with abundant cancer-associated fibroblasts (CAFs) is a hallmark of PDAC tissues and CAFs have been proven to regulate the PDAC micro- and macrosystem. Heterogenous phenotypes of CAFs have been described and for a subset of them mechanisms of cancer-induced rewiring provided. Whether the reported fibroblasts phenotypes are differently affected by different neoplastic cell states is largely unknown. Therefore, we sought to investigate whether specific differences in CAFs can be found across cancer subtypes and if those differences have a functional impact on the epithelial phenotype.

SUMMARY

CLASSICAL / PROGENITOR

BASAL-LIKE / SQUAMOUS

HIGH FGFR4
LOW MAPK CAFs

LOW FGFR4
HIGH MAPK CAFs

Classical cancer cell   CAF   FGFR4

Basal-like cancer cell   MAPK CAF   Epigenetic loss

CHAPTER 1

Loss of FGFR4 promotes the malignant phenotype of PDAC

Sabrina D'Agosto*, Francesco Pezzini*, **Lisa Veghini***, Pietro Delfino, Claudia Fiorini, Gael D. Temgue Tane, Anais Del Curatolo, Caterina Vicentini, Giorgia Ferrari, Davide Pasini, Silvia Andreani, Francesca Lupo, Elena Fiorini, Giulia Lorenzon, Rita T. Lawlor, Borislav Rusev, Antonia Malinova, Claudio Luchini, Michele Milella, Elisabetta Sereni, Antonio Pea, Claudio Bassi, Peter Bailey, Aldo Scarpa, …Vincenzo Corbo

* co-first authors

ABSTRACT

Transcriptomic analyses of pancreatic ductal adenocarcinoma (PDAC) have identified two major epithelial subtypes with distinct biology and clinical behaviours. Here, we aimed to clarify the role of FGFR1 and FGFR4 in the definition of aggressive PDAC phenotypes. We found that the expression of *FGFR4* is exclusively detected in epithelial cells, significantly elevated in the classical PDAC subtype, and associates with better outcomes. In highly aggressive basal-like/squamous PDAC, reduced *FGFR4* expression aligns with hypermethylation of the gene and lower levels of histone marks associated with active transcription in its regulatory regions. Conversely, *FGFR1* has more promiscuous expression in both normal and malignant pancreatic tissues and is strongly associated with the EMT phenotype but not with the basal-like cell lineage. Regardless of the genetic background, the increased proliferation of FGFR4-depleted PDAC cells correlates with hyperactivation of the mTORC1 pathway both in vitro and in vivo. Downregulation of *FGFR4* in classical cell lines invariably leads to the enrichment of basal-like/squamous gene programs and is associated with either partial or full switch of phenotype. In sum, we show that endogenous levels of *FGFR4* limit the malignant phenotype of PDAC cells. Finally, we propose FGFR4 as a valuable marker for the stratification of PDAC patients.

INTRODUCTION

Pancreatic ductal adenocarcinoma (PDAC) is a malignancy arising from the exocrine pancreatic epithelium and is the deadliest cancer worldwide (Michl et al., 2021; Rahib et al., 2021). The abysmal prognosis of PDAC is contributed by late diagnosis, its complex biology, and lack of effective treatments. The molecular taxonomy of PDAC has been redefined by multiple studies that have used transcriptomic profiling to analyse bulk tissues, cell lines, and microdissected epithelia (Bailey et al., 2016; The Cancer Genome Atlas Research Network, 2017; Chan-Seng-Yue et al., 2020; Collisson et al., 2019; Moffitt et al., 2015). All classifications have highlighted the existence of two major subtypes based on characteristics of the neoplastic epithelium, namely the classical/progenitor and the basal-like/squamous subtypes. The classical/progenitor PDAC subtype is often regarded as the default pancreatic cancer subtype (Chan-Seng-Yue et al., 2020; Hayashi et al., 2020) as it is characterised by the expression of transcription factors involved in specification and maintenance of pancreatic cell fate (Bailey et al., 2016; Kloesch et al., 2021; Martinelli et al., 2017). Conversely, the basal-like/squamous subtype is associated with loss of pancreatic endodermal identity, and expression of the master regulator of basal-like cells program ΔNp63 (Bailey et al., 2016; Moffitt et al., 2015; Somerville et al., 2020). This subtype shows a significantly worse survival outcome and is enriched for inactivation of *TP53* and chromatin regulators, including *ARID1A* and *KDM6A* (Bailey et al., 2026; Andricovich et al., 2018). Preclinical data have showed that the two subtypes differ also in the response to chemotherapy (Collisson et al., 2019; Martinelli et al., 2017; Porter et al., 2019), to agents targeting the cell cycle (Dreyer et al., 2021), and further display unique metabolic vulnerabilities (Brunton et al., 2020). While there is some clinical evidence for the predictive value of transcriptomic classifications (Martinelli et al., 2017; Aung et al., 2018; Nicolle et al., 2020), clinical investigations are ongoing to conclusively demonstrate the relevance of subtype-specific treatments. Previous works have elegantly demonstrated the causative involvement of pancreatic and endodermal transcription factors (e.g. GATA6, HNF1A, HNF4A) into the maintenance of subtype-specific gene programs (Martinelli et al., 2017; Brunton et al., 2020; Kloesch et al., 2021; Kalisz et al.,

2020). In particular, the emergence of the basal-like/squamous program is almost invariably associated with the loss of expression of transcription factors regulating pancreatic cell fates. Cell fate maintenance is also ensured by the signalling of growth factors through receptor tyrosine kinases (RTKs) (Lemmon et al., 2010; Neben et al., 2019). Following activation, RTKs transmit intracellular signals of varying qualities and quantities that alter the transcriptional landscape of a cell (Lemmon et al., 2010). The fibroblast growth factors (FGFs) to Fibroblast growth factor receptors (FGFRs) axis is reportedly involved in the maturation of pancreatic cells from the endoderm (Bhushan et al., 2001; Elghazi et al., 2002; Goncalves et al., 2021; Hebrok et al., 1998). Here, we explored the involvement of FGFRs in the definition of molecular subtypes of PDAC. We report the downregulation of FGFR4 in PDAC showing basal-like/squamous features. Integrating the analysis of transcriptomic, methylation, and chromatin accessibility datasets from patient-derived tissue specimens and cultures, we shed light on the mechanisms leading to downregulation of *FGFR4* in basal-like/squamous tumours. Conversely, we found that elevated expression of *FGFR1* is a functional marker of Epithelial to Mesenchymal Transition (EMT) rather than of the basal-like/squamous subtype. To elucidate whether *FGFR4* is cause or consequence of more aggressive PDAC subtypes, we targeted the receptor using RNA interference approaches in both monolayer cell cultures and patient-derived organoids to show that its loss accelerates cell proliferation and in vivo growth regardless of the genetic and transcriptomic background of the models. Mechanistically, loss of *FGFR4* was associated with increased fluxes through the mTORC1 pathway and accordingly increased protein synthesis. Downregulation of *FGFR4* in classical/progenitor cell lines invariably led to the enrichment of basal-like/squamous gene programs which was associated with either partial of full switch of phenotype. Overall, our data provide direct evidence that the loss of FGFR4 promotes aggressive phenotypes of PDAC.

RESULTS

FGFR4 is associated with the classical phenotype of PDAC

Receptor-Tyrosine Kinases (RTKs) initiated signaling is critical to cell fate determination (Lemmon et al., 2010; Neben et al. 2019). To investigate the functional relevance of RTKs in determining PDAC cell lineages and promoting its malignant phenotype, we started by exploring transcriptomic data of human PDAC specimens from the TCGA consortium (Cancer Genome Atlas Research Network, 2017) and found the selective enrichment of *FGFR4* in the classical subtype (**Fig. 1A, B**). We reproduced this finding in transcriptomic data from two additional cohorts (Bailey et al., 2016; Chan-Seng-Yue et al., 2020) (Fig. 1B). While relatively enriched in basal-like PDAC (Fig. 1A), the expression of *FGFR1* did not significantly discriminate basal-like from classical tumours in the 3 PDAC cohorts (Bailey et al., 2016; Cancer Genome Atlas Research Network, 2017; Chan-Seng-Yue et al., 2020) investigated (Fig. 1B). Next, we explored available single-cell RNA-Seq (scRNA-Seq) data of human PDAC tissues to localise the expression of both FGFR1 and FGFR4. We integrated four PDAC scRNA-seq data sets (Chan-Seng-Yue et al., 2020; Lin et al., 2020; Peng et al., 2019; Steele et al., 2020) using Harmony (Korsunsky et al., 2019) and performed cell type annotation to find that FGFR4 is predominantly expressed by epithelial cells, while *FGFR1* could be detected in epithelial, stromal (fibroblasts, endothelial cells), and immune cells (i.e. macrophages) (**Fig. 1C**). Next, we explored scRNA-seq data from normal pancreas (Muraro et al., 2016; Grün et al., 2016; Segerstolpe et al., 2016) (Supplementary Fig. 1A) and found that the expression of *FGFR4* is mostly restricted to the epithelial cells while *FGFR1* is detectable in many cell types. *In situ* hybridisation (ISH) analyses of normal pancreatic tissues confirmed scRNA-seq data (Supplementary Fig. 1B). To better understand the association of epithelial FGFRs expression with PDAC molecular subtypes, we then focused on transcriptomic datasets derived from either tissue with high neoplastic cellularity (i.e. ICGC (Bailey et al., 2016), average qPure score > 60%) or microdissected neoplastic epithelia (i.e. PanCuRx (Chan-Seng-Yue et al., 2020)). First, we divided samples of the two cohorts in four different groups based on *FGFR1* and *FGFR4* expression

statuses (see methods and Supplementary Fig. 1C). To explore the association of *FGFR1* and *FGFR4* with the aggressive basal-like and squamous molecular subtypes as defined by Moffitt (Moffitt et al., 2015) and Bailey (Bailey et al., 2016) (**Fig. 1D**, Supplementary Fig. 1D), we calculated the basal-like and squamous signature scores for each sample of the ICGC and the PanCuRx cohorts (Bailey et al, 2016; Chan-Seng-Yue et al., 2020) (see methods). Tumours with low levels of *FGFR4* showed the highest basal-like/squamous scores regardless of the *FGFR1* status (either high or low); indeed, the signature scores between the FGFR4^{low}FGFR1^{high} and FGFR4^{low}FGFR1^{low} were not significantly different (Fig. 1D and Supplementary Fig. 1D). Accordingly, all the FGFR4^{high} tumours of the ICGC cohort classified as classical, while only 9.7% (13/134) of the FGFR4^{high} tumours of the PanCuRx were defined as basal-like (Supplementary Fig. 1E). These results were substantially similar to those obtained when tumours of the two cohorts were separated based on the expression level of the known classical driver GATA6 (Supplementary Fig. 1F). When using the molecular classification proposed in the PanCuRx study (Chan-Seng-Yue et al., 2020), the group of FGFR4^{low} tumours was highly enriched for basal subtypes (Supplementary Fig. 1G). Reduced FGFR4 expression in PDAC tissues from the ICGC (Bailey et al., 2016) was associated with inferior overall survival (**Fig. 1E**). Conversely, the levels of *FGFR1* had no prognostic significance in different PDAC cohorts (n = 3, data not shown). To corroborate these findings, we used ISH to evaluate the expression of FGFR1 and FGFR4 in a cohort of 106 human pancreatic tissues from treatment naïve patients (**Fig. 1F**, Supplementary Fig. 2A). A total of 97 tissues were suitable for evaluation of both FGFRs. We confirmed that FGFR4 is expressed by epithelial cells while FGFR1 is prominent in stromal elements (Fig. 1F and Supplementary Fig. 2A). Low expression of FGFR4 was observed in 23% (22/97) of cases (**Fig. 1G**) and was significantly enriched in high grade tumours (Supplementary Fig. 2B). Furthermore, FGFR4 was never detected in poorly differentiated areas while detectable with variable degree of expression in well-differentiated tumour glands (Supplementary Fig. 2C). Finally, low expression of FGFR4 identified patients showing inferior overall survival in our cohort (**Fig. 1H**). To identify suitable human models for genetic manipulation of the two FGFRs, we screened an initial

array of cell lines (n = 6) and Patient-derived Organoids (n = 5). In accordance with our results, ISH analyses of 6 human PDAC cell lines revealed high FGFR4 in cells displaying an epithelial phenotype (Supplementary Fig. 2D–F), and higher levels of FGFR1 in mesenchymal-like cells showing expression of ZEB1 and/or Vimentin (Supplementary Fig. 2D–F). For PDOs, RNA-seq was used to classify cultures as either classical or basal-like using single-sample Gene Set Variation Analysis (ssgsea method) (Hänzelmann et al., 2013). Of note, the organoid culture with the highest basal-like/squamous identity (PDA9-O) showed the lowest expression of FGFR4 (Supplementary Fig. 2G), thus representing a model for FGFR4^{low} basal-like tumours.
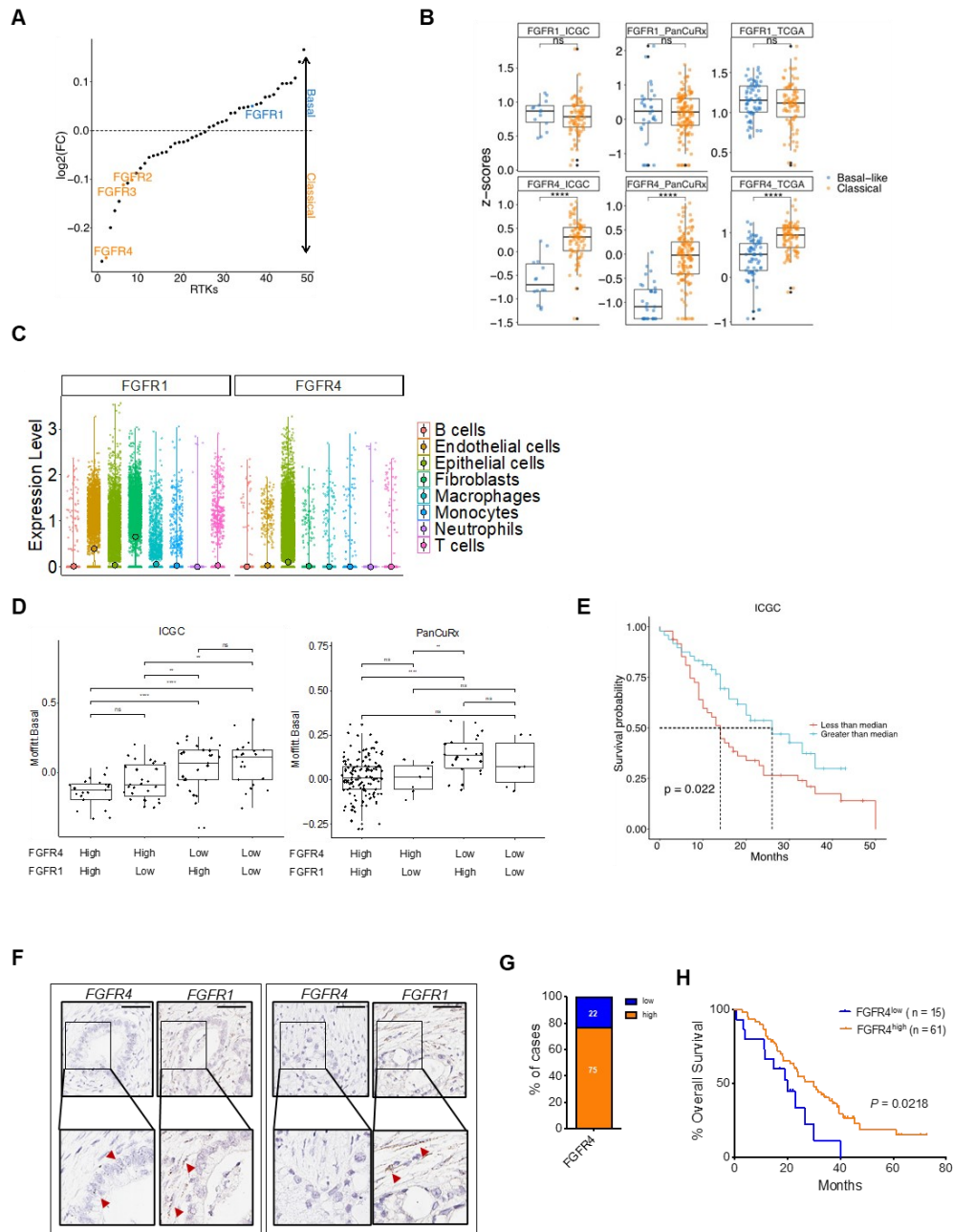
Fig. 1: FGFR4 is differentially expressed in PDAC molecular subtypes. A Receptor Tyrosine Kinases (RTKs) expression in basal-like and classical subtypes. The scatter plot shows the expressed RTK ranked by their mean log2 fold change in basal-like versus classical for samples of the TCGA cohort (Cancer Genome Atlas Research Network, 2017). Highlighted: FGFR1, FGFR2, FGFR3, FGFR4. **B** Boxplot of *FGFR1* (left) and *FGFR4* (middle) Z-scores stratified by the Moffitt subtypes (Moffitt et al., 2015) in the TCGA (Cancer Genome Atlas Research Network, 2017), ICGC (Bailey et al., 2016), and PanCuRx (Chan-Seng-Yue et al., 2020) datasets. ****p < 0.0001; and ns, not significant as determined by Wilcoxon test. **C** Violin plots of the normalised expression of *FGFR1* (left panel) and *FGFR4* (right panel) in each annotated cell cluster from the integration of four different scRNA-seq datasets of PDAC tissues (Chan-Seng-Yue et al., 2020; Lin et al., 2020; Peng et al., 2019; Steele et al., 2020) (see methods). **D** GSVA score (using ssgsea

method) for the basal-like signature (Moffitt et al., 2015) for each sample of the ICGC (Bailey et al., 2016) and PanCuRx (Chan-Seng-Yue et al., 2020) cohort according to the expression of *FGFR1* and *FGFR4*. **p < 0.01; ****p < 0.0001; and ns, not significant as determined by Wilcoxon test. **E** Kaplan–Meier plot comparing the overall survival of patients from the ICGC cohort (Bailey et al., 2016) (n = 96) according to the expression of FGFR4. p, Log-rank (Mantel–Cox) test. **F** Representative ISH images showing expression of *FGFR4* and *FGFR1* in two different pancreatic cancer tissues. Scale Bar, 50 μm. Insets show magnification of selected areas, and red arrowheads indicate either epithelial or stromal cells. **G** Stacked bar plot showing the percentage of PDAC tissues (n = 97) with either low (blue) or high (orange) expression of *FGFR4*. **H** Kaplan–Meier plot comparing the overall survival of patients according to *FGFR4* ISH status. p, Log-rank (Mantel–Cox) test.

FGFR1 is a functional marker of EMT in PDAC

The interrogation of the genomic data from the ICGC (Bailey et al., 2016) and TCGA (Cancer Genome Atlas Research Network, 2017) cohorts in cBioportal (https://www.cbioportal.org) revealed no recurrent genetic alteration affecting FGFR1 in PDAC (Supplementary Fig. 3A, B). We then looked at the correlation between FGFR1 and the established markers/drivers of PDAC cell phenotypes. In all the interrogated transcriptomic datasets (n = 5) (Bailey et al., 2016; Cancer Genome Atlas Research Network, 2017; Chan-Seng-Yue et al., 2020; Moffitt et al., 2015; Balli et al., 2017), FGFR1 expression positively correlated with the expression of EMT genes, in particular with the master regulator ZEB1, yet not with expression of squamous lineage genes (TP63, KRT5, KRT14) (**Fig. 2A**). To corroborate the suggested link with EMT, we found a significant positive correlation between the Hallmark EMT signature and *FGFR1* in samples from the TCGA cohort (Cancer Genome Atlas Research Network, 2017) (**Fig. 2B**). Next, we investigated whether induction of EMT or downregulation of its master regulator ZEB1 would affect expression of FGFR1. Following 48 h of TGFβ1 treatment, the SMAD4-proficient cell line hM1 displayed significant elevation in the expression of several EMT markers/drivers as well as of FGFR1 both at mRNA and protein levels (**Fig. 2C**). The mRNA levels of *CDH1* and *FGFR4* were only moderately affected by the treatment. Furthermore, the transient downregulation of ZEB1 in the PDAC cell line showing the more prominent mesenchymal-like phenotype (i.e. Hs766t, PANC1) led to a significant reduction in the expression of *FGFR1*, while increasing expression of *FGFR4* and the classical gene *CDH1* (**Fig. 2D**). Then, we sought to assess the functional consequences of FGFR1 inhibition in PDAC. First, we treated 7 human PDAC cell lines with increasing concentrations of the FGFR1 inhibitor BGJ398 (Guagnano et al., 2011) and measured cell viability using an ATP-based assay (**Fig. 2E**). Four out of the seven cell lines tested were primary cell lines (PDA2, PDA9, PDA23, PDA6), which were classified as either basal-like or classical based on RNA-Seq data (Supplementary Fig. 3D and data not shown). BGJ398 demonstrated poor activity and modestly affected proliferation of PDA2, hT1, and of Hs766T only at the highest dose (1 μM) (**Fig. 2E**). Then, we performed genetic depletion of FGFR1 by RNA interference approaches. Stable silencing of

FGFR1 in PANC1 was associated with reduced protein expression of the EMT driver ZEB1 but not of the marker Vimentin (**Fig. 2F**). *In vitro* proliferation of Hs766T, but not of PANC1, was significantly reduced following downregulation of FGFR1 (**Fig. 2G**). However, orthotopically transplanted PANC1 cells deficient for FGFR1 generated smaller tumours compared to parental cells transduced with the empty vector (**Fig. 2H**), thus suggesting cell extrinsic effects of FGFR1 downregulation in this cell line. In addition, we performed RNAi-based competition assay in the basal-like PDA9-O which displayed the highest protein levels of FGFR1 among the organoid cultures investigated. We observed the progressive drop-out of the vector targeting FGFR1 (Supplementary Fig. 3E), suggesting that FGFR1 is advantageous for the proliferation of this organoid culture. We next sought to explore whether loss of FGFR1 in a basal-like background could lead to changes in PDAC cell identity. Using RNAi, we targeted FGFR1 in the basal-like Hs766T (PDX1−CK5+, Supplementary Fig. 2E) and performed RNA-Seq analysis (Supplementary Fig. 3F). GSEA demonstrated that the loss of FGFR1 led to alteration of genes programs related to cell proliferation and Interferons' response (Supplementary Fig. 3G). However, the loss of FGFR1 did not lead to significant changes in subtype expression signatures and accordingly FGFR1-deficient cells were classified as basal-like (**Fig. 2I**). Conversely, downregulation of FGFR1 led to the significant reduction of the EMT transcriptional phenotype (**Fig. 2J**). In sum, our analysis reveals that FGFR1 is a functional driver of EMT in pancreatic cancer.
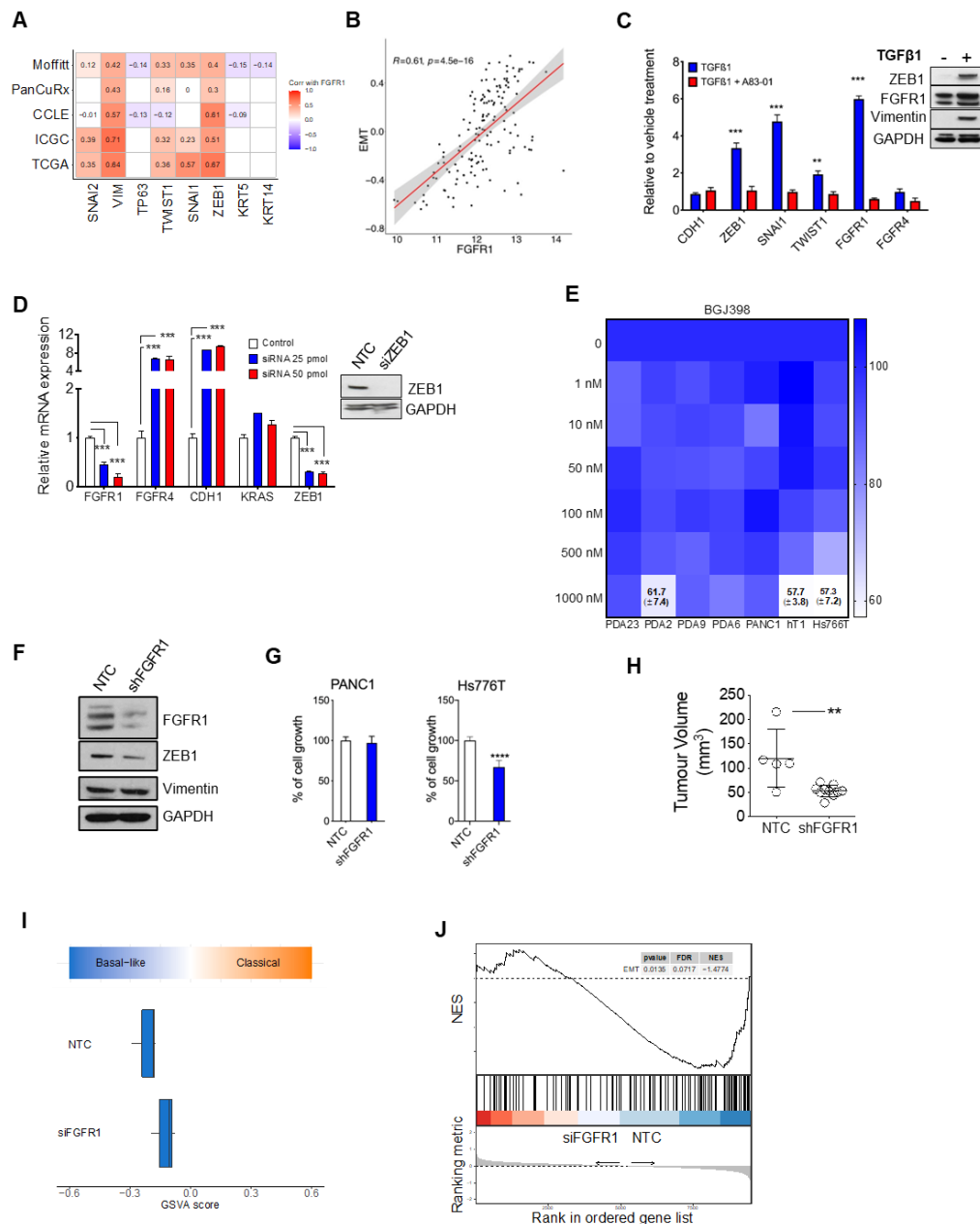
Fig. 2: FGFR1 is a functional marker of EMT in PDAC. A Heatmap showing correlation (Spearman's correlation) between FGFR1 and the squamous lineage markers, and the EMT genes in five different transcriptomic datasets (Bailey et al., 2016; Cancer Genome Atlas Research Network, 2017; Chan-Seng-Yue et al., 2020; Moffitt et al., 2015; Balli et al., 2017). All annotated boxes, $p < 0.001$ **B** Scatter plot showing the positive correlation between FGFR1 mRNA expression and the Epithelial-to-Mesenchymal Transition (EMT) signature score from MsigDB for the TCGA cohort (Cancer Genome Atlas Research Network, 2017). **C** Changes in the expression level of the indicated genes in hM1 cell line treated with 5 ng/mL of TGFβ1 alone or in combination with 500 nM of TGFβ1 inhibitor (A83-01) for 48 h. On the right, immunoblot analysis of ZEB1, FGFR1, and Vimentin in whole-cell lysates from hM1 treated with 500 nM TGFβ1 for 48 h. GAPDH was used as loading control. **D** Changes at 48 h in the expression level of the indicated genes in the Hs766T cell line transfected with either mock control or two different concentrations of

siRNAs targeting ZEB1. On the right, immunoblot analysis of ZEB1 in whole-cell lysates of PANC1 transfected with non-targeting control (NTC) or 25 pmol of siRNA against ZEB1. GAPDH was used as loading control. In (C and D), results shown as mean ± SD of three replicates. **$p < 0.01$; ***$p < 0.001$ as determined by Student's t test. **E** Cell viability of PDAC monolayer cultures treated with BGJ398 (n = 7 cell cultures) as indicated. Data are displayed as heatmap of the percentage of inhibition at each dose of the drugs and presented as mean of three independent experiments. **F** Immunoblot analysis of FGFR1, ZEB1, and Vimentin in whole-cell lysates of PANC1 cells stably expressing the control vector (NTC) or the shRNA targeting FGFR1 (shFGFR1). GAPDH was used as loading control. **G** Relative growth (as percentage of cell proliferation) of PANC1 and Hs766T cells stably transduced with either the control vector (NTC) or the vector targeting FGFR1. Data presented are means ± SD of three biological replicates. **H** Scatter dot plot showing differences in tumour volumes between tumour-bearing mice transplanted with PANC1/NTC (n = 5 mice) or PANC1/shFGFR1 (n = 10 mice). Tumour volumes were measured by ultrasound 5 weeks after transplantation. **$p < 0.01$ as determined by Student's t test. **I** Boxplots of GSVA score (based on ssgsea method) for the Classical and the Basal-like signatures calculated for the Hs766T cell line transfected with non-targeting control or siRNA against FGFR1. **J** GSEA plot evaluating the EMT signature upon FGFR1 knockdown in Hs766T cell line.

FGFR4 is epigenetically downregulated in basal-like/squamous PDAC

The reduced expression of FGFR4 in aggressive subtypes of PDAC might be due to either genetic or epigenetic mechanisms. First, we explored the genomic data from the ICGC (Bailey et al., 2016) and TCGA (Cancer Genome Atlas Research Network, 2017) cohorts and found no recurrent genetic alterations affecting FGFR4 (Supplementary Fig. 3A, C). Therefore, we interrogated the available methylation data from the ICGC cohort (Bailey et al., 2016) and found that the downregulation of FGFR4 in the squamous subtype was associated with hypermethylation of the gene (**Fig. 3A**). Next, we reanalysed data from Diaferia et al. (Diaferia et al., 2016) that used ChIP-Seq to profile marks indicative of either active (e.g. H3K27ac) or inactive (e.g. H3K9me3) chromatin in PDAC cell lines representative of classical and basal-like tumours. We found that the genomic region proximal to the FGFR4 transcription start site showed differential levels of H3K27ac between basal-like and classical cell lines, with changes that were concordant with higher level of transcripts in the classical cell line (**Fig. 3B** and Supplementary Fig. 4A). A broader peak of the active enhancer chromatin mark H3K4me1 was observed for the classical cell line in the intron 1 of FGFR4 gene (Fig. 3B), which has been reported to contain an enhancer region (Shah et al., 2013). In keeping with that, FGFR4 expression positively correlated with the expression of endodermal transcription factors and epithelial genes (*CDH1* and *ERBB3*) (**Fig. 3C**) in 5 different transcriptomic datasets of PDAC (Bailey et al., 2016; Cancer Genome Atlas Research Network, 2017; Chan-Seng-Yue et al., 2020; Moffitt et al., 2015; Balli et al., 2017). In particular, FGFR4 showed significant positive correlation with the transcription factor HNF1A in all datasets (**Fig. 3C**). Accordingly, putative target genes of HNF1A were significantly enriched in FGFR4 high tumours of the ICGC cohort (**Fig. 3D**). To prove direct regulation by the transcription factor, we reanalysed available data from pancreas-specific knockout of Hnf1a (Kalisz et al., 2020). In Hnf1a-deficient versus proficient pancreatic cells, expression of Fgfr4 was significantly reduced and this was concordant with genomic regions proximal to the transcription start site of Fgfr4 showing reduced occupancy by HNF1A and reduced levels of H3K27ac (**Fig. 3E**). Overall, our analysis strongly suggests that

FGFR4 is a marker of the classical subtype whose expression is epigenetically reduced in basal-like PDAC cells.

HNF1A blocks EMT in a classical PDAC cell line

To confirm the link between HNF1A and FGFR4 in the human PDAC setting, we manipulated the expression of HNF1A by RNAi in HPAF-II, which has been reportedly used as a model of classical PDAC (Diaferia et al., 2016; Somerville et al., 2018). The successful downregulation of HNF1A was associated with the reduced expression of FGFR4 and increased expression of both ZEB1 and FGFR1 (**Fig. 3F**). Downregulation of HNF1A was associated with substantial changes in the transcriptome of the HPAF-II cell line (Supplementary Fig. 4B) and gene-set enrichment analysis (GSEA) (Subramanian et al., 2005) showed the enrichment of several pathways and terms related to extracellular matrix organization/deposition and the EMT (**Fig. 3G**). Of the marker/drivers of PDAC epithelial subtypes, only HNF4A was significantly downregulated upon HNF1A knockdown (**Fig. 3H**). In keeping with a recent work (Kloesch et al., 2022), HFN1A downregulation was not sufficient to drive a full phenotype switch in HPAF-II cell line. Yet, HNF1A silencing significantly increased the expression of genes defining the basal-like signature (Moffitt et al., 2015) as assessed by GSEA (**Fig. 3I**).
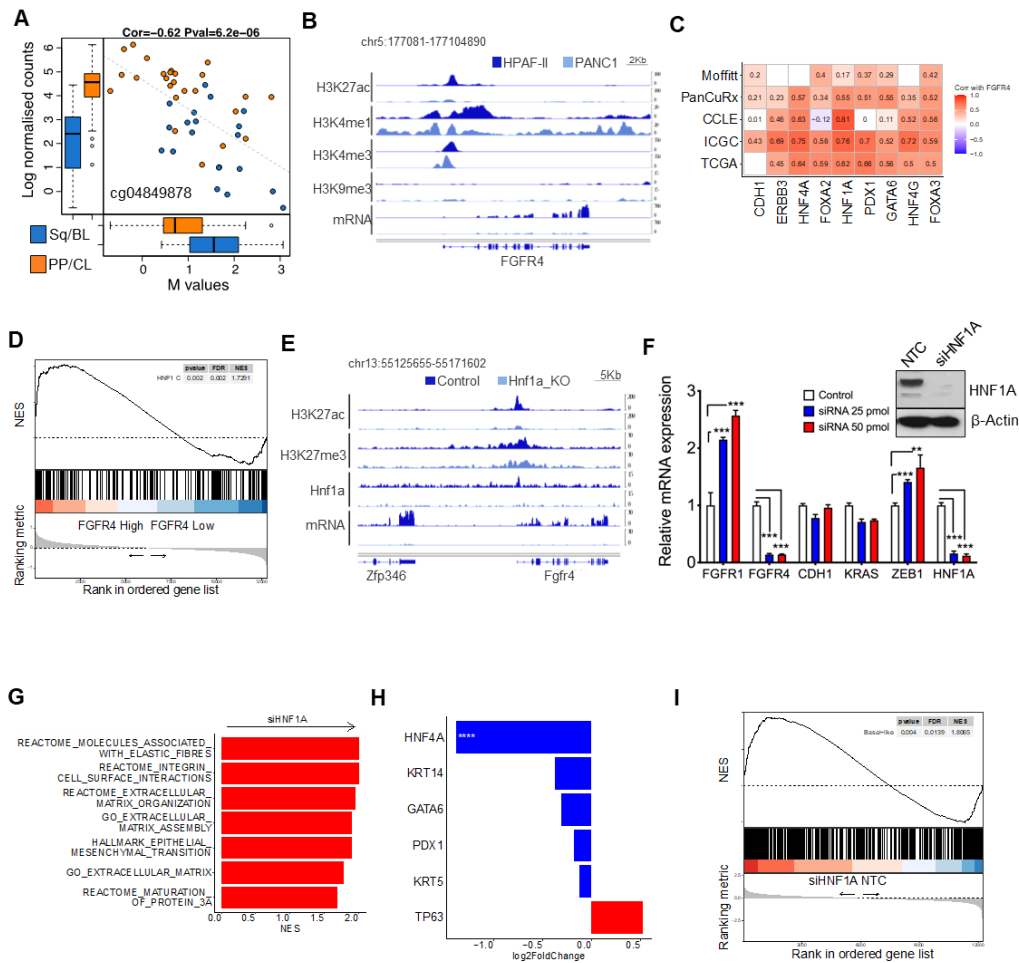
Fig. 3: Expression of FGFRs4 and determinants of molecular subtypes. A Hypermethylation of FGFR4 in squamous/basal-like tumours (blue) from the ICGC cohort (Bailey et al., 2016) is concordant with the downregulation of the gene. Indicated is the CpG probe showing the highest correlation. **B** Representative snapshot of the genomic region of FGFR4 in PANC1 (high-grade, basal-like) and HPAF-II (low-grade, classical) from Diaferia et al. (Diaferia et al., 2016) showing histone modifications (H3K27ac, H3K4me1, H3K4me3, H3K9me3) and RNA-seq data. **C** Heatmap showing correlation (Spearman's correlation) between FGFR4 and the expressed endodermal transcription factors and epithelial genes in five different transcriptomic datasets (Bailey et al., 2016; Cancer Genome Atlas Research Network, 2017; Chan-Seng-Yue et al., 2020; Moffitt et al., 2015; Balli et al., 2017). All annotated boxes, p < 0.001. **D** GSEA plot evaluating the enrichment of the geneset containing putative HNF1A target genes when comparing FGFR4 high versus FGFR4 low tumours of the ICGC cohort (Bailey et al., 2016). **E** Representative snapshot of the genomic region of Fgfr4 in mouse pancreatic cells proficient (control) or deficient (Hnf1a_KO) for HNF1A from Klasniz et al. (Kalisz et al., 2020) showing histone modifications (H3K27ac, H3K27me3), HNF1A occupancy, and RNA-seq data. **F** Changes in the expression levels of the indicated genes in the HPAF-II cell line transfected with either mock control or two different concentrations of siRNA against HNF1A. Results are shown as mean ± SD of three replicates. ***p < 0.001 as determined by Student's t test. On the right, immunoblot analysis of HNF1A in whole-cell lysates of

HPAF-II transfected with either non-targeting control (NTC) or 25 pmol of siRNA targeting HNF1A. β-Actin was used as loading control. **G** Enrichment of selected pathways upon HNF1A knockdown. The GSEA analysis was performed using gene sets from REACTOME, GO, Hallmark, and REACTOME databases in MsigDB library. Displayed gene sets that passed false-discovery rate < 0.05. **H** Expression of classical and basal-like genes in HNF1A-deficient HPAF-II cells (compared to parental cells) from RNA-Seq data. Data are presented as mean $\pm$ SD. ****, $p < 0.0001$ by Student t test. **I** GSEA plot evaluating the basal-like signature upon depletion of HNF1A in HPAF-II cell lines.

Loss of FGFR4 enhances the malignant behaviour of PDAC cells

To evaluate the functional relevance of FGFR4 in dictating PDAC phenotypes, we performed genetic and pharmacological perturbation experiments (**Fig. 4** and Supplementary Fig. 4). Cell viability of established cell lines and primary PDAC cells (n = 7) was not significantly inhibited by the continuous treatment with the FGFR4 inhibitor BLU9331 (Hagel et al., 2015) (FGFR4i) (Fig. 4A). Of note, low doses of FGFR4i slightly increased the proliferation of some PDAC cell lines. Also considering the dose-response analysis of PDAC cells with the FGFR1 inhibitor BGJ398 (Fig. 2E), our results show that pharmacological inhibition of FGFRs is not a viable strategy to reduce PDAC cells proliferation. Next, we targeted FGFR4 in the classical cell line HPAF-II using three different shRNAs (**Fig. 4B**). FGFR4 was successfully downregulated by all shRNAs with the #884 and the #419 showing the highest and lowest efficiency, respectively (Fig. 4B). The majority of results were obtained using the two most efficient shRNA, namely #884 and #885. Loss of FGFR4 in HPAF-II cell line was associated with downregulation of the epithelial markers E-Cadherin and ERBB3 (Fig. 4B) and increased *in vitro* proliferation (**Fig. 4C**). Interestingly, downregulation of FGFR4 expression altered the proliferative response to three different FGF ligands (**Fig. 4D**). In particular, continuous treatment with FGF2 and FGF19 significantly reduced the proliferation of control HPAF-II cell line but did not affect the proliferation of cells displaying downregulation of FGFR4 (Fig. 4D). Furthermore, we orthotopically transplanted HPAF-II transduced with non-targeting and targeting vectors into immunocompromised mice and monitored tumour growth for 4 weeks. At the experimental endpoint, loss of FGFR4 in HPAF-II cell line generated larger tumours with increased number of mitotic figures (**Fig. 4E**, and data not shown), and significantly increased the metastatic burden at the lungs and the liver (**Fig. 4F**). In agreement with that, the group of FGFR4^{low} tumours of the PanCuRx cohort (Chan-Seng-Yue et al., 2020) was significantly enriched for metastases (Supplementary Fig. 4C). The *in vivo* pro-tumorigenic effect driven by the loss of FGFR4 was further validated in organoid-based xenografts with the classical PDO hT3 (Supplementary Fig. 2G). Immunodeficient mice we orthotopically transplanted with equal number of cells from either parental PDOs (n = 7) or

cultures stably transduced with the shRNA targeting FGFR4 (n = 7) (Supplementary Fig. 4D). We monitored tumour growth with high-contrast ultrasound imaging starting at day 15 post transplantation. In agreement with the results obtained with established cell lines, PDOs expressing high levels of FGFR4 displayed reduced proliferation *in vivo* (**Fig. 4G**) and less efficient engraftment rate at earlier time points as only 1 out of 7 transplanted mice showed a detectable mass at day 15 as opposed to the FGFR4 deficient PDO (5/7 mice with detectable masses). Finally, we downregulated FGFR4 in the organoid model of FGFR4^{low} basal-like tumours (PDA9-O) prior to *in vivo* transplantation in immunocompromised hosts. At the endpoint, the tumour masses were significantly larger in animals transplanted with FGFR4 deficient cells (**Fig. 4H**). ISH analyses of transplanted tissues confirmed the downregulation of FGFR4 as opposed to control mice (**Fig. 4I** and Supplementary Fig. 4E). To further generalise our results, we transiently downregulated FGFR4 in four PDAC cell lines (including HPAF-II) and observed increased proliferation regardless of the molecular subtype of the cells (Supplementary Fig. 4F). In agreement with that, GSEA comparing the transcriptomes of FGFR4^{low} versus FGFR4^{high} tumours in the ICGC cohort revealed the significant enrichment of terms related to "cell proliferation" and "cell cycle" in FGFR4^{low} PDAC (Supplementary Fig. 4G). Overall, these data suggest that endogenous levels of FGFR4 limit the malignant phenotype of PDAC regardless of the genetic background of the cells.
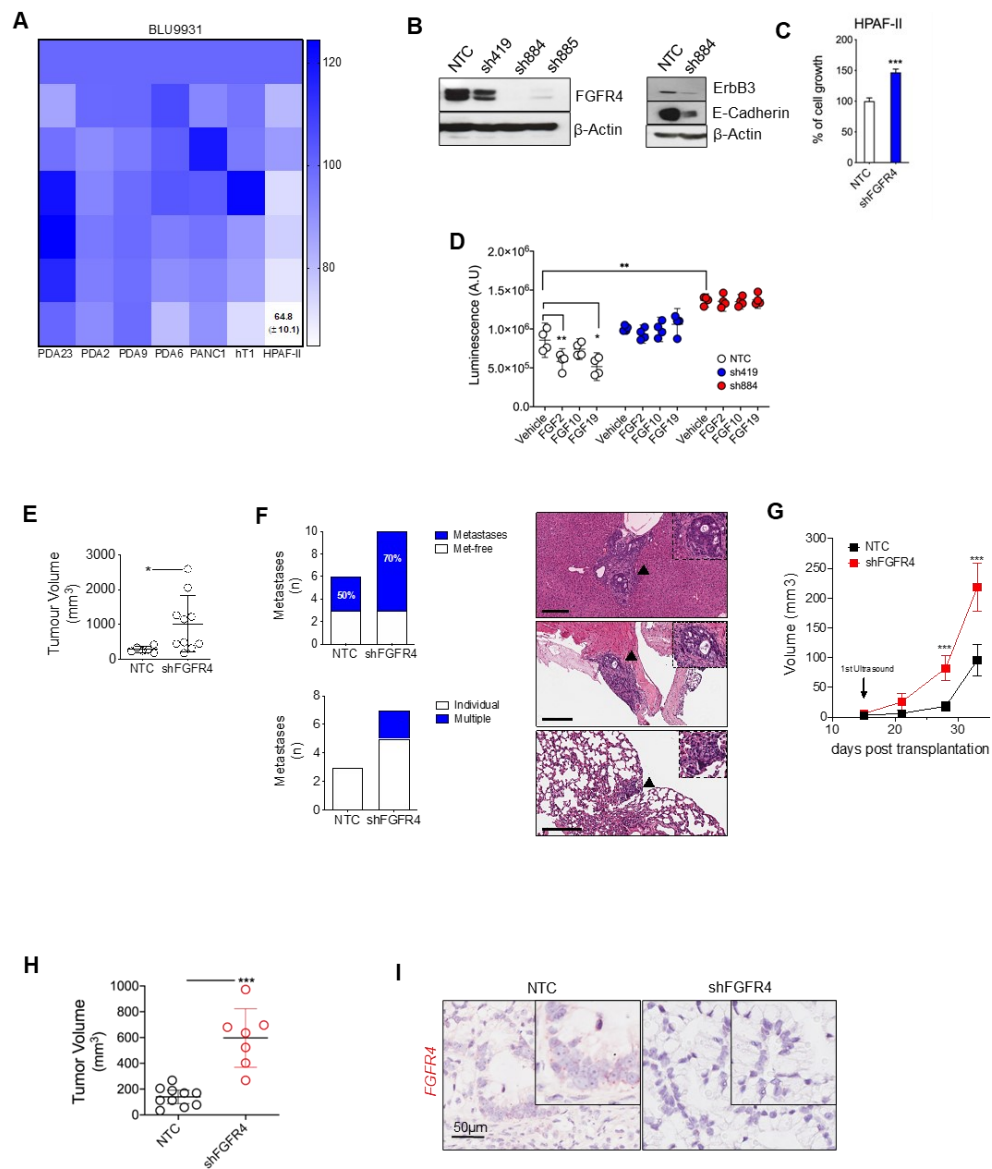
Fig. 4: Loss of FGFR4 is associated with an aggressive PDAC biological behaviour. A
Cell viability of PDAC monolayer cultures treated with BLU3391 (n = 7 cell cultures) as
indicated. Data are displayed as heatmap of the percentage of inhibition at each dose of the
drugs and presented as mean of three independent experiments. **B** Immunoblot analysis of
FGFR4, ErbB3, and E-Cadherin (loading control, β-Actin) in HPAF-II stably expressing
the control vector (NTC) or the construct targeting FGFR4 (shFGFR4). **C** Relative growth
(as percentage of cell proliferation) of HPAF-II cells stably transduced with either the
control vector (NTC) or the vector targeting FGFR4 (#884). Data presented are means ± SD
of three biological replicates. **D** Proliferation (as total luminescence) of HPAF-II cell line
stably transduced with NTC or two different short hairpin RNA against FGFR4 (#419 and
#884) following 48 h stimulation with FGF2 (25 ng/mL), FGF10 (100 ng/mL), and FGF19
(100 ng/mL). Data presented as means ± SD (n = 3 biological replicates). *p < 0.05; and
p < 0.01 as determined by Student's t test. **E Scatter dot plot showing differences in
tumour volumes between tumour-bearing mice transplanted with HPAF-II/NTC (n = 6
mice) and HPAF-II/shFGFR4 (n = 10 mice). Tumour volumes were measured by
ultrasound 4 weeks after transplantation. *p < 0.05 as determined by Student's t test. **F**
Stacked bar plot showing the distribution of mice with or without metastatic lesions in the

two different cohort of mice from (E) (upper panel). Lower panel, stacked bar plot showing the number of mice with individual or multiple metastatic lesions in the two different cohort from (E). On the right, representative Hematoxylin and Eosin staining of metastatic lesions at the liver (top and middle) and at the lungs (bottom) from a mouse bearing multiple metastases. The black arrows indicate the areas shown in the insets. Scale bar, 200 μm. **G** Line graph showing tumour volumes (mm3) of pancreatic masses detected upon the orthotopic injection of 1×106 cells from hT3 PDO into immunodeficient mice (n = 7). Means ± SD are shown. Mice were screened at 15, 21, 27, 32 days following transplantation. ****$p < 0.001$ by two-way ANOVA with Sidak's test for multiple comparison. **H** Scatter plot showing the difference in tumour volumes between mice transplanted with PDA9 organoids either transduced with control vector (n = 10 mice) or with shFGFR4 (n = 7 mice). Tumour volumes were measured by ultrasound 4 weeks after transplantation. ***$p < 0.01$ as determined by Student's t test. **I** Representative in situ hybridisation staining of FGFR4 in PDA9-O in mice from (H) and showing loss of FGFR4 in vivo. Scale bar, 50 μm.

Loss of FGFR4 is associated with increased basal-like/squamous features in PDAC

We next sought to explore whether loss of FGFR4 in a classical background could lead to changes in PDAC cell identity. FGFR4 knockdown in HPAF-II cells led to substantial changes in the transcriptome of this classical cell line (**Fig. 5A**). Similarly, FGFR4 knockdown led to profound changes in the expression of genes that drive the signatures of molecular subtypes of PDAC (**Fig. 5B**) and deficient cells were classified as basal-like (**Fig. 5C**) suggesting that, in this cell line, FGFR4 is a superior barrier to the expression of ectopic gene programs (i.e. basal-like) compared to HNF1A. We then looked at changes in the expression of markers/drivers of subtype following FGFR4 silencing and found reduced expression of CDH1 (**Fig. 5D**), which is consistent with the reduction of E-cadherin (protein level) following stable knockdown (Fig. 4B). Of transcription factors previously associated with the basal-like/squamous lineage, ZBED2 showed the most prominent upregulation upon FGFR4 silencing (Fig. 5D). ZBED2 has been recently demonstrated to antagonise the action of interferon regulatory factor 1 (IRF1), to be selectively enriched in squamous tumours, and to prevent the growth arrest induced by Interferon in PDAC cells (Somerville et al., 2020). Accordingly, silencing of FGFR4 led to downregulation of gene sets related to interferon pathway in HPAF-II (**Fig. 5E**) while increasing for the expression of gene programs related to c-Myc activity and EMT. To corroborate our findings, we interrogated RNA-seq from patients' tissues and found that ZBED2 is the gene whose expression is more prominent in FGFR4 low tumours of the ICGC cohort (Supplementary Fig. 5A). Furthermore, GSEA comparing the transcriptomes of FGFR4^{low} versus FGFR4^{high} tumours in both the ICGC and PanCuRx cohorts revealed the significant downregulation of terms related to "Interferon" in FGFR4^{low} PDAC (**Fig. 5F** and Supplementary Fig. 5B). To further generalise our results and understand whether the effect of FGFR4 downregulation on PDAC cell lineages is context dependent, we targeted the receptor by RNAi in two additional models of classical/progenitor (i.e. epithelial) PDAC: AsPC1 and SUIT2. These two cell lines have been extensively used to identify the molecular barriers to the expression of basal-like/squamous programs in PDAC (Kloesch et al., 2022; Somerville et al., 2018)

and display high expression of FGFR4 (Supplementary Fig. 5C). Differently from HPAF-II, the forced downregulation of FGFR4 in these two models did not lead to a full switch of phenotype (Supplementary Fig. 5C). Nevertheless, the loss of FGFR4 led to the reduction of classical/progenitor programs and of the epithelial marker E-cadherin, the enrichment of transcriptional signatures of basal-like/squamous PDAC and of genesets related to increased proliferation and c-Myc activity (**Fig. 5G**, Supplementary Fig. 5D–H). While suggesting that the effect on "full subtype switch" is cell-context dependent, our results strongly suggest that FGFR4 limits the expression of gene programs of aggressive (i.e. basal-like/squamous) PDAC. To further ascertain whether FGFR4 expression is associated with changes in the expression of gene and gene programs of the two PDAC subtypes in human tissues, we interrogated the scRNA-Seq data from Peng et al. (Peng et al., 2019). First, we confirmed the enrichment for FGFR4^{high} cells in the epithelial compartment of patients displaying the classical phenotype (Supplementary Fig. 5I). Then, we separated cases with lowest and highest expression of FGFR4 (Supplementary Fig. 5J) to find that those with elevated epithelial expression of FGFR4 accordingly displayed elevated expression of classical markers (Supplementary Fig. 5K). Furthermore, FGFR4^{low} cells were characterised by gene expression programs of basal-like/squamous subtypes (**Fig. 5H**), which included EMT related gene sets. Finally, we sorted out basal-like and classical cells from those cases and compared the transcriptome of cells displaying high and low expression of FGFR4. In line with the suggested role for FGFR4 in sustaining the classical phenotype, classical cells with the highest expression of FGFR4 displayed elevated expression of classical genes (**Fig. 5I**). Similarly, even within basal-like cells those with the highest expression of FGFR4 displayed elevated level of classical/epithelial PDAC while the ones with reduced expression of the gene showed increased expression of basal-like/squamous markers (Fig. 5I).
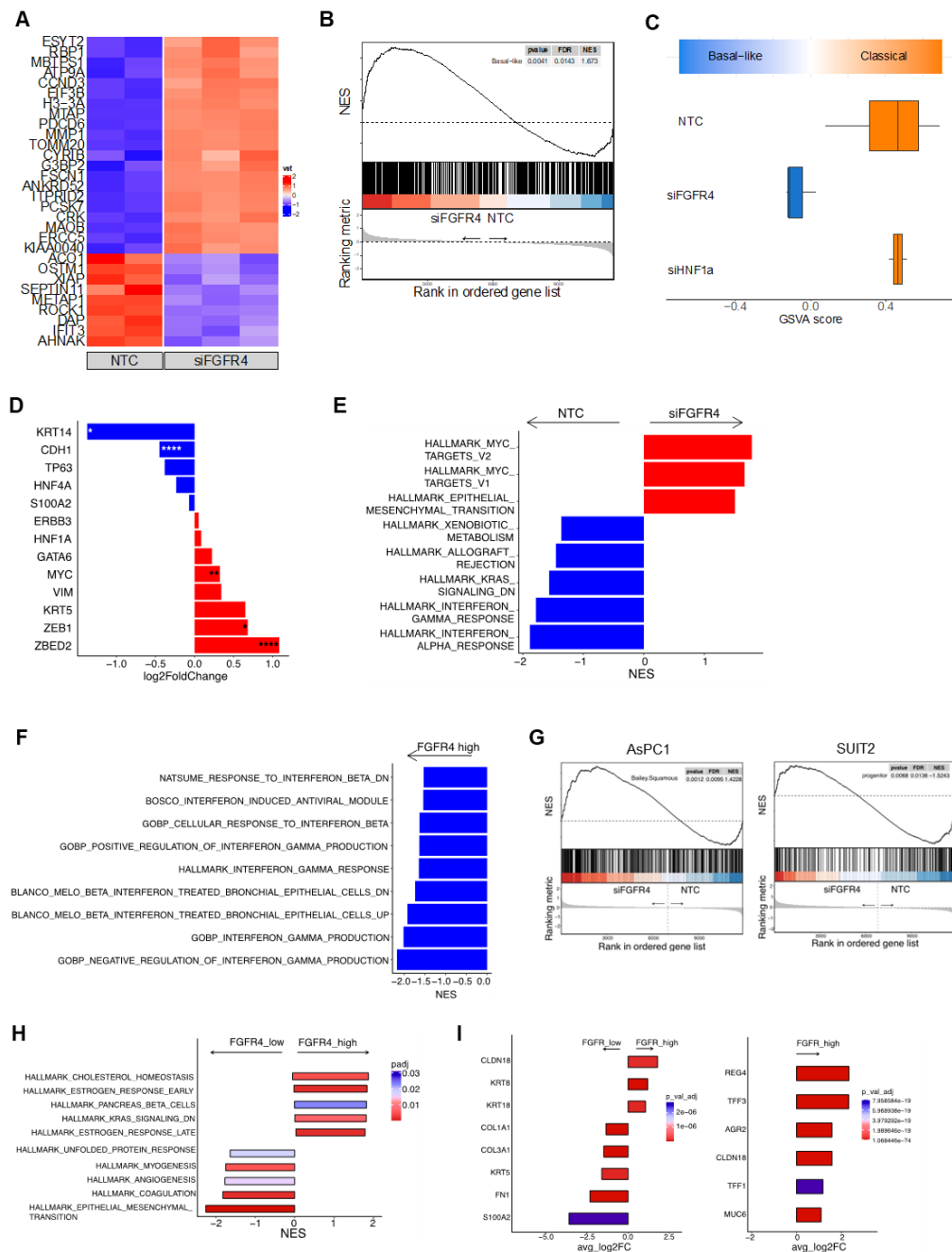
Fig. 5: FGFR4 loss leads to the expression of basal-like/squamous programs in PDAC. **A** Heatmap showing changes in the expression pattern of the 30 most differentially expressed genes in the comparison between: control and FGFR4 knock-down (siFGFR4). Z-scores derived from DESeq2-VST transformed counts. **B** GSEA plot evaluating the Basal-like signature upon FGFR4 knockdown in HPAF-II cell line. **C** Boxplots of GSVA score (based on the ssGSEA method) evaluating the Basal-like and Classical signatures (Moffitt et al., 2015) upon FGFR4 knockdown. **D** Expression of classical and basal-like genes in FGFR4-deficient HPAF-II cells (compared to parental cells) from RNA-Seq data. Data are presented as mean $\pm$ SD.*$p < 0.05$; **$p < 0.01$; and ****$p < 0.0001$ by Student t test. **E** Enrichment of selected pathways (GSEA) when comparing HPAF-II proficient (NTC) and deficient (siFGFR4) cells. GSEA was performed using gene sets from Hallmark database in MsigDB library. Displayed gene sets that passed false-discovery rate < 0.05. **F**

Enrichment of Interferon related pathways when comparing FGFR4 low versus FGFR4 high tumours of the PanCuRx cohort (Chan-Seng-Yue et al., 2020). GSEA was performed using gene sets from databases in MsigDB library. Displayed gene sets that passed false-discovery rate < 0.05. G GSEA plot evaluating the Bailey_Squamous (left panel) and the Bailey_Progenitor (right panel) signatures upon FGFR4 knockdown in AsPC1 and in SUIT2 cell lines, respectively. **H** Enrichment of selected pathways (GSEA) when comparing FGFR4 high versus FGFR4 cells from the scRNA-Seq dataset of Peng et al. (Peng et al., 2019). See also Supplementary Fig. 5I. GSEA was performed using gene sets from Hallmark database in MsigDB library. **I** Expression of classical and basal-like/squamous genes in FGFR4 high cells (compared to FGFR4 low cells) displaying either a basal-like (left panel) or a classical (right panel) phenotype.

Loss of FGFR4 leads to increased fluxes through the mTORC1 pathway in PDAC cells

Next, we used Enrichr (Kuleshov et al., 2016) on gene expression data to infer signalling pathways' dysregulation that might explain the increased aggressiveness observed in PDAC cells upon depletion of FGFR4. We found the significant enrichment of gene sets related to the PI3K/AKT, ERBB, Axon guidance, and RAS signalling pathways in PDAC cells depleted for FGFR4 (**Fig. 6A**) as well as in the FGFR4^{low} tumours of both the ICGC (Bailey et al., 2016) and PanCuRx (Chan-Seng-Yue et al., 2020) cohorts (**Fig. 6B**). First, we evaluated the effect of FGFR4 downregulation on the main signaling activated through the stimulation of FGFRs, the MAPK pathway. Serum-starved HPAF-II and SUIT2 cell lines were stimulated for 20 min with FGF ligands or 2% FBS, which induced the phosphorylation of ERK in both parental and FGFR4-depleted cells (Supplementary Fig. 6A, B). This suggests that the loss of FGFR4 does not compromise signaling through this pathway. Furthermore, the baseline level of phospho-ERK were elevated in both HPAF-II and SUIT2 cell lines upon FGFR4 knockdown, which is in line with the pathway analysis from RNA-seq data. A common single nucleotide polymorphism in the exon 9 of the FGFR4 gene results in a nucleotide change (G388R), which has been shown to enhance STAT3 activation without altering MAPK/ERK pathway (Ulaganathan et al., 2015). In our cohort, 7 out of 12 PDAC models carry the variant (see material and methods section). In line with a previous report (Ulaganathan et al., 2015), the polymorphic allele does not explain differences in FGFR4 transcript levels between cell lines (data not shown). Then, we tested the effect of FGFR4 knockdown on the activation of STAT3 in cell lines either wild-type (AsPC1) or carrying the polymorphic allele (HPAF-II and SUIT2). In line with the literature (Ulaganathan et al., 2015), the depletion of FGFR4 in SUIT2 and HPAF-II cell lines reduced the baseline and stimulated activation of STAT3 (Supplementary Fig. 6C). Conversely, the downregulation of FGFR4 in AsPC1 cell line did not dramatically affected the activation of STAT3, while consistently driving increased fluxes through MAPK at baseline (Supplementary Fig. 6C). Next, we sought to validate the inferred activation of the PI3K/AKT/mTOR pathway, which resulted the most dysregulated pathway in both cell lines and tissues at transcriptomic level (Fig. 6A,

B). We assessed the baseline and stimulated activation of the PI3K/AKT/mTOR pathway through the evaluation of the phosphorylated levels of AKT and of the downstream mTORC1 effectors (the inhibitory eIF4E-binding protein 4E-BP1, and the substrate of the S6 Kinase). Cells were serum-starved and then stimulated with FGF2, FGF19, and 2% of Fetal-bovine serum (FBS). In parental HPAF-II cell line, 20 min stimulation with either FGF ligands or FBS led to activation of AKT (Ser473), to increased phosphorylation of 4E-BP1, but not to increased phosphorylation of the S6K1 substrate S6 (**Fig. 6C** and Supplementary Fig. 6D). Strikingly, loss of FGFR4 in serum-starved condition was associated to increased activation of AKT, of S6K and phosphorylation of 4E-BP1 (Fig. 6C). As compared to the parental cell line, HPAF-II lacking FGFR4 showed higher induction of phosphorylated level of AKT, but no further increase in the phosphorylation of 4E-BP1, following stimulation with either FGFs or serum (Fig. 6C and Supplementary Fig. 6D). Overall, these data suggest that loss of FGFR4 in HPAF-II cell line increases the flux through the mTORC1 pathway in particular through the inhibition of the translational repressor 4E-BP1, which is known to be required for mTORC1-dependent regulation of proliferation in mammalian cells (Dowling et al., 2010). We replicated these results in five additional cell lines (PDA2-9-23, SUIT2, and AsPC1) by showing that the loss of FGFR4 primarily increases the phosphorylation of 4E-BP1 at baseline (**Fig. 6D** and Supplementary Fig. 6E–H). In keeping with this, we found increased levels of phosphorylated 4E-BP1 in pancreatic cancer tissues from mice transplanted with HPAF-II stably expressing shFGFR4 (**Fig. 6E**). Given that mTORC1 is the master regulator of protein synthesis (Thoreen et al., 2012), we measured changes in protein synthesis following FGFR4 knockdown in four different PDAC cell lines (see methods). Loss of FGFR4 significantly increased total protein synthesis (**Fig. 6F, G**) and coherently gene expression terms related to translational initiation were significantly enriched following FGFR4 knockdown (Supplementary Fig. 6I). Finally, we reasoned that if elevation of mTORC1 pathway activity was primarily responsible for the increased proliferation of PDAC cells upon FGFR4 depletion, then pharmacological inhibition of the pathway could represent a viable strategy to reverse this phenotype. Indeed, we found that, compared to the vehicle-treated cells, the treatment with the mTORC1

inhibitor (Everolimus) resulted in a larger inhibition of cell proliferation in FGFR4 depleted cells as opposed to parental cells (**Fig. 6H**). Overall, our results indicate that loss of FGFR4 in PDAC is associated to increased mTORC1-driven cell proliferation regardless of the genetic and transcriptomic background of the cells.
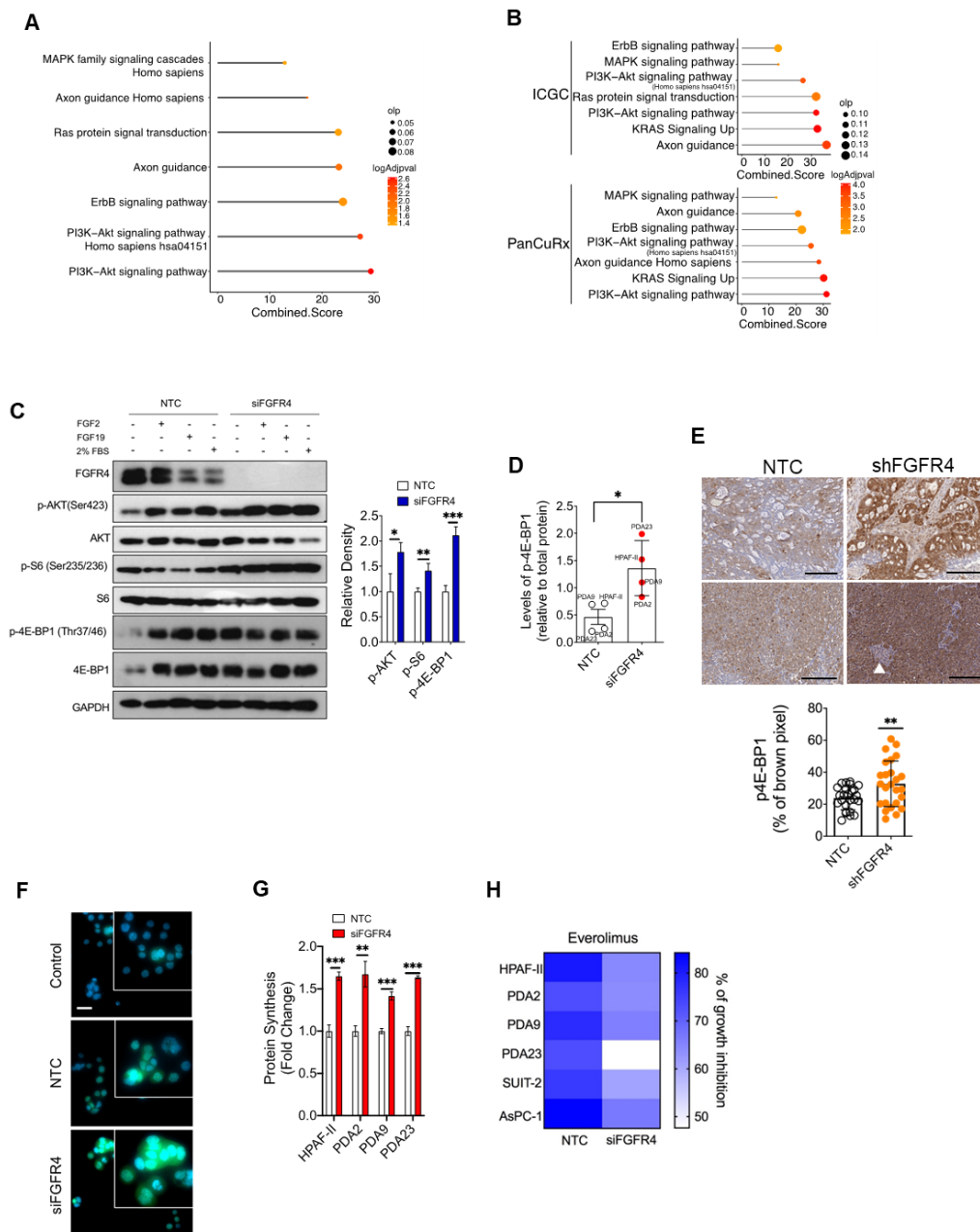
Fig. 6: Loss of FGFR4 is associated to hyperactivation of mTORC1 in PDAC. A Enrichr pathway analysis of significantly over-represented genes in FGFR4 deficient HPAF-II cells. **B** Enrichr pathway analysis of significantly over-represented genes in FGFR4low tumours of the ICGC (Bailey et al., 2016) (top) and PanCuRx (Chan-Seng-Yue et al., 2020) (bottom) cohorts. **C** Immunoblot analysis in whole-cell lysates of HPAF-II cell line transfected with either control (NTC) or siRNA targeting FGFR4. GAPDH was used as loading control. Quantification of changes in the phosphorylated levels of selected proteins (p-AKT, p-S6, and p-4E-BP1) between NTC and siFGFR4 at baseline is provided in the bar plots on the right (data presented as means ± SD of four biological replicates). *$p < 0.05$; **$p < 0.01$; ***$p < 0.001$ by Student's t test. See also Supplementary Fig. 6D. **D** Scatter plot showing changes in the phosphorylated levels of 4E-BP1 in four different cell cultures (HPAF-II, PDA2, PDA9, PDA23) following transient knockdown of FGFR4. *$p < 0.05$ by Student's t test. The quantification refers to the immunoblots of (C) and

Supplementary Fig. 6E–G. **E** Representative images of the immunohistochemical staining for phosho-4E-BP1 in tissues from mice transplanted with either mock (NTC) or shRNA targeting FGFR4. Areas with different histologies were included in the analyses. White arrowhead refers to islet of Langerhans, which stained negative and used as internal control. The quantification is provided in the scatter dot plot (bottom panel) as percentage of brown pixel (mean intensity/nuclei). A minimum of five field of visualisation (FOVs, 20X areas) per mouse (5 mice/cohort) was analysed. Scale bars, 200 μm. **F** Immunodetection of DAPI (blue), and newly synthesised protein (green) in cycloheximide-treated HPAF-II cells (top), and HPAF-II transfected with control (NTC, middle panel) and siRNA targeting FGFR4 (bottom panel). Scale bar, 20 μm. **G** Quantitative Click-iT HPG Alexa Fluor 488 immunofluorescence labeling showed a significant increase in nascent protein synthesis following the silencing of FGFR4 in different monolayer cultures. Data presented as means ± SD (n = 3 biological replicates per cell culture). **p < 0.01; and ***p < 0.001 as determined by Student's t test. **H** Cell viability of PDAC monolayer cultures transfected with either mock or siRNA targeting FGFR4 for 48 h and then challenged with 1 μM of the mTORC1 inhibitor Everolimus for 48 h (see methods). Data are displayed as heatmap of the percentage of inhibition relative to the untreated control and presented as mean of three independent experiments.

DISCUSSION

Here, we show that the loss of *FGFR4* expression in PDAC is invariably associated with the acquisition of a more aggressive phenotype by cancer cells driven by hyperactivation of the mTORC1 pathway. Conversely, we found that FGFR1 is a functional marker of the EMT. Receptor-Tyrosine Kinases (RTKs) initiated signalling is critical to cell fate determination (Lemmon et al., 2010; Neben et al., 2019). Therefore, we reasoned to explore the involvement of RTKs into the definition of PDAC subtypes which display distinct biological and clinical behaviours. The FGF-FGFR axis has been reportedly involved in pancreatic cell specification (Bhushan et al., 2001; Elghazi et al., 2002; Gonçalves et al., 2021; Hebrok et al., 1998) and, while an aberrant FGFR signalling is reported in several malignancies (Frattini et al., 2018; Turner & Grose, 2010), its involvement in PDAC has been largely neglected so far. Amplification and overexpression of *FGFR1* are described in up to 10% of patients with advanced PDAC (Aguirre et al., 2018) but rarer in resectable cohorts (Bailey et al., 2016; Cancer Genome Atlas Research Network, 2017). Expression of FGFR4 is reported in a substantial fraction of PDAC but its role in mediating tumorigenesis and therapy resistance has been seldomly explored (Sasaki et al., 2020; Motoda et al., 2011). Here, we provide multiple lines of evidence that *FGFR4* expression is restricted to epithelial cells in both normal and diseased pancreata, selectively elevated in classical tumours, and correlated with better outcomes. As opposed to *FGFR4, FGFR1* showed more promiscuous expression in both normal and diseased pancreata, was strongly associated with the EMT phenotype but not with epithelial (i.e. classical or basal-like) PDAC subtypes. Accordingly, genetic manipulation of *FGFR1* in cells displaying mesenchymal traits and classified as basal-like based on transcriptomic profiling resulted in a reduced expression of markers/drivers of EMT and of the EMT gene program but did not lead to epithelial phenotype switch. Increased FGFR1 expression could be observed in PDAC cells following prolonged exposure to TGFβ1 and coherently reduced upon transient knockdown of the master-regulator ZEB1. Activation of FGFR1 is linked to EMT in prostate cancer (Acevedo

et al., 2007), and both EMT and upregulation of FGFR1 has been linked to resistance to targeted therapies in lung cancers (Raoof et al., 2019; Kitai et al., 2016). In our study, selective inhibition of FGFR1 with BGJ398 did not dramatically affect proliferation of PDAC cells. Differently from FGFR1, we found a defined relationship between *FGFR4* expression and the classical subtype of PDAC. Loss of *FGFR4* in basal-like/squamous tumours was concordant with hypermethylation of the gene and reduced levels of active chromatin in its regulatory regions. Our results strongly suggest an epigenetic dysregulation of *FGFR4* expression in basal-like/squamous tumours which is similar to that observed for several endodermal transcription factors. We also demonstrated that *FGFR4* is a direct target of the classical transcription factor HNF1A. In line with recent reports, the silencing of *HNF1A* in the classical PDAC cell line HPAF-II was not sufficient to drive a subtype switch. In the same model, however, downregulation of *FGFR4* was sufficient to drive a full subtype switch thus suggesting that FGFR4 has stronger "antibasal" function than HNF1A in this cell line. In other two well-established models of classical/progenitor PDAC, the forced downregulation of *FGFR4* was not sufficient to drive a full switch of phenotype towards the basal-like subtype but was invariably associated with the reduced expression of classical genes and the enrichment for transcriptional programs of basal-like/squamous PDAC. This suggests that FGFR4 acts to maintain the classical phenotype and therefore to limit the expression of ectopic gene programs (i.e. basal-like/squamous) in PDAC. In keeping with that, the analysis of scRNA-Seq data demonstrated that, at individual cell level, FGFR4 expression is elevated in cells with a more classical/epithelial phenotype.

We additionally showed that *FGFR4* loss is associated with enhanced malignancy of PDAC cells by increasing *in vitro* and *in vivo* proliferation as well as enhancing metastatization of a cell line of the classical background. This finding further corroborates the evidence that basal-like cells tend to accumulate in advanced stages of the disease. While repression of "basalness/squamousness" seems an intrinsic feature of FGFR4, we also showed that its silencing in *FGFR4^{low}* basal-like models increases malignant behaviour suggesting a bona fide tumour suppressive role for endogenous levels of FGFR4 in PDAC. Others have recently

suggested that RTKs in PDAC might exert an oncogenic role only when overexpressed (Meyers et al., 2020). In keeping with this, acceleration of cell proliferation could be observed in established and primary cell lines regardless of their background and upon either transient or stable knockdown of *FGFR4*. Accordingly, gene programs related to cell cycle and proliferation were highly enriched in the comparison between low versus high *FGFR4* tumours of the ICGC and PanCuRx cohorts (Bailey et al., 2016; Chan-Seng-Yue et al., 2020). Pharmacological inhibition of FGFR4 had little to no effect on the short-term proliferation of several PDAC cell lines. Interestingly, stimulation of *FGFR4^high* classical cells with FGF2 and FGF19 led to reduced cell proliferation, which partially agrees with results from Motoda et al. (Motoda et al., 2011) that suggested a tumour suppressive role of FGF19 stimulation on cells expressing FGFR4 in PDAC. Conversely, FGF ligands did not exert inhibitor effects on the proliferation of cells deficient for FGFR4. Mechanistically, downregulation of *FGFR4* was associated with increased basal fluxes through the MAPK and the mTORC1 signaling pathways regardless of the genomic and transcriptomic background of the cells. Accordingly, PI3K/Akt/mTOR transcriptional signatures as well as the inhibitory phosphorylation of one of the best characterised mTORC1 substrate, 4E-BP1, were significantly enriched in both cell lines and tissues displaying reduced expression of FGFR4. Phosphorylation of 4E-BP1 by mTORC1 has been demonstrated to regulate mTORC1-driven proliferation in mammalian cells (Dowling et al., 2010; Thoreen et al., 2012) and accordingly its levels were higher in all cell lines tested following silencing of *FGFR4* and were concordant with increased cell proliferation and protein synthesis. In keeping with this, pharmacological inhibition of mTORC1 with Everolimus showed superior effect in reducing the proliferation of cells deficient for FGFR4 as opposed to proficient cells. In summary, we show that endogenous levels of *FGFR4* limit the malignant phenotype of PDAC. In particular, the loss of FGFR4 was associated with increased activity of the mTORC1 pathway in PDAC cells. Finally, we propose *FGFR4* as a valuable marker for the prognostic stratification of PDAC patients.

MATERIALS AND METHODS

Human samples

Pancreatic cancer tissues used in this study were obtained from surgical resections of patients treated at the University and Hospital Trust of Verona (Azienda Ospedaliera Universitaria Integrata, AOUI). Written informed consent from the donors for research use of the tissue was obtained prior to acquisition of the specimens. In particular, the FFPE tissues of 106 PDAC cases used for *in situ* hybridization and immunohistochemical analyses were retrieved from the ARC-Net Biobank and were collected under the protocol number 1885 approved by the local Ethics Committee (*Comitato Etico Azienda Ospedaliera Universitaria Integrata*) to A.S. (Prot. 52070, Prog. 1885 on 17/11/2010). Two different pathologists (A.S. and C.L.) independently performed histopathological evaluation and scoring of the tissues for *FGFR1* and *FGFR4* expression. Resected tissues used for the generation of organoids and monolayer cell cultures were collected under the protocol number 1911 approved by the local Ethics Committee (*Comitato Etico Azienda Ospedaliera Universitaria Integrata*) to V.C. (Prot. n 61413, Prog 1911 on 19/09/2018). All experiments were conducted in accordance with relevant guidelines and regulations.

Cell cultures

A total of 12 monolayer cell cultures and 5 PDAC organoids were used in this study. The established human cell lines HPAF-II, PANC1, and AsPC-1 were purchased from ATCC (CRL-1997™, CRL-1469™, CRL-1682™). Human hM1, hF2, and hT1 2D cell cultures and hT3 organoids were kindly provided by Dr. David Tuveson (Cold Spring Harbor Laboratory, NY, USA), while SUIT-2 and Hs766T were kindly provided by Prof. Aldo Scarpa (University of Verona). HPAF-II, PANC1, SUIT-2, and AsPC-1 were grown in DMEM (Gibco) supplemented with 10% FBS and 1% Penicillin-Streptomycin (Pen-Strep, Gibco). hM1, hF2, Hs766T, and hT1 were cultured in RPMI (Gibco) supplemented with 10% FBS and 1% Pen-

Strep. PDAC organoids and primary monolayer cultures were established as described previously (Boj et al., 2015; Huch et al., 2013). Briefly, tumour specimens were minced and digested with Collagenase II (5 mg/mL, Gibco) and Dispase I (1.25 mg/mL, Gibco) in human complete medium (described in Boj et al., 2015) at 37°C for a maximum of 2 hours. The resulting material was further digested with TrypLE (Gibco) for 10 minutes at 37°C, embedded in growth factor reduced Matrigel$^{(R)}$ and cultured in human complete medium. Of the models used here, 7 out of 12 carry the G388R variant of FGFR4 (HPAF-II, hF2, SUIT2, PDA23, PDA9, PANC1, and hT3).

Four of the five organoid models used were acquired as part of the Human Cancer Model Initiative (HCMI) and, those models are available for access from ATCC. The corresponding IDs are as follows:

Sample Code	ID
PDA1-O	HCM-CSHL-0080-C25
PDA2-O	HCM-CSHL-0077-C25
PDA9-O	HCM-CSHL-0081-C25
PDA20-O	HCM-CSHL-0092-C25

Tissue digestion from 4 specimens was also directly seeded on tissue-culture vessels for initiation of monolayer cell cultures using the following medium: Advanced DMEM/F12 medium (Gibco) supplemented with HEPES (1X, Gibco), Glutamax^{TM} (1X, Gibco), Primocin^{TM} (1 mg/mL, Invivogen), mouse Epidermal Growth Factor (50 ng/mL, Gibco), Dexamethasone (3 nM, Sigma), and 5% Fetal Bovine Serum (FBS, Gibco). Both monolayer cell cultures and organoids were routinely tested for the presence of mycoplasma using MycoAlert Detection Kit from Lonza, in accordance with the manufacturer's instructions.

Lentiviral infection of cell lines and organoids

Stable knockdown of *FGFR1* and *FGFR4* was achieved using validated short hairpin RNAs (shRNA) against human *FGFR1* (TRC clone 574) and human *FGFR4* (TRC clone 884, 885, and 419) in the vector pLKO.1-puro-CMV-tGFP (Sigma-Aldrich). The vector TRC2 pLKO.5-puro (Sigma-Aldrich) was used as non-targeting control (NTC) of the infection. Lentiviruses were produced in HEK293T cells by transfecting plasmids (containing the GFP cassette) and the packaging plasmid VSV-G with X-tremeGENE9 (Roche, 063665110101). The viral supernatants were harvested at 48 hours and cell debris removed prior to infection. To concentrate lentivirus, Lenti-X concentrator (TaKaRa Bio) was used. Transduction of monolayer cell cultures was performed by adding the viral supernatants supplemented with 1 µg/mL of Polybrene (Santa Cruz Biotechnology) to cells having 50-60% of confluency. Two days after infection, 2 µg/mL of puromycin (Gibco) was added for antibiotic selection. For transduction of organoids, cultures were first released from Matrigel$^{(R)}$ by incubation with a solution of Dispase I at 37°C for 20 minutes, and then subjected to enzymatic digestion with TripLE (Gibco) supplemented with Dispase I and 0.1 mg/mL DNAse I (Sigma-Aldrich) for 20 minutes. 1×10^{5} single cells were resuspended with the transduction medium supplemented with 1 µg/mL of polybrene, spinoculated at 600 x g for 1 hour at room temperature, and incubated for 16 hours at 37°C. The following day, cell suspension was recovered and seeded in Matrigel$^{(R)}$. Two days after infection, cells were treated with 2 µg/mL puromycin (Gibco) for antibiotic selection. Successful transduction was assessed by visualizing GFP positivity of cells with the EVOS Cell Imaging System (Thermo Fisher Scientific), and antibiotic selection stopped when the treatment caused extinction of the untransduced cultures. The sequences of shRNAs against *FGFR1* and *FGFR4* are as follows:

Target location	Clone ID	DNA Sequence
3UTR	TRCN0000199419	CCTGACACAGTGCTCGACCTT
CDS	TRCN0000219885	TGTGGGCAGCATCCGCTATAA
CDS	TRCN0000219884	CCCTCGAATAGGCACAGTTAC
CDS	TRCN0000312574	TGCCACCTGGAGCATCATAAT

For *in vitro* drop-out experiments with organoids, the viral supernatants were adjusted to achieve an 80% of GFP+ ratio. As control, organoids were transduced with pre-made GFP expressing lentiviral particles (CMV-neo, Amsbio).

Animal Studies

Six- to Eight-weeks old *NSG* (NOD.Cg-Prkdc^{scid};Il2rg^{tm1Wjl}) mice were purchased from Charles River Laboratory (Milan). All animal experiments regarding transplanted mice were conducted in accordance with procedures approved by CIRSAL at University of Verona (approved project 655/2017-PR). No statistical methods were used to predetermine sample size estimate for transplantation experiments, which was instead based on preliminary experiments showing an engraftment rate above 95% for both cell lines and organoids. Therefore, a minimum of 5 successful grafts (per group) was considered suitable to consistently identify differences between groups in terms of tumour growth. For orthotopic transplantation of either cell lines ($1x10^6$ cells) or dissociated organoids ($1x10^6$ cells), mice were anesthetized using isoflurane and an incision was made in the left abdominal side at the level of the spleen. Cells were resuspended in 50 µl of a 2:3 dilution of Matrigel$^{(R)}$ (Corning) and cold PBS (Gibco) and injected into the tail region of the pancreas using insulin syringes (BD micro-fine 30 Gauge). The injection was considered successful by the development of bubble without signs of leakage. Mice with signs of leakage upon injection were excluded from the studies. The abdominal wall was sutured with absorbable vicryl sutures (Vetsuture), and the skin was closed with wound clips (CellPoint Scientific Inc.). Monitoring of tumour growth was performed as previously described (Olive et al., 2009). Briefly, following weekly manual palpation starting 10 days following transplantation,

tumour-bearing mice were subjected to high-contrast ultrasound screening using the Vevo 2100 System with a MS250, 13–24 MHz scanhead (Visual Sonics). Mice were sacrificed at the indicated time points (4-5 weeks, once the tumour masses have reached the 10 mm in diameter). Pancreas, spleen, lungs and liver were collected for downstream analysis.

Transient Knockdown in Cell lines

For small interfering RNA (siRNA) knockdown experiments, siRNA constructs were purchased from Thermofisher Scientific (s5176, s229971, s13869, s5164) and primary cell cultures or established cell lines were transfected with either 25 or 50 pmol of siRNA using Lipofectamine^{TM} 2000 (Thermofisher Scientific, #11668027) according to manufacturer's instruction for 6-well plates format. The sense strand of the duplex siRNAs was: *FGFR4*, 5' CAUUGACUACUAUAAGAAAtt 3'; *ZEB1*, 5'GGUAGAUGGUAAUGUAAUATT 3'; *HNF1A*, 5' AGACUAUGCUCAUCACCGATT 3'; and *FGFR1*, 5' GAGGCUACAAGGUCCGUUAtt 3'. Non-targeting siRNA (Ambion) was used as negative control at a final concentration of 25 pmol.

Cell Proliferation Assay

For measuring cell proliferation, $2x10^3$ cells were plated on white 96-well plate (Thermofisher Scientific) and cultured in 100 μL of culture medium. Cell viability was measured 72 hours post-seeding using the CellTiter-Glo assay (Promega, G9683).

Fluorescent activated cell sorting

Fluorescent activated cell sorting (FACS) analysis was performed in order to evaluate the percentage of GFP positive cells. Before the analysis, organoids were first released from Matrigel$^{(R)}$ by incubation with a solution of Dispase I at 37 °C for 20 minutes, and then subjected to enzymatic digestion with TripLE

supplemented with Dispase I and 0.1 mg/mL DNAse I (Sigma-Aldrich) for 20 minutes, until the organoids appeared as single cells under the microscope. Cells were filtrated (Cell Strainer 40μm Nylon, BD Falcon), resuspended in cold PBS and acquired using FACS Canto II (BD Biosciences). Data were analysed using FlowJo software (Flowjo LLc). Untransduced and GFP-stably expressing cells were used as negative and positive controls, respectively.

Nascent protein detection

To visualize nascent proteins, the Click-iT Protein Synthesis Assay Kit reagents (Invitrogen) was used. Cells were plated on black 96-well plates (Thermofisher Scientific) and cultured for 24 hours in DMEM methionine-free (Gibco) medium supplemented with 1X HEPES and 1X Glutamax. Cells were transfected with siRNA as previously described. Two days post-transfection, cells were incubated with the methionine analog L-homopropargylglycine (HPG) for 30 minutes at final concentration of 50 μM in methionine-free medium under conditions optimal for the cells (humidified atmosphere at 37°C and 5% CO2). After washing with cold PBS, cells were fixed with 3.7% formaldehyde (Sigma-Aldrich) for 15 minutes at room temperature, followed by a permeabilization step using 0.5% Triton X-100 (Sigma-Aldrich). The Click-iT reaction, with Alexa-488 detection reagents, was performed according to the manufacturer's protocol. For the control experiment and to confirm the specificity of the signal, 300 μg/mL cycloheximide (Sigma-Aldrich), a protein synthesis inhibitor, was added 30 minutes before HPG addition. After the Click-iT reaction, cell plates were scan using VICTOR 3 1420 multilabel counter plate reader (PerkinElmer) to assess nascent protein synthesis by determining signal intensity in the fluorescent channel of FITC. Two dimensional cultures were also imaged using Axio Observed Z1/7 inverted Wide field microscope (Zeiss) with 40x objective magnification and digitalized by the Zeiss Zen software.

Therapeutic experiments with cell cultures

BGJ398 (S2183, Selleckchem), BLU3391 (S7819, Selleckchem), and Everolimus (S1120, Selleckchem) were dissolved in DMSO (Sigma-Aldrich). The final concentration of DMSO was no higher than 0.2%. Briefly, cells were dissociated to single cells by enzymatic dissociation with 1X Trypsin (Gibco) at 37°C for 2 minutes, counted and seeded in a range concentration of $1x10^3 – 2.5x10^3$ cells into individual wells of a white 96-well plate. After 24 hours, cells were treated with appropriate drugs for 48 hours using drug concentrations ranging from 0.1 nM to 10 µM. Proliferation was measured using CellTiter-Glo assay per the manufacturer's protocol. For treatment with Everolimus, cells were counted and diluted to obtain 20 cells/µL in 100 µL of Opti-MEM^{TM} supplemented with 5% FBS. 100 µL of cells-containing medium was plated into individual wells of a white 96-well plate. Twenty-four hours after culture, cells were transfected with siRNA against FGFR4 and non-targeting small interfering RNA control, as previously described. The concentration of Everolimus necessary to achieve inhibition of activity by 50% (IC$_{50}$) was calculated using concentrations ranging from 0.1 nM to 10 µM (7-point curve). 1 µM of drug was added in 100 µL of culture medium 48 hours post-plating, with nine replicate wells for each sample. At day 5, cell viability was measured using a luminescence ATP-based assay (CellTiter-Glo). Cells were also treated with 5 ng/mL of human TGFβ1 (#100-21, Peprotech), alone or in combination with 500 nM of A83-01 (#2939, Tocris Bioscience), 25 ng/mL of Recombinant Human FGF-basic (#100-18C, Peprotech), 100 ng/mL of Recombinant Human FGF10 (#100-26, Peprotech), 100 ng/mL of Recombinant Human FGF19 (#100-32, Peprotech), and 2% of Fetal Bovine Serum (FBS, Gibco).

Histology and Immunohistochemistry

Tissues were fixed in 10% neutral buffered formalin and embedded in paraffin. Sections were subjected to Hematoxylin and Eosin as well as immunohistochemical staining. The following primary antibody was used for immunohistochemical staining of xenografts: Phospho-4E-BP1 (Thr37/46) (#2855, Cell Signaling), 1:400. Slides were scanned at 40x magnification and digitalized using the Aperio Scan-

Scope XT Slide Scanner (Aperio Technologies). Quantification of p-4E-BP1 staining was performed in at least five random nonoverlapping fields of visualization (magnification, 20x) in each sample using ImageJ. To measure the percentage of positive area, captured images were first color deconvoluted and DAB+ particles counted automatically. The percentage of strong positive pixels was calculated relative to the number of nuclei present in each of the selected areas. Positivity for p-4E-BP1 was rarely seen in non-neoplastic cells.

Immunofluorescence

Cells (5 x 10^3 cells per chamber) were seeded into chamber culture slides (BD Falcon) in culture media. The next day, cells were rinsed with ice-cold PBS and fixed with 3.7% formaldehyde for 10 minutes at room temperature followed by permeabilization with 0.5% Triton X-100. The cells were subjected to immunofluorescence staining with the following primary antibodies: PDX1 (#EPR3358, ab134150, Abcam), 1:100; and Cytokeratin 5 (CK5) (NCL-L-CK5, Leica Biosystems), 1:100. All antibodies were incubated for 2 hours at room temperature. The cells were then washed with cold PBS three times for 3 minutes and incubated with Alexa 488-labeled anti-rabbit secondary antibody (1:500) (Invitrogen), and Alexa 555-labeled anti-mouse secondary antibody (1:500) (Invitrogen) at room temperature for 1 hour. A final step of washes in cold PBS was completed at room temperature followed by mounting with DAPI (Vector Laboratories). The cells were examined by Olympus BX61 Upright fluorescence microscope (Leica).

In Situ Hybridization

The *in-situ* hybridization (ISH) was performed on 4 μm section of human PDAC tissues (n = 106) and on xenografts. Briefly, sections were deparaffinized by incubation with xylene for 10 minutes, 100% ethanol for 2 minutes and then let dry for 5 minutes at room temperature. Slides were incubated for 10 minutes with RNAscope® Hydrogen Peroxide (Advanced Cell Diagnostics), washed with

distilled water and incubated for 20 minutes at 99°C with RNAscope® 1X Retrieval Reagents (Advanced Cell Diagnostics). Sections were rinsed in distilled water and dehydrated in 100% ethanol for 3 minutes and let dry at room temperature. Then, the slides were incubated at 40°C for 10 minutes with RNAscope® Protease Plus (Advanced Cell Diagnostics), washed with distilled water and incubated with the appropriate probe for 2 hours at 40°C, followed by washes with RNAscope® 1X Wash Buffer (Advanced Cell Diagnostic). The different RNAscope® 2.5 HD AMPs (Hs-FGFR1-C2 and Hs-FGFR4-no-XMm-C1, Advanced Cell Diagnostics) were added to the slides following manufacturer's instructions. Positive control probe Hs-UBC and 2-plex negative control probe (Advanced Cell Diagnostics) were used as positive and negative control, respectively. Then, slides were incubated for 10 minutes at room temperature with either ImmPACT™ DAB Substrate Kit (DBA) or RNAscope® 2.5 HD Detection Reagent- RED (Advanced Cell Diagnostic). Slides were stained with hematoxylin, dried at 60°C for 15 minutes and mounted with VectaMount® mounting medium (Vector Laboratories). Slides were scanned at 40x magnification and digitalized using the Aperio Scan-Scope XT Slide Scanner. For each case, two consecutive tissue sections were prepared and stained for *FGFR1* and *FGFR4*. Only RNA signals from neoplastic cells were evaluated in a minimum of 5 field of investigations (at 20X magnification). The following semiquantitative method was used for scoring: score 0, no or rare signals (dots); score 1, between 3 and 10 dots per cell at 20X magnification; score 2, more than 10 dots (or clusters) per cell. For each marker, cases were considered high if showing an average score > 1.5, and low if showing a score of < 1.5. A total of 97 cases were suitable for evaluation of the mRNA expression of both *FGFR1* and *FGFR4*; of those 76 had available overall survival data for correlation analyses.

Immunobloting

Protein lysates were prepared using Cell Signaling Lysis Buffer (Cell Signaling) and separated on 4-12% Bis-Tris NuPAGE gels (Life Technologies), transferred onto a PVDF membrane (Millipore) and incubated with the following antibodies:

FGFR4 (8562, Cell Signalling), FGFR1 (9740, Cell Signalling), Akt (9272, Cell Signalling), phospho-Akt (4060, Cell Signalling), phospho-S6 Ribosomal protein (4858, Cell Signalling), S6 Ribosomal protein (2217 ,Cell Signalling), phospho-4E-BP1 (2855, Cell Signalling), 4E-BP1 (9644, Cell Signalling), ERK1/2 (9102, Cell Signalling), phospho-ERK1/2 (4376, Cell Signalling), phospho-FRS2 (2864, Cell Signalling), STAT3 (12640, Cell Signalling), phospho-STAT3 (Tyr705, 9145 Cell Signalling), Vimentin (NCL-L-VIM-V9, Leica Biosystems), HER3/ErbB3 (12708, Cell Signalling), ZEB1 (203829, Abcam), HNF1A (sc-393925, Santa Cruz Biotechnology), E-Cadherin (M3612, Dako), RAS (F234, Santa Cruz Biotechnology). Vinculin (4650, Cell Signalling), GADPH (5174, Cell Signalling) (sc-166545, Santa Cruz Biotechnology), β-Actin (4967, Cell Signalling) were used as loading control. The immunoblots were visualized with ECL plus (Amersham/GE Healthcare Europe GmgH).

qRT-PCR analysis

RNA was extracted with Trizol® Reagent (Life Technologies) method. 1 µg of DNase-treated RNA was reverse transcribed using TaqMan® Reverse Transcription reagents (Applied Biosystems) in a volume of 20 µL according to the manufacturer's instructions. Samples were diluted to a final concentration of 10 ng/µL. TaqMan was performed in triplicate using 20 ng of cDNA and the following TaqMan® probe (TaqMan® Gene Expression Assay): *FGFR4* (Hs01106908_m1), *FGFR1* (Hs00915142_m1), *ZEB1* (Hs00232783_m1), *SNAI1* (Hs00195591_m1), *CDH1* (Hs01023894_m1), *TWIST1* (Hs01675818_s1), *KRAS* (Hs00364284_g1), and *HNF1A* (Hs00167041_m1). *HPRT1* (Hs02800695_m1) was used as reference gene. Relative gene expression quantification was performed using the ΔΔCt method with the Sequence Detection Systems Software, Version 1.9.1 (Applied Biosystems).

RNA sequencing

RNA was extracted from PDAC monolayer cultures and organoids using TRIzol (Life Technologies), followed by column-based purification with the PureLink RNA Mini Kit (Ambion). The quality of purified RNA samples was determined using a Bioanalyzer 2100 (Agilent) with an RNA 6000 Nano Kit. RNAs with RNA Integrity Number (RIN) values greater than 8 were used to generate sequencing libraries using the TruSeq sample Prep Kit V2 (Illumina) according to the manufacturer's instructions. RNA-Seq libraries prepared from organoids (n = 5) and primary cell cultures (n = 3) were multiplexed and sequenced using a NextSeq 500 platform with paired-end reads of 150 bases with a final coverage of 30 million reads per sample. RNA-Seq libraries prepared from established cell cultures (n = 20) were multiplexed and sequences using a NextSeq 500 platform with paired-end reads of 75 bases with a coverage of 3 million reads per sample. After quality control and adaptor trimming, RNA-seq reads were aligned to the GRCh38 genome build using Salmon v1.4.0 (Patro et al., 2017). Then, transcripts quantification was imported in R through tximport package v4.0 (Soneson et al., 2015). Finally, count data was normalized using the R/Biocondutor package DESeq2 v1.30.0 (Love et al., 2014) in order to produce an integrated matrix of expression values. This matrix was used for all downstream analyses. Differentially expression analysis has been performed using DESeq2 (Love et al., 2014). Gene set enrichment analysis (GSEA) was performed with *fgsea* R package v1.16.0 (Subramanian et al., 2015) and *enrichR* package v3.0 (Kuleshov et al., 2016) using the list of differentially expressed genes sorted by log2 of fold change. Pathways are from the MSigDB database and in particular Gene Ontology, KEGG, Biocarta, Reactome and Hallmark gene sets. *fgsea* function was used with default parameters. Results were considered significant for FDR < 0.05. GSVA R package v1.38.2 (Hänzelmann et al., 2013) was used to calculate the main PDAC transcriptomics subtypes (Bailey et al., 2016; Moffitt et al. 2015) gene set scores. *Gsva* function was used with ssgsea and gene set scores were compared among knockdown and control samples with Wilcoxon rank-sum test.

Single-cell RNA-Sequencing

For the integration of scRNA-seq datasets from PDAC tissues, we used the Harmony algorithm (Korsunsky et al., 2019) via the *R* package *harmony* in order to account for the technical differences of the four datasets. The datasets (Peng et al. 2019 (primary PDAC = 24, ncells = 41964), Lin et al. 2020 (primary PDAC = 10, ncells = 7752), Chan-Seng-Yue et al. 2020 (primary PDAC = 13, ncells = 33970) and Steele et al. 2020 (primary PDAC = 16, ncells = 42844)) were first preprocessed individually using Seurat (Hao et al., 2021) for quality control and filtering (percent_mt_max = 20, nFeature_min = 500, nCount_min = 500, nCount_max = 50000) and then integrated using *harmony* function with default parameters and grouping by dataset variable. Cells were annotated with *singleR* package using the preloaded dataset *HPCA* from the *celldex* package (Aran et al., 2019) to stratify gene expression by cell population. For the normal pancreas scRNA-seq datasets, we used the integration pipeline implemented in the Seurat *R* package (Stuart et al., 2019) with default parameters. The three dataset Muraro et al., 2016 (ncells=2285), Segerstolpe et al., 2016 (cells = 2394) and Grün et al., 2016 (ncells = 1004) were downloaded from the Seurat V3 repository together with their annotation metadata. The preprocessing of the datasets counts data is described in Stuart et al., 2019; the downloaded datasets set were imported and managed through the *R* package Seurat V4.0.1 (Hao et al., 2021).

Statistical Analysis and Data mining

For data mining and pancreatic cancer subtypes stratifications we used different gene expression datasets. The two main datasets were the PACA-AU cohort of the ICGC consortium and the TCGA-PAAD cohort of the TCGA consortium. The first was downloaded from the supplementary material of the corresponding publication (Bailey et al., 2016). This dataset contains normalized expression values (TMM normalized using edgeR Bioconductor package, converted to CPM and log2 transformed) of 96 pancreatic cancer patients. For subtypes stratification, Z-scores were calculated for each gene. Associated clinical data were downloaded from https://dcc.icgc.org/releases/current/Projects/PACA-AU. The second dataset

represents the TCGA-PAAD cohort (Cancer Genome Atlas Research Network, 2017), downloaded from http://firebrowse.org/?cohort=PAAD, which consists of the RNA-Seq gene expression profile of 178 pancreatic cancer patients. According to other publications that disputed the histologies of some samples, we restricted the samples' number to 148. Additional datasets included: PanCuRx (Chan-Seng-Yue et al., 2020) (EGA archive accession), Moffitt et al. (Moffitt et al., 2015) (GEO accession: GSE71729), and Cancer Cell line Encyclopedia (CCLE) (Barretina et al., 2012). PanCuRx dataset was preprocessed with STAR v2.7.6a (Dobin et al., 2013) and RSEM v1.3.1 (Li et al., 2011) and eventually a vst expression matrix was produced. For Moffitt dataset, we downloaded the matrix of log2-transformed background-corrected Cy5 microarray signal, whereas for CCLE cohort we downloaded the TPM matrix. For harmonization, Z-scores standardization was independently performed for each dataset before subsequent analysis. Expression of *FGFR1* and *FGFR4* were stratified according to tumour stage, subtype classification and survival status. The correlation of FGFR1 and FGFR4 expression with other genes was evaluated using Spearman's correlation test (significant p-value < 0.001). To classify tumours from the PanCuRx and the ICGC datasets according to the expression of *FGFR1*, *FGFR4*, and GATA6, the distribution of their transcripts levels in the respective cohorts was assessed. We observed a bimodal and a normal distribution in the PanCuRx and in the ICGC, respectively. Samples from Bailey et al. were therefore stratified according to the median value of *FGFR1, FGFR4,* and *GATA6* expression. In the PanCuRx dataset, the following thresholds were used for *FGFR1 FGFR4*, and *GATA6*, respectively: < 3.3, < 3.4, and 3.5 vst. Survival analysis has been performed through the R packages survival v3.2.10 and the graphical representation done with survminer v0.4.9 (https://CRAN.R-project.org/package=survival). We integrated the levels of *FGFR4* and *FGFR1* expression with follow-up information for patients and drew Kaplan-Meyer curves for survival stratifying the results according to mean, median, 1st and 3rd quartiles. GraphPad Prism was used for graphical representation of data. Unless indicated, all the p-values refer to Student t test.
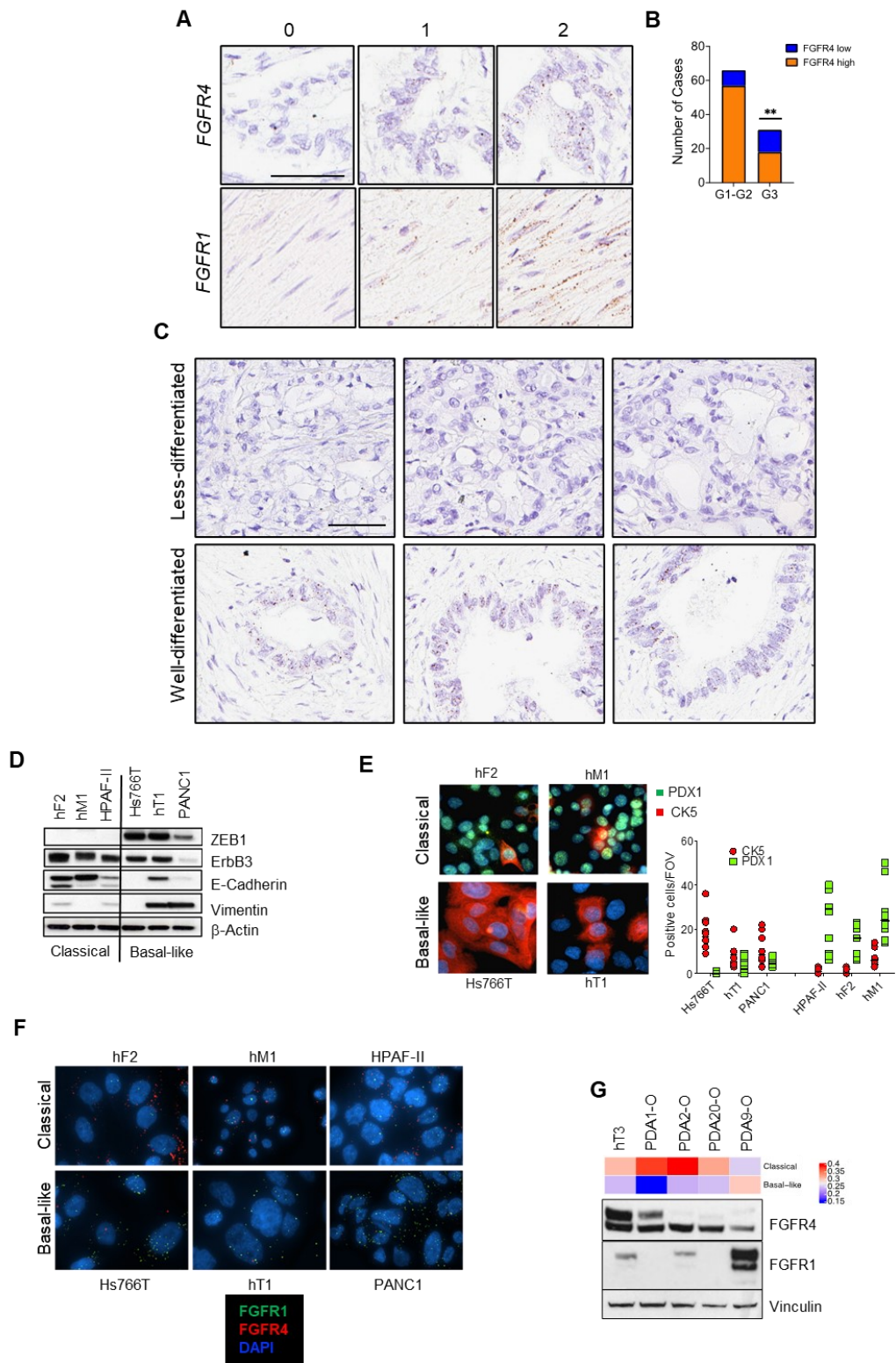
ChIP-Seq and DNA Methylation datasets

We analyzed ChIP-seq data from two different datasets: Kalisz et al. (Kalisz et al., 2020), which included H3K27ac, H3K27me3, and HNF1A ChIP-seq for mouse pancreatic cells proficient and deficient for HNF1A and all integrated with expression data; Diaferia et al. (Diaferia et al., 2016) which included H3K27ac, H3K4me1, H3K4me3, and H3K9me9 ChIP-Seq data and corresponding RNA-seq data for low grade and high grade PDAC cells. In both cases, data were preprocessed as described in the referenced papers with the only difference that Diaferia et al. dataset was re-aligned to GRCh38 human genome build. DNA methylation data were retrieved from Nones et al. (Nones et al., 2014) The methylation score for *FGFR4* was eventually compared to expression data and stratified according to the Bailey et al. (Bailey et al., 2016) subtype classification.
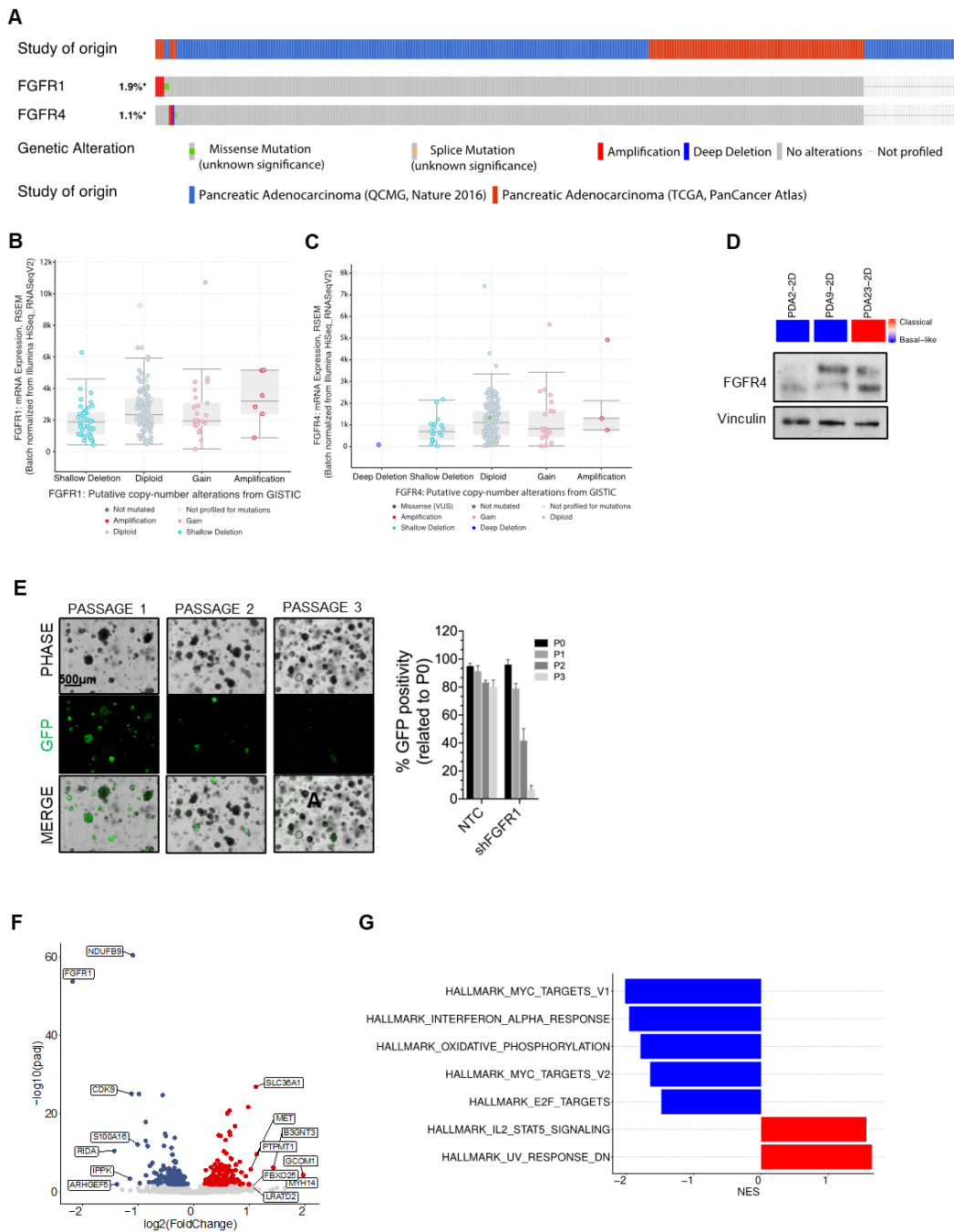
SUPPLEMENTARY FIGURES
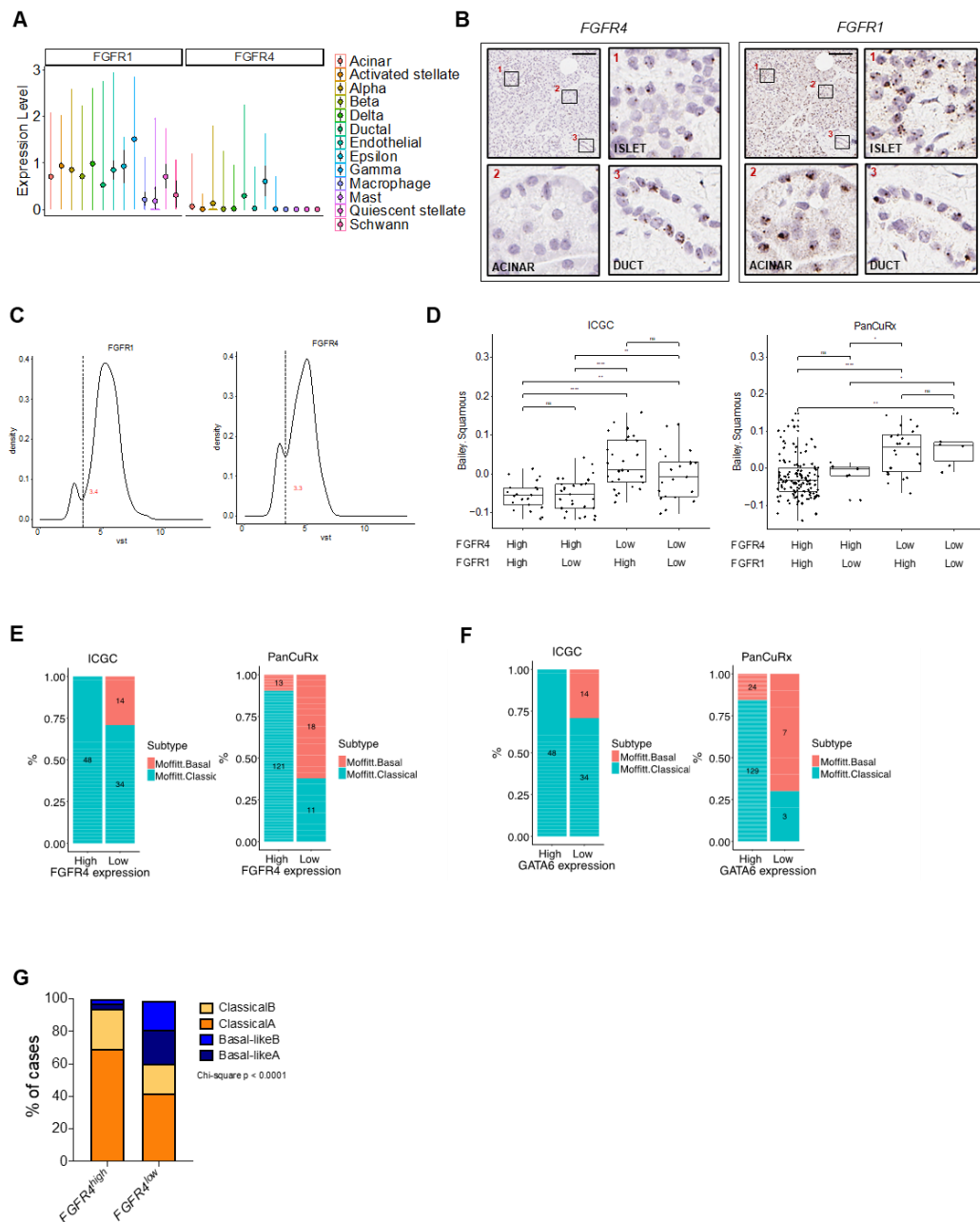
Supplementary Figure 1: Expression of FGFR4 and FGFR1 in pancreatic samples A Violin plots of the normalized expression of *FGFR4* (left panel) and *FGFR1* (right panel) in each annotated cell cluster from the scRNA-seq of normal adult pancreas from 3 different datasets (Muraro et al., 2016; Grun et al., 2016; Segerstolpe et al., 2016). **B** Representative ISH images showing expression of *FGFR4* and *FGFR1* in normal pancreas. Scale Bar, 100 μm. Insets show magnification of selected areas: 1, islet of Langerhans; 2, acinar cells; and 3, ductal cells. **C** Density plot showing the distribution the *FGFR4* and *FGFR1* mRNA expression levels in the PanCuRx cohort (Chan-Seng-Yue et al., 2020). The dashed vertical

lines refer to the value of mRNA levels (vst) that has been used as threshold to define low-versus high-expressing samples. **D** GSVA score (using ssgsea method) for the squamous signature (Moffitt et al., 2015) for each sample of the PanCuRx cohort (Chan-Seng-Yue et al., 2020) according to the expression of *FGFR1* and *FGFR4*. *, $p < 0.05$; **, $p < 0.01$; ****, $p < 0.0001$; and ns, not significant as determined by Wilcoxon test. **E** Stacked bar plot showing the Moffitt molecular subtypes distribution according to the *FGFR4* expression status in the ICGC (left) and the PanCuRx cohorts (right). **F** Stacked bar plot showing the Moffitt molecular subtypes distribution according to the GATA6 expression status in the ICGC (left) (Bailey et al., 2016) and PanCuRx (right) (Chan-Seng-Yue et al., 2020. cohorts. **G** Stacked bar plot showing the molecular subtypes distribution according to the *FGFR4* expression status in the PanCuRx cohorts.

A

FGFR4

0   1   2

FGFR1

B

FGFR4 low
FGFR4 high

Number of Cases

G1-G2   G3

**

C

Less-differentiated

Well-differentiated

D

hF2 hM1 HPAF-II Hs766T hT1 PANC1

ZEB1
ErbB3
E-Cadherin
Vimentin
β-Actin

Classical   Basal-like

E

hF2   hM1

Classical

PDX1
CK5

Basal-like

Hs766T   hT1

CK5
PDX1

Positive cells/FOV

Hs766T hT1 PANC1 HPAF-II hF2 hM1

F

hF2   hM1   HPAF-II

Classical

Basal-like

Hs766T   hT1   PANC1

FGFR1
FGFR4
DAPI

G

hT3 PDA1-O PDA2-O PDA20-O PDA9-O

Classical
Basal-like

0.4
0.35
0.3
0.25
0.2
0.15

FGFR4
FGFR1
Vinculin

Supplementary Figure 2: Expression of *FGFR4* and *FGFR1* in tissues and *in vitro* models of PDAC. **A** Representative ISH images of PDAC tissues showing no (0), moderate (1) or high (2) expression of *FGFR4* or *FGFR1*. Scale bars, 60 μm. **B** Stacked bar plot showing the distribution of morphological grades according to the *FGFR4* expression status in the PDAC tissue cohort. **, $p < 0.01$ by two-sided Chi-square test. **C** Representative ISH images of PDAC tissues showing either poor (top) or well (bottom) differentiation; scale bar, 60 μm. **D** Immunoblot analysis for ZEB1, ErbB3, E-Cadherin, and Vimentin in whole-cell lysates of 6 PDAC cell cultures. β-Actin was used as loading control. **E** Representative immunofluorescence staining of PDX1 (green) and CK5 (red) in four PDAC cell lines. Counterstain, DAPI (blue); magnification 100x. Quantification of PDX1+ cells and CK5+ cells in four PDAC cell lines is provided in the right panel as number of positive cells in a minimum of 5 field of visualization (FOV) per cell line. **F** Representative fluorescence *in situ* hybridization of *FGFR4* and *FGFR1* in 6 PDAC cell cultures. DAPI, blue; *FGFR1*, green; *FGFR4*, red. **G** Immunoblot analysis of FGFR1 and FGFR4 in whole-cell lysates of 5 PDAC organoid cultures. Vinculin was used as loading control. The classical and the basal-like signature scores were calculated for each PDAC organoid cultures using GSVA (ssgsea method).
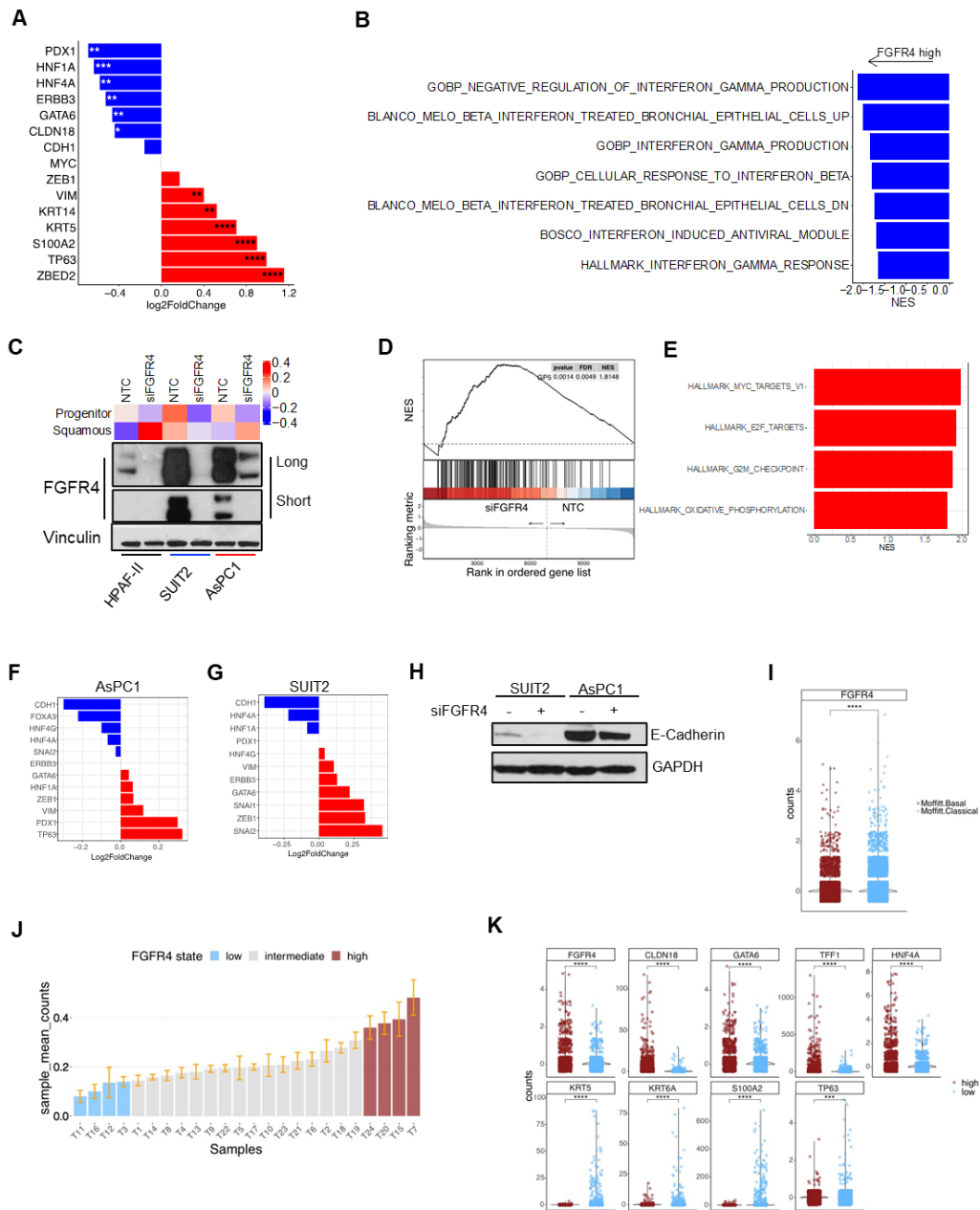
Supplementary Figure 3: FGFR1 is associated with the EMT phenotype in PDAC. A cBioportal oncoprint visualization of genetic alterations (single-nucleotide variations, copy-number variations, and structural variations) in samples from the ICGC (Bailey et al., 2016) and TCGA (Cancer Genome Atlas Research Network, 2017) cohorts. **B-C** cBioportal Boxplot visualization of the correlation between *FGFR1* (B) and *FGFR4* (C) mRNA and copy-number status for samples of the ICGC (Bailey et al., 2016) and TCGA (Cancer Genome Atlas Research Network, 2017) cohorts. **D** Classification of primary PDAC cell cultures based on RNA-Seq. At the bottom, immunoblot of whole-cell lysates showing different levels of FGFR4. Vinculin, loading control. **E** Competition based-assay

in PD9-O following infection with the shRNA targeting FGFR1. Representative phase-contrast images (top), GFP signal (green, middle panel) and merged images (bottom panel) demonstrating loss of GFP positivity over time. Scale bar as indicated. At the bottom, quantification of the GFP positivity (as percentage of signal compared to P0) over time of PDA9-0 transduced with the indicated vector linked to GFP. Data presented as mean + SEM (n = 3). **(F)** Volcano plot of differences in gene expression between control (n = 3) and *FGFR1* knocked down (KD) cells (n = 3). Indicated are some of the genes with $\log_2$FC expression ≥ 2 and adjusted $p < 0.05$. **(G)** Enrichment of pathways in Hs766T following *FGFR1* knock-down. The GSEA analysis was performed using gene sets from HALLMARK database in MsigDB library. Displayed are gene sets that passed FDR < 0.05.
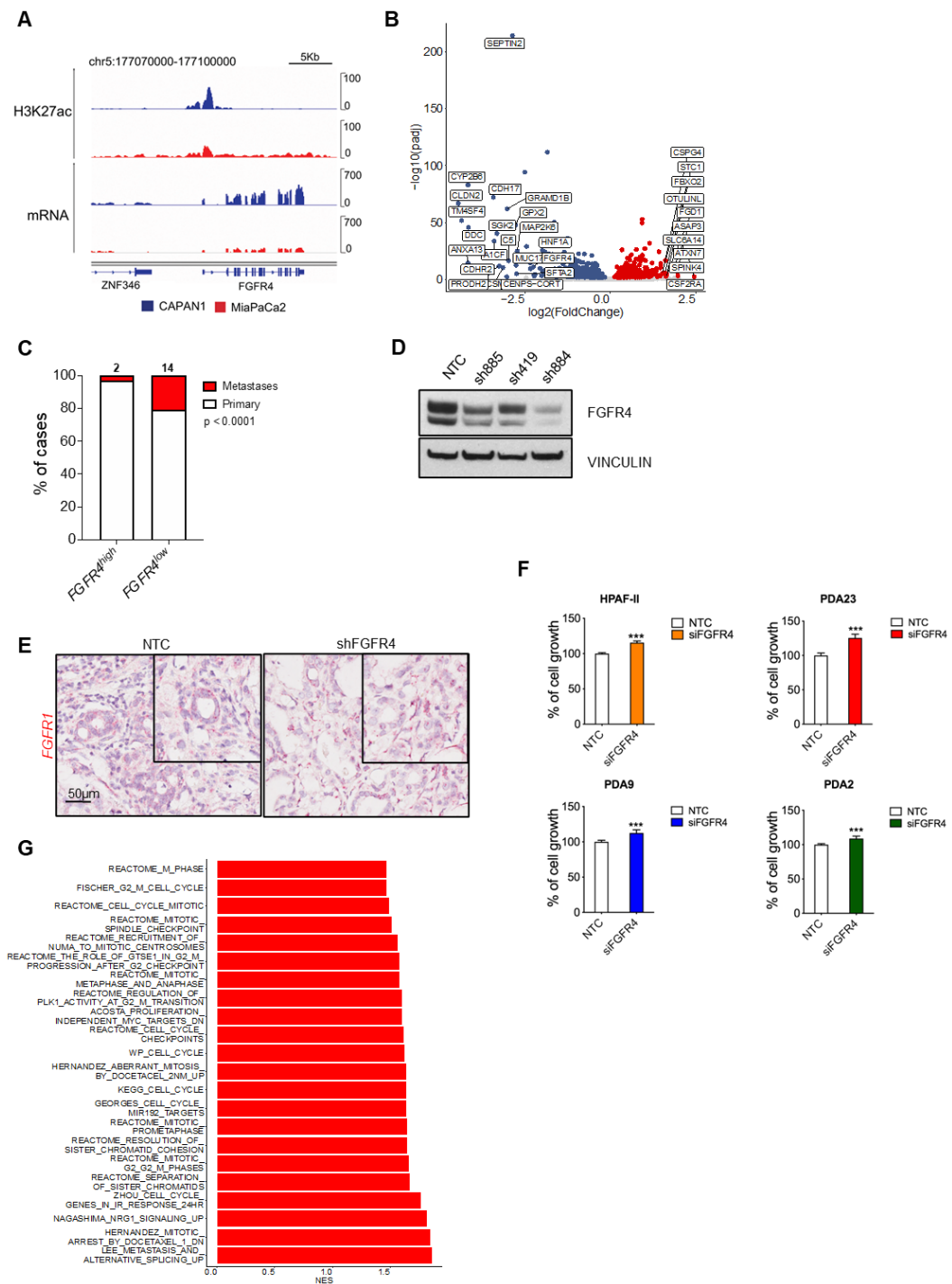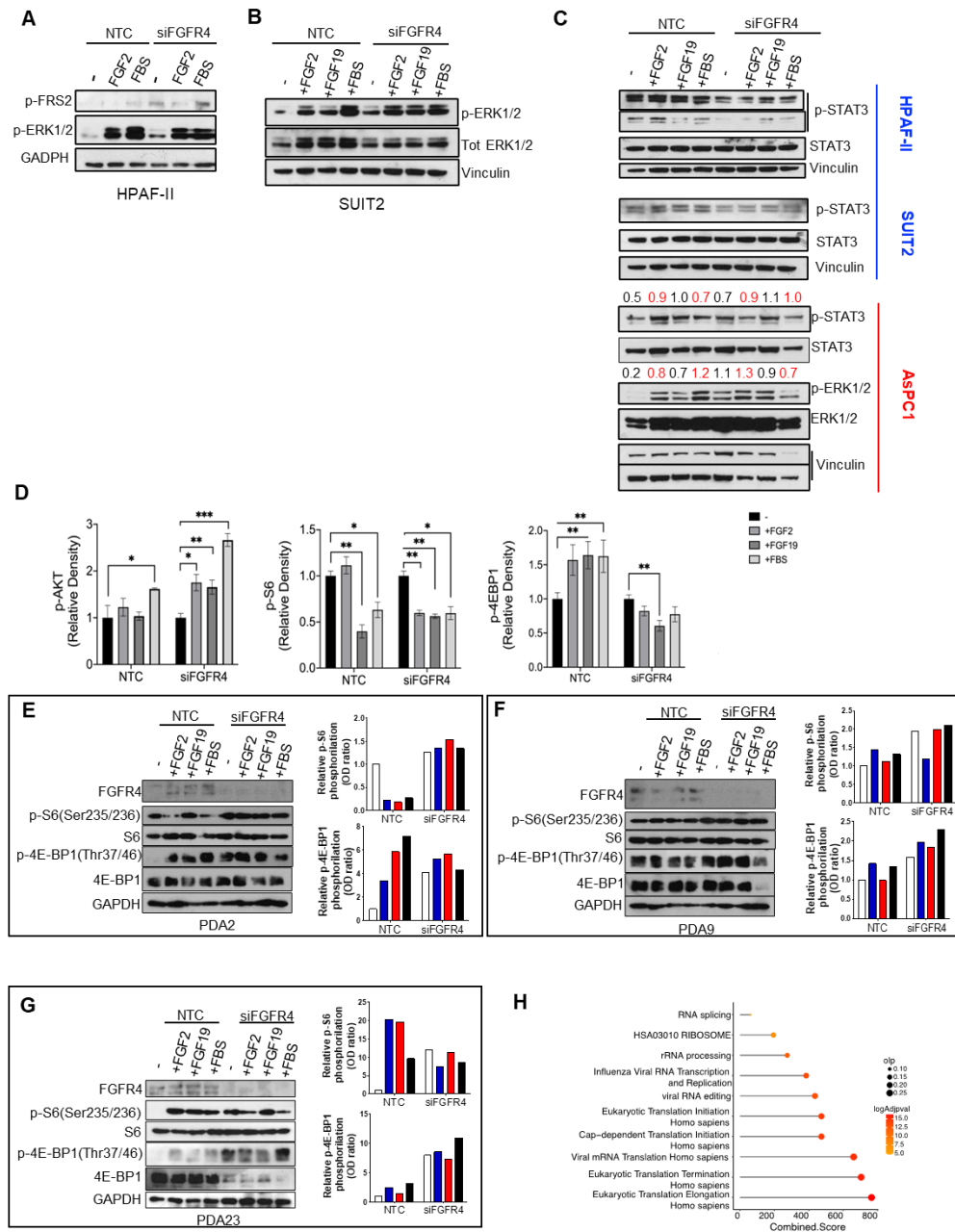
Supplementary Figure 4: **Loss of FGFR4 enhances the malignancy of PDAC cells. A** Representative snapshot of the genomic region of *FGFR4* in MiaPaCa2 (high-grade, basal-like) and Capan-1 (low-grade, classical) from Diaferia et al. (Diaferia et al., 2016) showing histone modification (H3K27ac) and RNA-seq data. **B** Volcano plot of differences in gene expression between control (n = 2) and *HNF1A* knocked down (KD) cells (n = 3). Indicated are some of the genes with log_2FC expression ≥ 2 and adjusted $p < 0.05$. **C** Stacked bar plot showing the distribution of primary and metastatic cases from the PanCuRx cohort

according to the FGFR4 expression status. p, Chi-Square test. **D** Immunoblot for FGFR4 in hT3 PDO transduced with either mock control of the shRNA targeting FGFR4. Vinculin was used as loading control. The transplantations were performed with the hT3 transduced with the sh884. **E** Representative ISH staining of *FGFR1* in PDA9-O transduced with NTC or shFGFR4. Scale bar, 50 μm. **F** Relative growth (as percentage of cell proliferation) of HPAF-II, PDA23, PDA9, and PDA2 cells transiently transfected with either the control vector (NTC) or the siRNA targeting *FGFR4*. Data presented are means ± SD of 3 biological replicates. **G** Enrichment of selected pathways (GSEA) when comparing *FGFR4* low versus *FGFR4* high tumours of the ICGC cohort (Bailey et al., 2016). GSEA was performed using gene sets from REACTOME, GO, Hallmark, and REACTOME databases in MsigDB library. Displayed gene sets that passed false-discovery rate < 0.05.

Supplementary Figure 5: Transcriptional changes associated with the downregulation of FGFR4 in pancreatic cancer. A Expression of classical and basal-like genes in *FGFR4* low versus *FGFR4* high tumours of the ICGC cohort (Bailey et al., 2016). ****, false discovery rate (fdr) < 0.0001; ***, fdr < 0.001; **, fdr < 0.01; and *, fdr < 0.1 by Wald test. **B** Enrichment of Interferon related pathways when comparing *FGFR4* low versus *FGFR4* high tumours of the ICGC cohort (Bailey et al., 2016). **C** Immunoblot analysis of FGFR4 in whole-cell lysates of 3 PDAC cultures transfected with either mock control or siRNA targeting FGFR4. Vinculin was used as loading control. The progenitor and the squamous signature scores were calculated for each culture using GSVA (ssgsea method) and are based on the classification proposed by Somerville et al. (Somerville et al., 2018) **D** GSEA plot evaluating the Gene Program 5 (GP5, c-Myc activity) from the Bailey classificatory (Bailey et al., 2016) upon *FGFR4* knockdown in AsPC1 cell line. **E**

Enrichment of Myc-related and proliferation-related pathways upon downregulation of *FGFR4* in AsPC1. **F-G** Expression of classical (blue) and basal-like (red) markers in cells depleted of *FGFR4* (as compared to parental cells). **H** Immunoblot analysis of E-cadherin in SUIT2 and AsPC1 cells upon knockdown of FGFR4. GAPDH was used as loading control. **I** Expression of *FGFR4* in ductal cells classified as classical or basal-like from Peng et al. (Peng et al., 2019) ****, $p < 0.01$ by Student t test. **J** Samples from Peng et al. ranked by mean *FGFR4* expression in the epithelial compartment. The cases in blue and red were considered as *FGFR4* low (n = 4) and high (n = 4), respectively. **K** Expression of classical/progenitor and basal-like/squamous markers in *FGFR4*^{high} and *FGFR4*^{low} epithelial cells from J.

Supplementary Figure 6: Loss of FGFR4 is associated to hyperactivation of mTORC1 in PDAC. A Immunoblot analyses of p-FRS2, p-ERK1/2 in whole cell lysates from HPAF-II transfected with either control (NTC) or siRNA targeting *FGFR4.* GAPDH was used as loading control. Cells were serum-starved for 8 hours and then either left untreated or stimulated with FGF2 (25 ng/mL), and 2% CS-FBS for 20 minutes. **B** Immunoblot analyses of p-ERK1/2, total ERK1/2 in whole cell lysates from SUIT2 transfected with either control (NTC) or siRNA targeting *FGFR4.* Vinculin was used as loading control. Cells were serum-starved for 8 hours and then either left untreated or stimulated with FGF2 (25 ng/mL), FGF19 (100 ng/mL), and 2% CS-FBS for 20 minutes. **C** Immunoblot analyses of p-STAT3, and total STAT3 in whole cell lysates from HPAF-II, and SUIT2 cell lines (in blue). For SUIT2, the same cell lysates from B were used, therefore the same Vinculin blot

is used for normalization. Bottom panel, immunoblot analysis of p-STAT3, total STAT3, p-ERK1/2, and total ERK1/2 for AsPC1 (in red). Vinculin was used as loading control. Numbers on top of the p-STAT3 and p-ERK1/2 refers to the quantification of the phosphorylated levels by normalizing first for the loading control and then for total level of the proteins. For all panels, cells were serum starved and treated as indicated. **D** Bar plots showing the quantification of changes in the phosphorylated levels of selected proteins (p-AKT, p-S6, and p-4E-BP1) as relative density of the total protein level. From Fig 6C. Data presented as means ± SD of four biological replicates. *, $p < 0.05$; **, $p < 0.01$; ***, $p < 0.001$ by Student's *t*-test. **E-G** Immunoblot analyses of FGFR4, and selected components of the mTORC1 pathway in whole cell lysates from 3 different primary PDAC cell lines transfected with either control (NTC) or siRNA targeting *FGFR4*. GAPDH was used as loading control. Cells were serum-starved for 8 hours and then either left untreated or stimulated with FGF2 (25 ng/mL), FGF19 (100 ng/mL), and 2% CS-FBS for 20 minutes. Quantification of changes in the phosphorylated levels of selected proteins (p-S6, and p-4E-BP1) is provided in the bar plots on the right. **H** Immunoblot analyses of p-4E-BP1 in whole cell lysates from AsPC1 and SUIT2 cell lines treated as in E-G. For both AsPC1 and SUIT2, the same cell lysates from B were used, therefore the same Vinculin blot is used for normalization using the serum-starved mock-transfected cell lines as reference. **I** EnrichR pathway analysis of significantly over-represented genes in HPAF-II lacking FGFR4.

CHAPTER 2

Differential Activation of MAPK Defines Fibroblast Subtypes in Pancreatic Cancer

ABSTRACT

Fibroblast heterogeneity is increasingly recognised across cancer conditions. Given their important contribution to disease progression and therapy response, mapping out fibroblasts' heterogeneity is of outmost importance to devise effective anti-cancer therapies. Cancer-associated fibroblasts (CAFs) are the most abundant cell population in pancreatic ductal adenocarcinoma (PDAC) tissues. Different PDAC neoplastic cell states have been described and many activated CAFs phenotypes. However, whether CAFs phenotypes are differently specified by PDAC cell lineages remains to be elucidated. Here, we used pathway mapping analysis and context-dependent pathway response signatures to infer MAPK activity and dependency in heterogeneous expression data from models and patients' samples. We complemented this approach by in situ expression analysis and found that the stromal, but not epithelial, MAPK activity discriminated basal-like from classical tumours. CAFs displaying elevated MAPK activity were specifically anchored to the basal-like/squamous cells in both human primary tissues and xenotransplantation models. Leveraging scRNA-seq data from mouse tumour tissues following short-term perturbation of the pathway, we found that MAPK signalling pathway is critical to the definition of PDAC CAFs phenotypes. Contrasting the two conditions with known differential pathway activity, we demonstrated the general dependency of myCAFs on MAPK activity obtained gene-expression signatures of CAFs displaying MAPK hyperactivation. Gene expression signatures of MAPK^{high} CAFs (sMEK) from mouse tumours suggested metabolic rewiring and immunoregulatory function. Ligand-receptor analysis in untreated and treated samples identified a MAPK^{high} CAF- epithelial cells crosstalk based on *INHBA* (encoding for Activin-A). Disruption of this crosstalk *in vivo* and

modelling of Activin-A activity *in vitro* suggested a role for this protein in sustaining the basal-like phenotype through suppression of endodermal transcription factor expression. Finally, we found that gene expression signatures of MAPK[high] CAFs correlated with poor prognosis in several cancer conditions, including PDAC, and with reduced response to immunecheckpoint inhibition in bladder cancers.

INTRODUCTION

Pancreatic Ductal Adenocarcinoma (PDAC) is one of the most aggressive cancer with a 5-year survival rate of 11% (Siegel et al., 2022). This dismal prognosis is mainly due to the lack of specific symptoms that leads to a late diagnosis, with only 15-20 % of the patients presenting with a resectable disease (Gobbi et al., 2013). For the patients who are not eligible for surgery, standard chemotherapy provides a modest survival benefit. Two consensus molecular subtypes of PDAC have been proposed based on the transcriptomic profile of neoplastic cells: the classical/progenitor and the basal-like/squamous subtype (Collisson et al., 2011; Moffitt et al., 2015; Bailey et al., 2016; Chan-Seng-Yue et al., 2020). The classical/progenitor subtype is enriched for gene programs driven by endodermal transcription factors (e.g., GATA6, HNF1A and PDX1) and inactivation of SMAD4 (Chan-Seng-Yue et al., 2020, Khloesh et al., 2022; Bailey et al., 2016; de Andrés et al., 2023). Conversely, the more aggressive basal-like/ squamous is characterized by the loss of endodermal identity, the acquisition of squamous programs (such as those driven by ΔNp63), chemoresistance, and immune exclusion (Bailey et al., 2016; Somerville et al., 2018; Shinkawa et al., 2022). Nonetheless, the molecular classification of PDAC have not yet informed clinical management (Martinelli et a., 2017; Aung et al., 2018; Nicolle et al., 2020). A dense desmoplastic reaction with abundant cancer-associated fibroblasts (CAFs) is a hallmark of PDAC tissues and CAFs have been proven to regulate the PDAC micro- and macrosystem (Mahadevan et al., 2007; Shinkawa et al., 2022). Heterogenous phenotypes of CAFs have been described and for a subset of them mechanisms of cancer-induced rewiring provided (Ohlund et al., 2016; Biffi et al., 2019; Elyada et al, 2019; Dominguez et al., 2020). Despite how cancer cells genotype affects CAFs phenotype have been investigated, the effect of different neoplastic cell states on fibroblasts is largely unknown (Tape et al., 2016; Shaashua et al., 2022; Vennin et al., 2019). Here, we sought to investigate whether specific differences in CAFs can be found across cancer subtypes and if those differences have a functional impact on the epithelial phenotype. We undisclosed an important role for the MAPK signalling pathway in the definition of PDAC CAFs phenotypes. We show that the

myCAF transcriptional phenotype is uniquely dependent on a proficient MAPK signalling. Additionally, we demonstrated that hyperactivation of MAPK signalling occurs in myCAFs populating basal-like/squamous tumour niches. We took advantage of scRNA-seq data derived from tumour-bearing mice treated with MEK inhibitor to derive a stromal specific signature (sMEK). Finally, we found that the sMEK signature correlates with poor prognosis in several cancer conditions, including PDAC, and with reduced response to immunecheckpoint inhibition in bladder cancers.

RESULTS

Basal-like PDAC cells bear cancer-associated fibroblasts with elevated MAPK activity

To identify molecular features predictive of resistance to the inhibition of MEK1/2, we treated 6 human cell lines and 5 patient-derived organoid (PDOs) cultures with increasing doses of trametinib (MEKi). Short-term treatment of both classical and basal-like cell lines with subIC50 doses of MEKi effectively inhibited MAPK, while inducing the compensatory activation of the PI3K/AKT pathway in a cell-context dependent manner (Supplementary Figure 1A). In both cell lines and PDOs, the classical lineage and high levels of a transcriptional signature of MAPK activation positively correlated with detrimental effects of MEKi on cell viability (Supplementary Figure S1B, C). A basal-like cell line (Hs766t) displayed sensitivity to MAPK inhibition and the largest variation of the transcriptome following treatment (Supplementary Figure S1E). Finally, the treatment of cell lines with sublethal doses of MEKi for 2 and 7 days did not induce significant changes in cell identity (Supplementary Figure S1E). Then, we used the same transcriptional signature of MAPK activation to infer differential activity of the pathway in an extended set of human cell lines. We explored the transcriptomic data available from the CCLE (n = 41) (Barretina et al., 2012) and those generated in our laboratory (n = 10) to reliably classify cell lines as either basal-like or classical. In this dataset, the MAPK transcriptional signature could not discriminate classical from basal-like cell lines (**Fig. 1A**). When exploring transcriptomic data from tissue cohorts, high levels of the MAPK signature were enriched in the basal-like PDAC of the TCGA (The Cancer Genome Atlas Research Network, 2017) but not of the PanCuRx (Chan-Seng-Yue et al., 2020) or the ICGC (Bailey et al., 2016) cohorts (Fig. 1A). To refine our analyses, we used RNA-seq data from 6 MEKi treated cell lines to derive a transcriptomic signature of MEKi response (epithelial MEK, eMEK) based on downregulated genes only, which we considered as a rough MAPK dependency footprint (Supplementary Figure 1F). Consistent with our observations, the eMEK signature could not discriminate classical from basal-like tumours in the PanCuRx cohort (Chan-Seng-Yue et al., 2020), which contains

RNA-seq data from microdissected epithelia (Supplementary Figure 1G), nor identified patients with different clinical outcomes in the TCGA (The Cancer Genome Atlas Research Network, 2017) and ICGC (Bailey et al., 2016) cohorts (Fig. S1G). The tissues included in the TCGA cohort display, on average, a very low neoplastic cell content (The Cancer Genome Atlas Research Network, 2017). Therefore, we reasoned of a potential contribution of the stromal compartment to the elevated MAPK activation inferred in the basal-like tissues of this cohort. Accordingly, MAPK transcriptional signatures were positively correlated with the levels of stromal genes such as *ACTA2* and *FAP* (Supplementary Figure 1I). Next, we applied a multiplex immunofluorescence approach to human PDAC tissues classified as either basal-like/squamous or classical with well-established tissue markers (Somerville et al., 2018; Kaufmann et al., 2001; de Andrés et al., 2023; Bailey et al., 2016; Martens et al., 2021) (Supplementary Figure 1J, K). We found a significant enrichment for α-SMA$^+$p-ERK$^+$ fibroblasts in the stroma of basal-like/squamous cells (**Fig. 1B**). Intratumor heterogeneity was observed in tissues containing both classical and basal-like cells (**Fig. 1C**). In GATA6^{high} KRT81^{neg} (i.e., classical) tumour regions (Muckenhuber et al., 2018), p-ERK$^+$ CAFs were rarely detected while the opposite was found in KRT81^{high}-expressing tumour regions. Spatial analysis showed that significantly more α-SMA$^+$p-ERK$^+$ CAFs can be found in proximity of basal-like cells (Fig. 1C). Finally, we investigated if this p-ERK$^+$ CAFs were anchored to the basal-like phenotypes using tissues from patient-derived xenografts (PDX) which exhibited class switch following drug treatment. We found that the treatment-induced switch of epithelial subtype was coherently associated with changes in the stroma compartment (**Fig. 1D**). Conversely, when no switch of molecular class was observed following treatment, no changes were evident in the stromal compartment (Supplementary Figure 1L). Pancreatic stellate cells (PSCs) are known precursors of cancer-associated fibroblasts (Helms et al., 2022; Öhlund, Elyada & Tuveson, 2014; Bachem et al., 1998). We serum-starved mouse PSCs (mPSCs) and then briefly exposed them to the conditioned media from either classical or basal-like human PDAC cells before evaluating levels of p-ERK. The conditioned medium from basal-like cells induced nuclear enrichment of p-ERK to the same extent of mouse EGF and significantly

more than the conditioned medium from classical cells (**Fig 1E**). Accordingly, the immunoblot analysis of mPSCs exposed to cell lines' conditioned media confirmed enhanced p-ERK upon exposure to basal-like cells secretome (**Fig. 1F**). Finally, to test whether the p-ERK activation is driven by EGFR receptor activation we performed immunofluorescence for p-EGFR. Our results show that, while mEGF induced EGFR activation, the conditioned medium from basal-like cells did not activate the receptor (Supplementary Figure 1M). Collectively, these data show that basal-like cells harbour CAFs with elevated activity of MAPK.
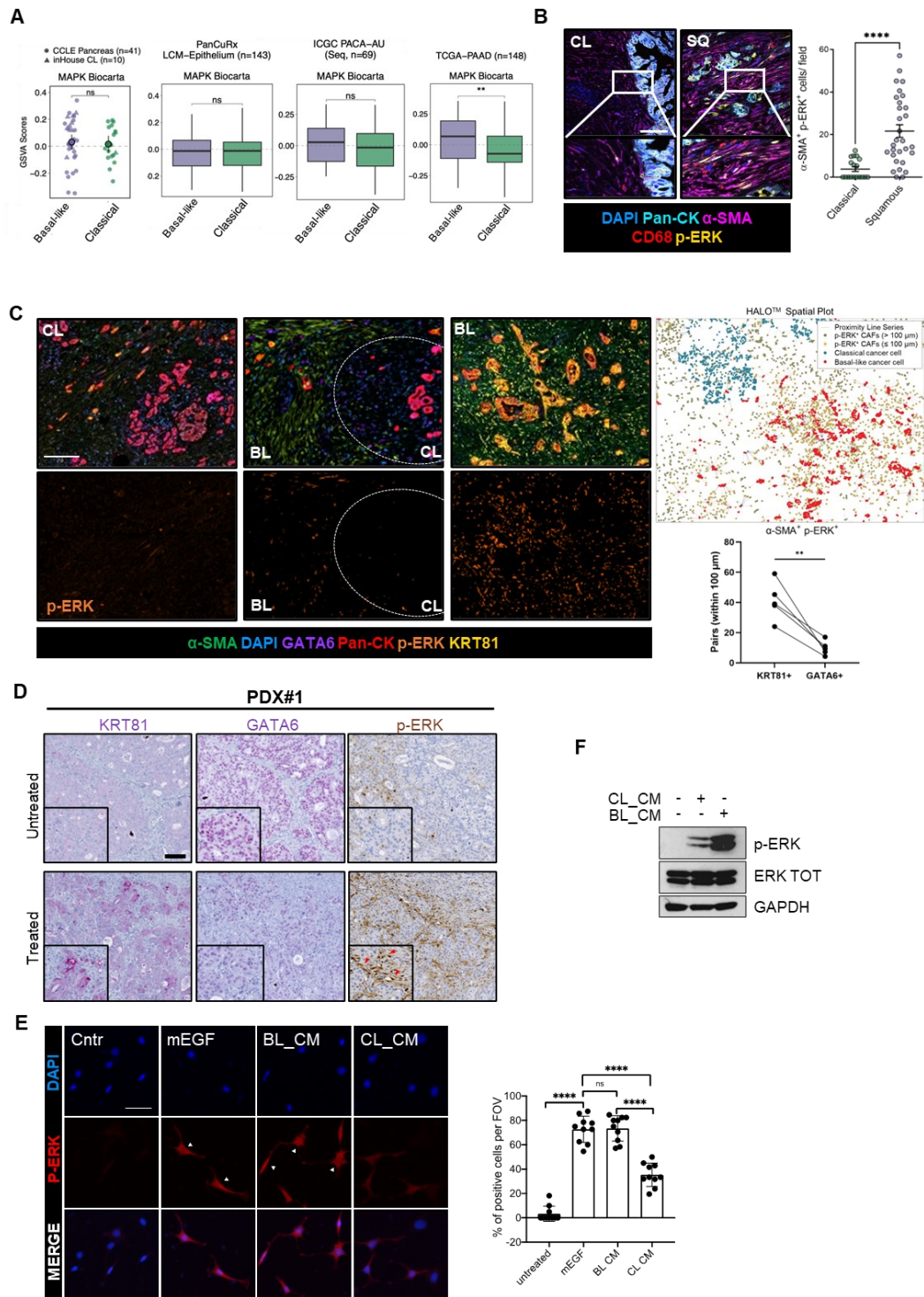
Figure 1. Basal-like PDAC cells bear cancer-associated fibroblasts with elevated MAPK activity A Boxplots of GSVA scores obtained with GSVA Bioconductor package for MAPK Biocarta gene set (MSigDB) stratified by Moffitt subtypes (Moffitt et al., 2015). From left to right: CCLE (Barretina et al., 2012), PanCuRx (Chan-Seng-Yue et al., 2020), ICGC (Bailey et al., 2016), and TCGA (The Cancer Genome Atlas Research Network, 2017). ****p < 0.0001; and ns, not significant as determined by Wilcoxon test. **B** Representative images of multiplex immunofluorescence performed on FFPE of patients with classical (CL, left panel) and squamous (SQ, right panel) PDAC. Scalebar, 100 μm.

Below 2X magnification of the selected area. On the right, scatterplots representing the numbers of α-SMA$^+$p-ERK$^+$ cells per field. ****$p < 0.0001$ as determined by Student's t test. **C** Representative images of multiplex immunofluorescence performed on FFPE of human PDAC tissue. The three panels represent different areas within the same tumour with different classification. CL, classical; BL, basal-like. Scalebar, 200 μm. On the right, the spatial plot obtained with Halo® Image Analysis Platform showing the distribution of p-ERK$^+$ CAFs around classical (GATA6$^+$) and basal-like (KRT81$^+$) cancer cells. Below, the paired dot plot showing the quantification of p-ERK$^+$ CAFs with a distance below 100 μm to classical (GATA6$^+$) and basal-like (KRT81$^+$) cancer cells. **$p < 0.01$ **D** Representative images of immunohistochemistry for KRT81, GATA6 (purple) and p-ERK (brown) on patient derived xenograft (PDX#1) tissues treated with either vehicle or MEK inhibitor. Red arrows indicate p-ERK signal in stroma. Scalebar, 200 μm. Inserts showed 2X magnification of selected areas. **E** Representative immunofluorescence staining of p-ERK (red) on mPSCs FBS-starved for six hours (Cntr) and treated for ten minutes with mEGF (50 ng/ml) and basal-like or classical conditioned media. Nuclei were counterstained with DAPI (blue). Scalebar, 50 μm. White arrows indicate nuclear translocation of p-ERK. On the right, scatter dot plot showing the percentage of cells with p-ERK nuclear translocation per FOV. For each condition, 10 fields were analysed. ****$p < 0.0001$; and ns, not significant as determined by Student's t test. **F** Immunoblot analyses of p-ERK and total ERK in whole cell lysates from mPSCs serum starved for six hours and treated for ten minutes with either classical or basal-like conditioned media. GAPDH was used as loading control.

scRNA-seq of mouse PDAC tumours treated with MEKi reveals quantitative and qualitative changes in cell subsets

To investigate the role of MAPK in the definition of stromal phenotypes, we performed a multidimensional analysis of tissues from mouse basal-like PDAC (**Fig. 2A**). First, we generated and characterized a mouse model based on the orthotopic transplantation of a quasi-mesenchymal KPC derived cells that *in vivo* produces cancer tissues aligning with the human basal-like PDAC (Lupo et al., 2023). Tumor-bearing mice treated daily with 1 mg/Kg of MEKi showed reduced activation of MAPK and compensatory activation of the PI3K/Akt pathway (Supplementary Figure 2A). Multiplex IF of tissues from tumour-bearing mice treated over the course of 14 days showed the presence of p-ERK⁺ CAFs in untreated tumours, the reduction of p-ERK signal in both the epithelial and stromal compartments at 2 days following treatment, and the rapid pathway rewiring particularly in the stromal compartment at 7 days of treatment (**Fig. 2B**). In keeping with that, the reactivation of the MAPK pathway occurred *in vitro* within hours from the treatment of mouse CAFs (Supplementary Figure 2B). Given the kinetics of the MAPK pathway rewiring, we then performed scRNA-Seq on fresh tissues from tumour-bearing mice treated for 2 and 7 days with MEKi along with their untreated controls. We profiled a total of 18495 cells across 12 tumours (6 untreated and 6 treated) and recovered an overall cellular composition similar to that expected from PDAC tissues (**Fig. 2C, D**). Unsupervised clustering of single cell data identified 11 major cell types (Fig. 2C). Further annotation of the identified cell subsets was performed *post ho*c by using known gene signatures (Fig. 2D). The main cluster was composed by malignant epithelial cells which were confirmed by inferred copy-number alterations (CNA) (Tirosh et al., 2016) (not shown). Other cell types included non-malignant epithelial cells (i.e. acinar cells), immune and stromal cell types (Fig. 2C, D). The treatment was associated with significant changes in cell composition and cell states. We observed a reduction in the proportion of malignant epithelial cells both at 2 and 7 days of treatment (**Fig. 2E, F**), which was consistent with the histology of treated tumours (Supplementary Figure 2C). In the non-malignant compartment, we observed a higher fraction of CAFs in the treated groups that was also confirmed with immunohistochemistry

with the fibroblast marker FAP (Supplementary Figure 2C). Consistent with the pharmacological treatment and the proteomic analysis, the eMEK transcriptional signature was significantly downregulated in the treated tumours (**Fig. 2G**). Furthermore, cell cycle related signatures (Hwang et al., 2022) were downregulated by the treatment (Supplementary Figures 2D, E) which was consistent with reduced fraction of Ki67$^+$ cells in the tissues (Supplementary Figure 2F). Conversely, even if apoptosis related transcriptional programs were enriched in treated epithelial cells the staining of tissues with cleaved-caspase 3 (CC3) did not show prominent induction of apoptosis (Supplementary Figures 2D, E, G). We then investigated whether the treatment affects the cancer cell subtype at single cell resolution. Our bulk RNA-seq data showed that the tumour subtype is not strongly affected by MEK inhibition, while scRNA-seq data revealed a little but significant increase in the number of classical neoplastic cells after 2 and 7 days of treatment with MEKi (not shown; **Fig. 2H**). Overall, our data are consistent with a cytostatic rather than cytotoxic effect of MEKi.
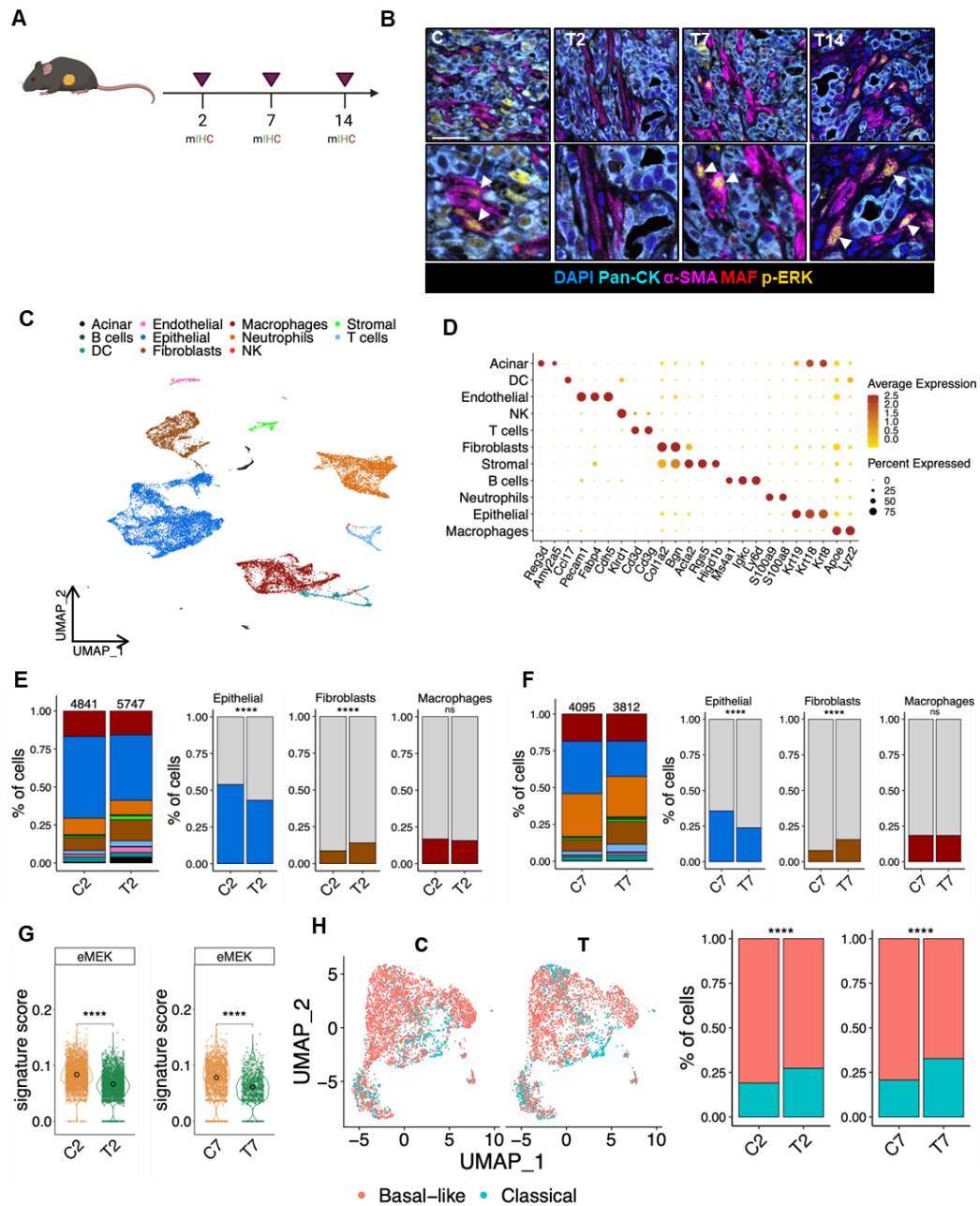
Figure 2: scRNA-seq of mouse PDAC tumors treated with MEKi reveals quantitative and qualitative changes in cell subsets A Schematic representation of the *in vivo* experimental setting. Mice were treated daily with Trametinib (1mg/Kg) for 2, 7, or 14 days. At each timepoint, a group of mice have been sacrificed and further analysis performed. **B** Representative images of multiplex immunofluorescence performed on tumour tissues from mice treated with (from left to right): vehicle, MEKi for 2 (T2), 7 (T7), and 14 (T14) days. White arrowheads indicate α-SMA⁺/p-ERK⁺ cells. Bottom panels showed a 2X magnification of selected areas. Scalebar, 25 μm. **C** UMAP plot showing the unsupervised clustering of viable cells from 12 digested mouse tumours tissues (6 vehicle and 6 treated) annotated in 11 different clusters. Different cell type clusters are color-coded. **D** Bubble plot showing selected cell type-specific markers across clusters. Size of dots represents the percentage of cells expressing a specific marker and intensity of color indicates level of average expression. **E** Barplots representing the percentage of cells for

each cell type cluster from mice treated with either vehicle (C2) or MEKi (T2) for 2 days. On top is reported the total number of cells for each sample. On the right, barplots representing the percentage of cells for a specific cluster (epithelial, fibroblasts, and macrophages) from mice treated with either vehicle or MEKi for 2 days. ****$p < 0.0001$; and ns, not significant as determined by Wilcoxon test. **F** Barplots representing the percentage of cells for each cell type cluster from mice treated with either vehicle (C7) or MEKi (T7) for 7 days. On top is reported the total number of cells for each sample. On the right, barplots representing the percentage of cells for a specific cluster (epithelial, fibroblasts, and macrophages) from mice treated with either vehicle or MEKi for 7 days. ****$p < 0.0001$; and ns, not significant as determined by Wilcoxon test. **G** Violin plots representing the signature score value of the eMEK signature of cells from mice treated with either vehicle or MEKi for 2 days (left) and 7 days (right). ****$p < 0.0001$ as determined by Wilcoxon test. **H** Umap plots showing cells of the epithelial cluster of vehicle (C) and MEKi (T) treated mice, classified as classical and basal-like according to Moffitt classification (Moffitt et al., 2015). On the right, barplots showing the percentage of cells of the epithelial cluster of mice treated either with vehicle (C) and MEKi (T) for 2 and 7 days, classified as classical and basal-like according to Moffitt classification (Moffitt et al., 2015). ****$p < 0.0001$ as determined by Wilcoxon test.

MAPK inhibition induces changes in the proportion of myCAFs and iCAFs

Within the CAFs compartment, the treatment did not partition cells into distinct clusters (Supplementary Figure 3A). Established signatures of CAFs commonly found in mouse and human PDAC tissues (Elyada et al., 2019) were expressed in distinct clusters of cells, which could be detected across conditions (treated/untreated) and timepoints (2 and 7 days) (**Fig. 3A**). The main subset of CAFs was composed by myCAFs, while apCAFs was the less represented one in all the conditions (Fig. 3A). As observed for the malignant epithelial compartment, the treatment induced quantitative and qualitative changes in the fibroblasts compartment. We observed a significant reduction in the proportion of myCAFs after treatment which was associated with an increase in the number of fibroblasts classified as iCAFs (**Fig. 3B**). These relative changes were more prominent at two days following MEKi. Considering all CAFs subsets, the treatment induced the significant downregulation of the MAPK transcriptional signature (Supplementary Figure 3B). However, the myCAFs compartment showed the largest variation in gene expression upon treatment, which suggests a higher dependency of this CAFs phenotype on MAPK activity (**Fig. 3C**). Then, we moved onto exploring the possibility that MEKi could affect the differentiation status of CAFs. First, we used CytoTRACE (Gulati et al., 2020) to predict the differentiation status of the two main CAFs subsets in untreated and treated tumors. Regardless of the treatment, iCAFs and myCAFs were at the opposite ends of the differentiation spectrum (**Fig. 3D**), with iCAFs showing the lowest transcriptional diversity and therefore predicted to be the more differentiated cell subset. Next, we used Velocyto to infer pseudotemporal trajectory from scRNA-seq data (La Manno et al., 2018). In untreated tumours, no dominant pseudotrajectory could be identified (**Fig. 3E**). Conversely, a dominant pseudotrajectory from myCAFs to iCAFs was inferred in treated tumours, supporting MAPK as a relevant pathway for the maintenance of the myCAFs phenotype (Fig. 3E). To orthogonally validate these findings, we first explored scRNA-Seq from untreated tumours to identify reliable markers of myCAFs and iCAFs subsets. We found that *Tnc* and *Mmp3* (Forsthuber et al., 2023; Mucciolo et al., 2022) were highly expressed in cell subsets showing strong

myCAFs and iCAFs phenotypes, respectively (Supplementary Figure 3D, E). *In situ* hybridization analysis (ISH) of mouse PanIN from autochthonous models driven by oncogenic K-RAS (Hingorani et al., 2003) revealed expression of *Tnc* in proximity of epithelial cells while abundant stromal cells expressing *Mmp3* were found surrounding each lesion (Supplementary Figure 3F). In cancer tissues from autochthonous models driven by mutations of K-RAS and TP53 (Hingorani et al., 2005), both *Tnc* and *Mmp3* expressing cells showed a spatial segregation consistent with that observed for myCAFs and iCAFs phenotypes in this model (Öhlund et al., 2017; Biffi et al., 2019) (Supplementary Figure 3G). Next, we performed *in situ* hybridization in tissues from our mouse cohort. Consistent with the scRNA-seq data, the treatment induced significant changes in the proportion of myCAFs and iCAFs (**Fig. 3F**). After two days of MEKi, there was a drastic reduction in the number of *Tnc* expressing cells with a concomitant increase in *Mmp3* expressing cells (Fig. 3F). To further generalize our findings and understand whether this myCAFs into iCAFs transdifferentiation induced by the treatment occurred independently by the epithelial cell lineage, we analysed tissues obtained from additional mouse models of classical and basal-like PDAC (Godfrey et al., 2022) (Supplementary Figure 3G-F)**.** Short-term treatment (two days) of tumour-bearing mice was consistently associated with an increase in iCAFs in the stroma also in classical tumours (Supplementary Figure 3G). Altogether, our data indicates that MAPK activity is a key determinant of the myCAFs phenotype *in vivo*.
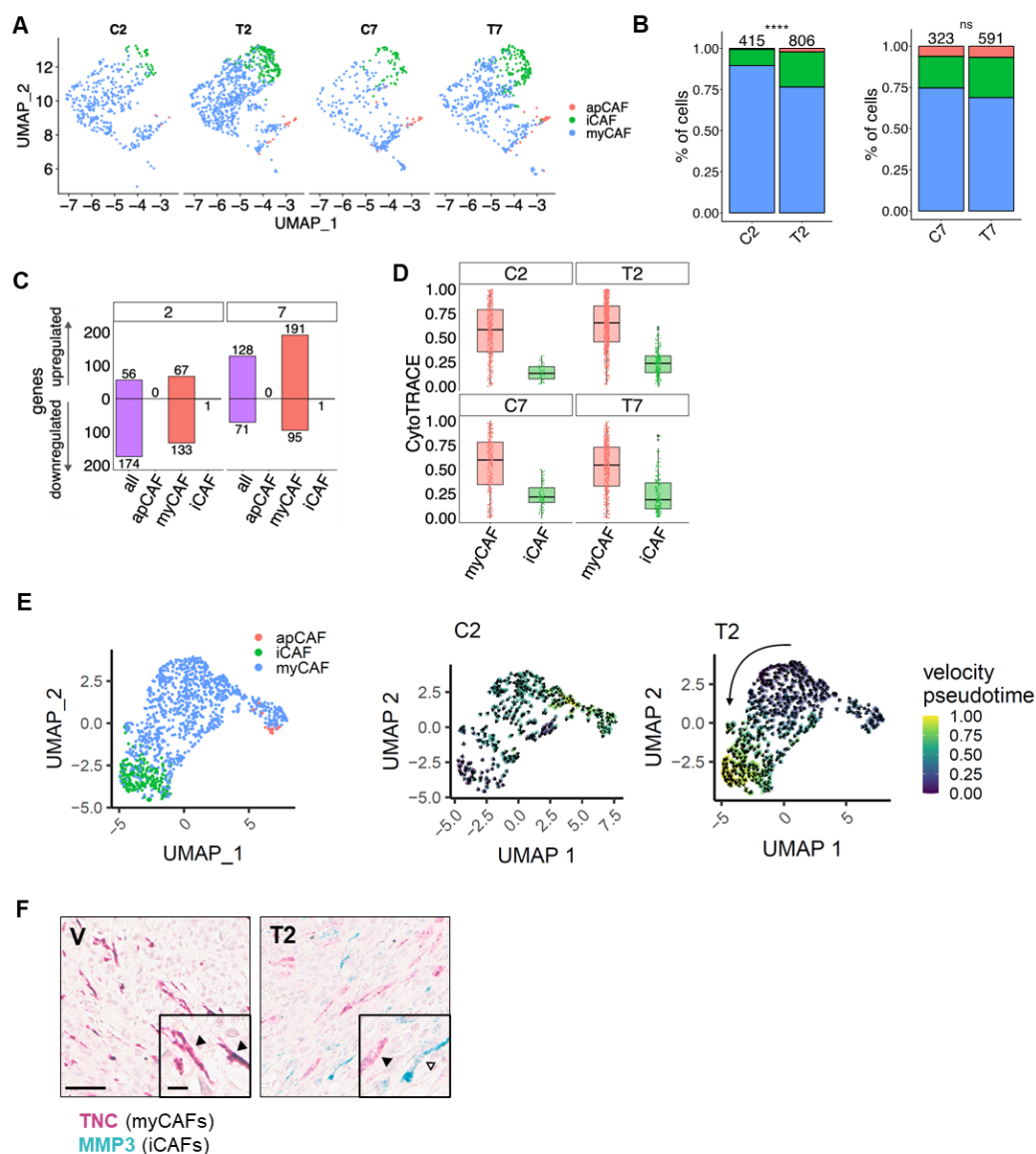
Figure 3: MAPK inhibition induces changes in the proportion of myCAFs and iCAFs
A UMAP plot of cells from the fibroblast cluster representing the CAFs subtype for each cell (stratified according to Elyada's classification (Elyada et al., 2019)) from mice treated with either vehicle or MEKi for 2 or 7 days. **B** Barplots representing the percentage of cells of the fibroblast cluster classified according to Elyada's subtypes (myCAFs, iCAFs, and apCAFs (Elyada et al., 2019)) from mice treated either with vehicle or MEKi for 2 days (C2, T2) or 7 days (C7, T7). On top is reported the total number of cells for each sample. ****$p < 0.0001$, ns as not significant as determined by Wilcoxon test. **C** Barplots showing the number of genes up- and down-regulated in cells of the fibroblast cluster after 2 and 7 days of treatment with MEKi. Cells are stratified using Elyada's classification (Elyada et al., 2019). **D** Scatterplot showing the CytoTRACE value (Gulati et al., 2020) for cells of the fibroblast cluster treated either with vehicle or MEKi for 2 days (C2, T2) or 7 days (C7,

T7), classified according to Elyada's subtypes (apCAFs not shown (Elyada et al., 2019)). **E** On the left, UMAP plot of the fibroblast cluster obtained by the integration of cells from mice treated with either vehicle or MEKi for 2 days (C2, T2). The colour visualization represents Elyada's subtypes (Elyada et al., 2019). On the right, UMAP representing the velocity (arrows) and pseudotime (colour) for each cell of the fibroblast cluster (annotated on the left panel) from mice treated with either vehicle or MEKi for 2 days. Black arrow indicated the global directionality of the velocity. **F** Representative images of *in situ* hybridization showing expression of *TNC* (red; myCAFs) and *MMP3* (green; iCAFs) genes on PDAC tissue from mice treated with either vehicle (V) or MEKi for 2 days (T2). Scalebar, 60 µm. Insert showed a 2X magnification of selected areas. Black arrowheads indicate myCAFs, while white arrowheads indicate iCAFs.

A MAPK CAF signature identify a subcluster of myCAFs and is associated to basal-like tumours

To identify subset of CAFs with elevated activity of MAPK in our scRNA-Seq data, we derived a transcriptomic signature based on genes significantly downregulated by two days of MEKi in the CAFs compartment (sMEK) (**Fig. 4A,** Supplementary figure 4A, see method section). Next, we classified cells by quartiles of mean z-score of the sMEK signature (n = 169) and defined as MAPK^{high} CAFs the cells in the highest quartile. This subset of CAFs formed a somewhat distinct cluster of cells in untreated tumours (**Fig. 4B**) and was almost exclusively composed by myCAFs (**Fig. 4C**). We obtained the same results when the signature was re-sized to contain 25 genes (Supplementary Figure 4B). Consistent with the dynamic of MAPK inhibition in our model, the proportion of CAFs expressing the sMEK signature reduced after 2 days of treatment to then increase at 7 days (**Fig. 4D**). Next, we explored the overlap between the sMEK signature and signatures of either MAPK activation or CAFs phenotype. In keeping with their myofibroblastic phenotype, 8 genes of the sMEK signature were also included in the myCAF signature proposed by Elyada and colleagues (Elyada et al., 2019) (n = 23) (Supplementary Figure 4C). No significant overlap was observed with other signatures. We then used PROGENy (Schubert et al., 2018) to infer pathway activity in each CAFs subset from the untreated tumours. In line with previous reports (Öhlund et al., 2017; Biffi et al., 2019; Elyada et al., 2019; Dominguez et al., 2020; Krishnamurty et al., 2022), myCAF were characterized by elevated activation of TGFβ, while iCAFs were enriched for inflammation-associated signalling pathways (**Fig. 4E**). MAPK^{high} CAFs were characterized by elevated TGFβ and MAPK activity, the enrichment of hypoxia-driven responses, and activity of inflammatory pathways (Fig. 4E). Gene-set enrichment analysis (GSEA) on the list of differentially expressed genes between CAFs with high and low MAPK activity confirmed a metabolic reprogramming as well as the activation of inflammation-associated transcriptional programs in MAPK^{high} CAFs (Supplementary Figure 4D). Accordingly, MAPK^{high} CAFs expressed high levels of *Slc2a1, PGK1, Eno1, PKM* and some cytokine/chemokines such as *Il11* and *Mif* (not shown). In addition, the sMEK signature positively correlated with *TGFB1* in the TCGA datasets (**Fig. 4F**).

In our *in vitro* setting, mPSCs exposed to conditioned media from both basal-like and classical cell lines showed induction of iCAF genes and activation of the JAK-STAT pathway, which was reported to be the driver of the iCAF phenotype (Biffi et al., 2019) (**Fig. 4G**, Supplementary Figure 4E). Therefore, mPSCs were pre-treated for two days with TGF-β1 in order to attenuate the polarization towards iCAFs and then exposed for 24 hours to either basal-like or classical CM. We observed that, along with stronger ERK phosphorylation, the basal-like CM induces the sMEK signature (**Fig. 4H**, Supplementary Figure 4E). Of note, treatment with TGF-β1 upregulated the sMEK signature as well, in accordance with the myofibroblastic nature of the sMEK^{high} CAFs (Fig. 4H). Moreover, the sMEK signature identified basal-like tumours from the TCGA cohort (The Cancer Genome Atlas Research Network, 2017) (**Fig. 4I**) and was enriched in the stroma of human tumours displaying a greater proportion of basal-like cells from the scRNA-seq dataset of Peng et al. (Peng et al., 2019) (**Fig. 4J,** Supplementary Figure 4F). Given the strong association with basal-like tumours, we sought to investigate whether sMEK^{high} CAFs present specific interactions with the epithelium. The ligand-receptor analysis performed with CellPhone DB shows unique interactions between sMEK^{high} CAFs and epithelial cells (**Fig 4K**). The analysis revealed that only sMEK^{high} CAFs are the source of INHBA which is predicted to interact with activin receptors on the epithelial compartment (Fig 4H). Accordingly, INHBA is in the top 10 genes of the sMEK signature and is the gene with the highest score in the DEG between sMEK^{high} and sMEK^{low} CAFs (Fig 4A; not shown). INHBA is the subunit of the homodimer Activin A, therefore we tested the effect of Activin A on cancer cells *in vitro*. We treated the classical cell line HPAF-II with 100 ng/ml of Activin A for 3 days and evaluate the change in expression of classical markers (**Fig 4K**). The treatment induced a significant downregulation of CDH1, PDX1, and GATA6 in HPAF-II (Fig 4K). Accordingly, a similar trend on detected classical marker was observed on the basal-like cell line Hs766t after 3 and 6 days of treatment with Activin A (Supplementary Figure 4G). Overall, those data suggest that MAPK^{high} CAFs potentially release Activin A, which reduce the classical

identity of cancer cell. This effect is consistent with the increased number of classical cancer cells observed after MEK inhibition *in vivo* (Fig 2H).
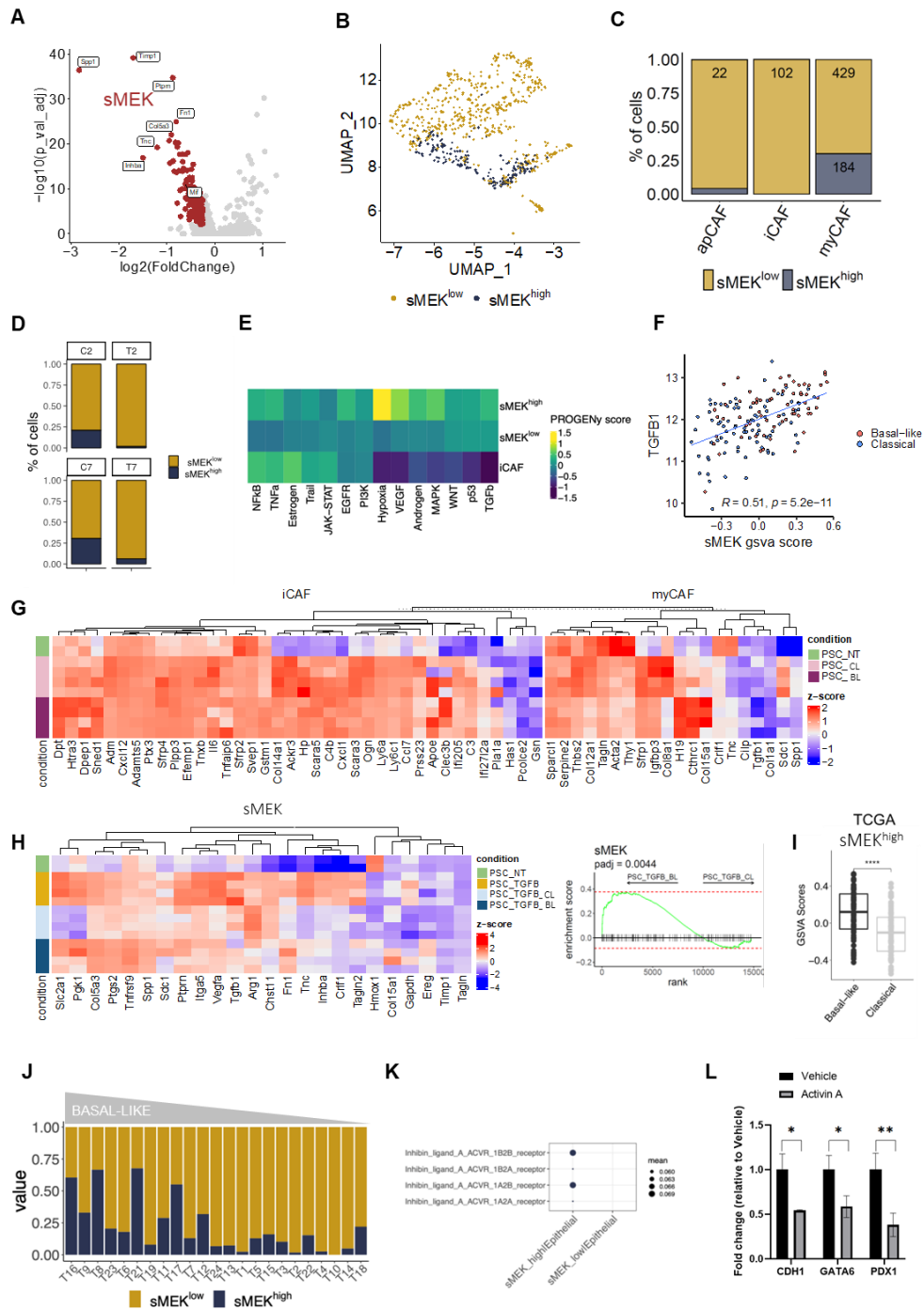
Figure 4: A MAPK CAF signature identify a subcluster of myCAFs and is associated to basal-like tumours **A** Volcano plot representing the genes down- and up-regulated in fibroblasts upon treatment with MEKi for 2 days *in vivo*. The red dots are the genes that are part of the sMEK signature (n=168). Highlighted some of the genes with log2FC expression > 2 and adjusted $p < 0.05$. **B** UMAP plot of cells from the fibroblast cluster stratified according to the signature sMEK (divided as high and low) from mice treated with vehicle for 2 and 7 days. **C** Barplots representing the percentage of cells of the fibroblast cluster with high (blue) and low (yellow) values for the sMEK signature

classified according to Elyada's subtypes (myCAFs, iCAFs, and apCAFs (Elyada et al., 2019) from mice treated with vehicle. **D** Barplots representing the percentage of cells of the fibroblast cluster with high (blue) and low (yellow) values for the sMEK signature in vehicles (C2, C7) and in MEKi treated samples (T2, T7). **E** Heatmap showing the expression of pathway-responsive genes in specific CAFs phenotypes as assessed by PROGENy analysis (Schubert et al., 2018). **F** Scatter plot showing the positive correlation between *TGFB1* mRNA expression and the sMEK gsva score for the TCGA cohort (The Cancer Genome Atlas Research Network, 2017) stratified according to Moffitt subtypes (Moffitt et al.,2015). **G** Heatmap showing changes in the expression of the genes in the myCAFs and iCAFs signatures from Elyada et al. (Elyada et al., 2019) in mPSCs treated with conditioned media from classical and basal-like cell lines for 24 hours. Z-scores derived from DESeq2-VST transformed counts. **H** On the left, heatmap showing changes in the expression of the genes in the sMEK signature in mPSCs treated with either TGF-β1 (5 ng/ml) for 72 hours or pre-treated with TGF-β1 for 48 hours and additionally treated with conditioned media from classical and basal-like cell lines for 24 hours. On the right, GSEA plot evaluating the sMEK signature in mPSCs pre-treated with TGF-β1 for 48 hours and additionally treated with conditioned media from classical and basal-like cell lines for 24 hours. **I** Boxplot of GSVA scores for the sMEK[high] signature in the sample of the TCGA cohort (The Cancer Genome Atlas Research Network, 2017) classified as Classical or Basal-like according to Moffitt's subtypes (Moffitt et al.,2015). ****$p < 0.0001$. **J** Barplots showing the percentage of cells of the fibroblast cluster with high values for the sMEK signature in samples of the Peng et al. (Peng et al.,2019) cohort ordered accordingly to decreasing basal-like cells content. **K** Ligand receptor analysis using CellPhone DB on scRNA-seq data from mice treated with vehicles for 2 and 7 days. **L** Barplots showing the fold change in expression of selected genes in HPAF-II treated with Activin A (100 ng/ml) for 3 days.

The sMEK signature can be found across several human cancer types and predicts poor clinical outcome

In the majority of the PDAC cohorts investigated (n = 4; Zhang et al., 2012; Yang et al., 2016; Chen et al., 2015; Kirby et al., 2016), high levels of the sMEK signature outperformed established stromal signatures (Moffitt et al., 2015) in identifying patients with inferior overall survival (**Fig. 5A, B** Supplementary Figure 4H). Furthermore, we found that basal-like tumours displaying elevated levels of the sMEK signature had the worse prognosis (Supplementary Figure 4I). Next, we performed a single-cell pan-cancer analysis across 10 tumour types (Luo et al., 2022), including PDAC, to evaluate whether the expression of the sMEK signature could be observed in the fibroblasts compartment of other tumour types. The signature was enriched in the fibroblast vs other cell types in the majority of cancer indications (**Fig. 5C**). In three tumour types (i.e., lung adenocarcinoma, bladder cancer, and uveal melanoma), elevated levels of the sMEK signature correlated with worse patient prognosis (**Fig. 5D**). sMEK signature is detected across several cancer types and correlates with level of TGF-beta expression, a known predictor of poor response to immuno-oncology therapies (Mariathasan et al., 2018; Principe et al., 2019). Therefore, we next sought to test whether it correlates with response to cancer immunotherapy. The sMEK signature is enriched in patients with worse response to immunotherapy (stable and progressive disease) in patient with bladder cancer (BLCA) in the cohort from Dominguez et al. (Dominguez et al., 2020) (**Fig. 5E**). Accordingly, elevated level of the sMEK signature correlated with reduced survival in BLCA patients treated with anti–PD-L1 therapy (Dominguez et al., 2020) (Fig. 5E). Overall, those data suggest that the sMEK signature is not pancreas-specific and can predict poor outcome also in other cancer types.
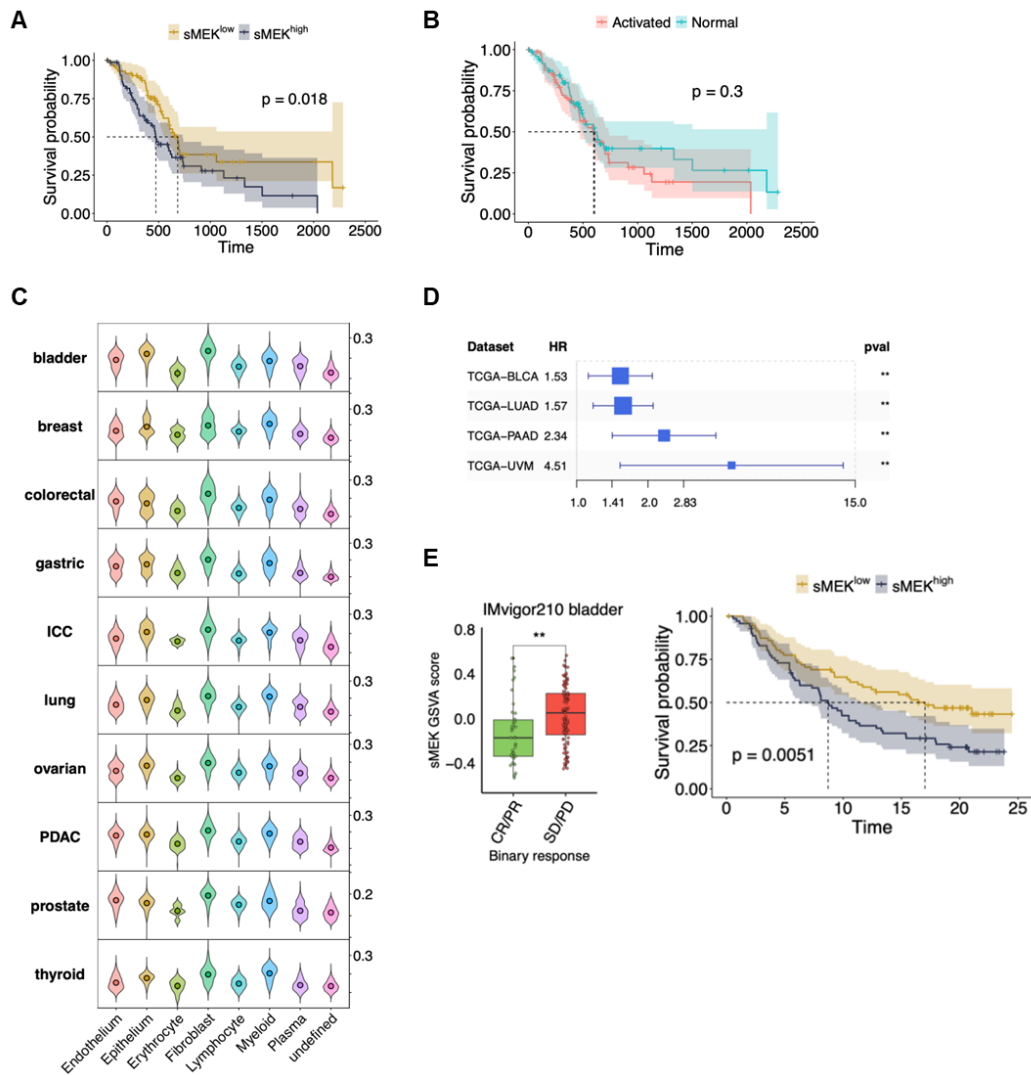
Figure 5: The sMEK signature can be found across several human cancer types and predicts poor clinical outcome **A** Kaplan–Meier plot comparing the overall survival of patients from the TCGA cohort (n = 148) (The Cancer Genome Atlas Research Network, 2017) according to the expression of the sMEK signature. p, Log-rank (Mantel–Cox) test. **B** Kaplan–Meier plot comparing the overall survival of patients from the TCGA cohort (n = 148) (The Cancer Genome Atlas Research Network, 2017) according to Moffitt's stromal subtypes (Moffitt et al., 2015). p, Log-rank (Mantel–Cox) test. **C** Violin plots representing the score values for the sMEK signature of cells from different cellular type clusters from the Luo et al. dataset (Luo et al.,2022). **D** Forest plots showing the hazard ratio for the sMEK signature in 4 of human tumour types from the TCGA cohort (TCGA (The Cancer Genome Atlas Research Network, 2017). ** $p < 0.01$ as determined by Wilcoxon test. **E** On the left, Boxplot showing sMEK GSVA score over IMvigor210 bladder samples separated by drug response. CR, complete response; PR, partial response; SD, stable disease; PD, progressive disease. ** $p < 0.01$ as determined by Wilcoxon test. On the right, Kaplan–Meier plot comparing the survival probability of BLCA patients

treated with immunotherapy from the cohort of Dominguez et al (Dominguez et al., 2020) according to the expression of the sMEK signature. p, Log-rank (Mantel–Cox) test.

DISCUSSION

Here, we undisclosed an important role for the MAPK signalling pathway in the definition of PDAC CAFs phenotypes. Our data show that the myCAF transcriptional phenotype is uniquely dependent on a proficient MAPK signalling. Furthermore, hyperactivation of MAPK signalling occurs in myCAFs populating basal-like/squamous tumour niches. Gene expression signatures of MAPK[high] CAFs (sMEK) from mouse tumours suggested metabolic rewiring and immunoregulatory function. Finally, we found that the sMEK signature correlated with poor prognosis in several cancer conditions, including PDAC, and with reduced response to immunecheckpoint inhibition in bladder cancers. Our findings support previous observation about the importance of MAPK signalling in sustaining the myCAFs phenotype (Mucciolo et al. 2022) and expand on the heterogeneous phenotypes that can be found in the PDAC TME. We provide new insights on a stromal phenotype specifically shaped by basal-like/squamous cells. Signalling pathway activities and cell dependency on a given pathway are often successfully inferred from gene expression data (Szalai & Saez-Rodriguez, 2020; Schubert et al., 2018). Here, we used pathway mapping analysis and context-dependent pathway response signatures to infer MAPK activity and dependency in heterogeneous expression data from models and patients' samples. In both human cancer cell lines and patient-derived organoids, high level of a MAPK transcriptional signature was the best predictor of sensitivity to MEK1/2 inhibition. Basal-like/squamous models were predicted to be less dependent on MAPK activity and accordingly displayed reduced sensitivity to MEKi. *In vitro*, a transiently disabled MAPK pathway was not associated with significant changes of cancer cell states. Our results are in line with previous observation from Miyabayashi and colleagues showing that RAS signalling hyperactivation is not fundamental for the definition of the basal-like/squamous subtype (Miyabayashi et al., 2020). We have previously shown that querying bulk transcriptional datasets derived from tissues with different neoplastic cell content is a viable strategy to localize the cellular compartment contributing to gene expression differences between molecular subtypes (D'Agosto et al., 2022). Using the same approach, we show that MAPK transcriptional signatures were particularly elevated in basal-like tumours from the TCGA cohort (The Cancer

Genome Atlas Research Network, 2017). The inferred hyperactivation of MAPK in the stromal compartment of tumours classified as basal-like significantly correlated with increased density of fibroblasts displaying nuclear p-ERK, a known surrogate marker for MAPK activation (Zhang et al., 2002). Different neoplastic cell states often co-exist in human PDAC tissues (Krieger et al., 2021; Juiz et al., 2020; Chan-Seng-Yue et al., 2020; Hwang et al., 2022). Therefore, molecular subtyping based on bulk sequencing data might mask transcriptional heterogeneity (Chan-Seng-Yue et al., 2020; Raghavan et al., 2021). Immunophenotyping of heterogeneous human tumours clearly showed that p-ERK$^+$ CAFs were enriched in basal-like/squamous niches. These pERK$^+$ CAFs can be detected in mouse PDAC tumours as well as in heterospecies models, which were instrumental to demonstrate that this CAFs subpopulation is specifically anchored to the basal-like subtype. Indeed, treatment induced changes in cancer cell lineage was accordingly associated with qualitative changes in the stroma, i.e. increased or decreased p-ERK$^+$ CAF density. To gain further insights into this CAFs phenotype, we leveraged scRNA-seq data obtained from mouse tumour tissues following short-term perturbation of the MAPK pathway. Our model aligned with the human basal-like/squamous PDAC (Lupo et al. 2023) and showed rapid kinetics of pathway rewiring following treatment. Short-term perturbations are often used to capture primary transcriptional response to a specific stimulus (Somerville et al., 2020; Biffi et al., 2019). Contrasting the two conditions with known differential pathway activity, we were able to show the general dependency of myCAFs on MAPK activity and to obtain gene-expression signatures of CAFs displaying MAPK hyperactivation. Our model poorly recapitulates the tissue architecture of human PDAC and that of autochthonous models. However, the model preserved the CAFs heterogeneity reported in mouse and human tumours (Öhlund et al., 2017; Biffi et al., 2019; Elyada et al., 2019; Dominguez et al., 2020), the expected myCAFs/iCAFs ratio in the PDAC TME (Buechler et al., 2021; Dominguez et al., 2020), and showed pERK$^+$ CAFs as expected for a basal-like model. Inferred dynamics in scRNA-seq data and *in situ* expression analyses showed that MAPK inhibition leads to dramatic changes of the myCAFs/iCAF ratio into the mouse PDAC TME. The highest degree of dependency of myCAFs on MAPK activity suggests a potential transdifferentiation

of myCAFs into iCAFs. However, we cannot exclude that changes of the myCAFs/iCAFs ratio observed following MEKi are also contributed by qualitative changes into the malignant compartment. Focusing on CAFs showing the highest dependency on MAPK activity, we obtained a gene expression signature (sMEK) that mapped almost exclusively onto the myCAFs subcluster. This result is coherent with the spatial localization of pERK[+] CAFs in human tissues, i.e. proximal to neoplastic cells. Accordingly, the sMEK signature is enriched for ECM related genes and shows a partial overlap with the published myCAFs signature (8 genes out of 21) (Elyada et al., 2019). Nonetheless, the sMEK signature suggest a peculiar metabolic rewiring of myCAFs driven by a hypoxic-like response and putative immunoregulatory functions. Aligning with their myCAFs identity, TGF-β signalling was a major driver of MAPK[high] CAFs and accordingly treatment of mouse PSCs with TGF-β1 greatly induced the sMEK signature *in vitro*. Furthermore, the signature was also strongly induced when mPSCs were exposed to the conditioned media from basal-like human cancer cell lines. That further suggests that this phenotype is anchored to basal-like cancer cells. In different PDAC cohorts, the sMEK signature reliably identified patients with worse prognosis. That is in contrast with the epithelial specific MEK signature which failed to stratify patients based on risk. Previous studies have shown that similar fibroblast lineages and phenotypes can be observed in different cancer conditions (Buechler et al. 2021; Kieffer et al., 2020; Galbo et al., 2021). We explored pan-cancer scRNA-seq data to find that the sMEK signature is enriched in stromal cells from many cancer conditions and identifies more aggressive disease in some of them. While deeper mechanistically investigations are needed, our data suggest at least two potential functions for the MAPK[high] CAFs.

Ligand-receptor analysis in untreated and treated samples identified a MAPK[high] CAF- epithelial cells crosstalk based on *INHBA*, which codify for a subunit of the homodimer Activin A, produced by the CAFs in the untreated status. Activin A is a member of the TGF-beta superfamily, whose stromal expression and plasmatic levels were already correlated with poor survival in PDAC (Mancinelli et al., 2021; Chen et al., 2022; Yu et al., 2023; Yi et al., 2022; Togashi et al., 2015). Activin A is significantly downregulated in CAFs following treatment with MEKi.

Furthermore, short-term MEKi was also associated with a slight increase in the number of classical PDAC cells. Therefore, we tested whether Activin A might contribute to antagonize the emergence of the classical phenotype. Differently from the treatment with TGF-β1 (D'Agosto et al., 2023), the treatment of the classical cell line HPAF-II with Activin A did not induce the expression of EMT-like genes but rather significantly reduced the expression of endodermal transcription factors. Endodermal TFs are important for the maintenance of the classical phenotype and epigenetically silenced in the basal-like/squamous tumours (Khloesh et al., 2022; Bailey et al., 2016; de Andrés et al., 2023). Another potential function for this CAFs subtype is immunoregulatory. sMEK signature include genes with immune-related function and high level of the signature predict poor response to immunotherapy in bladder cancers. In sum, our study shows that MAPK signalling is a key determinant of the myCAFs phenotype and that its hyperactivation is a distinctive feature of stromal cells in basal-like/squamous tumour niches. Inhibition of MAPK signalling using a potent MEK1/2 inhibitor has important consequences on stroma remodelling with transient changes in myCAFs to iCAFs ratio. We also provide here a gene-expression signature that might be used for patients' stratification based on risk in PDAC and other cancer conditions.

MATERIALS AND METHODS

Human samples

Human PDAC tissues used in this study were obtained from surgical resections of patients treated at the University and Hospital Trust of Verona (Azienda Ospedaliera Universitaria Integrata, AOUI). Written informed consent was acquired from patients before specimens' acquisition. The FFPE samples used for multiplex immunofluorescence and immunohistochemistry were retrieved from the ARC-Net Biobank and were collected under the protocol number 1885 approved by the local Ethics Committee (Comitato Etico Azienda Ospedaliera Universitaria Integrata) to A.S. (Prot. 52070, Prog. 1885 on 17/11/2010). Tissues from surgical resection used for the generation of organoids were collected under the protocol number 1911 approved by the local Ethics Committee (Comitato Etico Azienda Ospedaliera Universitaria Integrata) to V.C. (Prot. n 61413, Prog 1911 on 19/09/2018). All experiments were conducted in accordance with relevant guidelines and regulations.

The Essen cohort is a retrospective study carried out according to the recommendations of the local ethics committee of the Medical Faculty of the University of Duisburg-Essen. Clinical data were obtained from archives and electronic health records. Patients who had undergone pancreatic resection with a final histopathologic diagnosis of human PDAC between March 2006 and February 2016 was used (Approval no: 17-7340-BO).

Cell lines and organoids

The murine PDAC cell line FC1199, the murine stellate cell line mPSCs, the human PDAC cell lines (hT1, hM1, and hF2) and organoid hT3 (VR02-O) were kindly provided by the Tuveson's laboratory (Cold Spring Harbor Laboratory, NY, USA). Hs766T were kindly provided by Prof. Aldo Scarpa (University of Verona). FC1199 were generated from PDA tumours from KPC (Kras$^{G12D/+}$; p53$^{R172H/+}$;

Pdx1-Cre), while mPSCs have been established from WT C57BL/6J mice (Hingorani et al., 2005; Öhlund et al., 2017). FC1199[luc/Gfp] cells were generated using procedures reported elsewhere (Buckley et al., 2015). The human cell lines PANC-1 and HPAF-II were purchased from ATCC (CRL-1469™, CRL-1997™). FC1199, PANC-1, and HPAF-II were cultured in DMEM (Gibco) supplemented with 10% FBS (Gibco) and 1% Penicillin-Streptomycin (Pen-Strep, Gibco). hT1, hM1, hF2, and Hs766T were grown in RPMI 1640 (Aurogene) supplemented with 10% FBS and 1% Pen-Strep. mPSCs were cultivated in DMEM supplemented with 5% FBS and 1% Pen-Strep. PDAC organoids (VR01-O, VR03-O, VR04-O, and VR05-O) were established and cultured as described previously (Boj. et al., 2015; Huch et al., 2013). 60400 and 110299 were generated from PDA tumours derived from CKP (Ptf1a[wt/Cre]; Kras[wt/LSL-G12D]; p53^{fl/fl}) mice (Mazur et al., 2015). VR01-O (Sample Code ID: HCM-CSHL-0080-C25), VR03-O (Sample Code ID: HCM-CSHL-0077-C25), VR04-O (Sample Code ID: HCM-CSHL-0081-C25), and VR05-O (Sample Code ID: HCM-CSHL-0092-C25) have been acquired as part of the Human Cancer Model Initiative (HCMI) https://ocg.cancer.gov/programs/HCMI, and are available on ATCC. Cells and organoids were routinely screened for Mycoplasma contamination using MycoAlert Mycoplasma Detection Kit (Lonza).

Animal studies

In this study we used both isograft and xenograft models. Six- to eight- weeks old C57Bl/6J (B6J) and NSG (NOD.Cg-Prkdc[scid];Il2rg[tm1Wjl]) mice were purchased from Charles River Laboratory (Milan). All animal experiments regarding transplanted mice were conducted in accordance with procedures approved by CIRSAL at University of Verona (approved project 655/2017-PR). KC (Kras[G12D/+]; Pdx1-Cre) and KPC (Kras[G12D/+]; p53[R172H/+]; Pdx1-Cre) mice were used as spontaneous model for pre-invasive lesions and PDAC, respectively (Hingorani et al., 2003; Hingorani et al., 2005). Isograft models were generated with KPC and CKP-derived cell lines. For the generation of isograft based on KPC-derived cell line (FC1199), 2.5x105 cells were transplanted in B6J mice as previously described

(Lupo et al., 2023). For the generation of isograft based on CKP-derived cell lines (60400 and 110299), 5.0×10^5 cells were resuspended in 30 µL of a 1:1 dilution of Matrigel® (Corning) and cold plain medium and injected into the pancreas of B6J mice using insulin syringes (BD micro-fine 30 Gauge) under the guidance of Ultrasonic imaging. The injection was considered successful by the appearance of encapsulated cell suspension ball without signs of leakage. Patient-derived xenografts (PDX#1, PDX#2) were generated by subcutaneous implantation of a patient's tumour fragment in the left flank of anaesthetized NSG mice. Tumour growth was measured twice weekly until they reached the volume of 1 cm³. Then, tumours were harvested, cut into small fragments (3 mm3) and transplanted subcutaneously into the left flank of anaesthetized NSG to generate the 2nd generation of xenograft. The same procedure was followed to generate the 3rd generation of xenograft which was used for treatments. Mice were maintained under sterile and controlled conditions (22°C, 50% relative humidity, 12 h light–dark cycle, autoclaved food and bedding, acidified drinking water).

Drug treatments

For *in vitro* experiments, cells were counted and seeded in a 6 well plate or a $100 cm^2$ dish. After reaching 40% of the confluence, cells were treated for the time reported in each experiment (for longer treatment, Trametinib was refreshed every 2 days). Trametinib (Selleck) was dissolved in DMSO, whose final concentration was less than 0.1% (v/v). PDAC cell lines have been treated with subIC50 concentration: HPAF-II (IC50 = 4.8 nM), PANC-1 (IC50 = 10000 nM), Hs766t (IC50 = 2.85 nM), hF2 (IC50 = 4.54 nM), hM1 (IC50 = 1.35 nM), hT1 (IC50 = 148.8 nM). mPSCs have been treated with MEKi with a concentration of 10 nM. For *in vivo* experiments, Trametinib was dissolved in a solution of 0.5% hydroxypropyl-methylcellulose, 0.2% tween 80 and ddH2O (pH 8) for oral administration.

The xenograft tissues were derived from 2 PDX treated with or without MEKi (4 weeks) from the CAM-PaC (Integrative Analysis of Gene Functions in Cellular and Animal Models of Pancreatic Cancer) cohort4.

For orthotopic models, mice were treated with or without MEKi for 1 or 2 weeks for 60400 and 110299 derived tumours, respectively.

Conditioned media treatments

Conditioned media was collected from cancer cell lines after 48h of conditioning (confluence of the cells around 70%) and used to treat mPSCs for 1 hours. When shown, mPSCs have been pre-treated with TGFβ1 5 ng/ml (Peprotech) for 48 hours. When FBS starvation was required, conditioned media was collected from cancer cell lines after 15h of conditioning in serum starvation (confluence of the cells around 70%) to avoid aspecific signaling activation caused by FBS and used to treat mPSCs (starved for 6 hours) for 10 minutes. Treatment with conditioned media for RNA-seq experiment was done for 24 hours on mPSCs either pre-treated or not with TGFβ1 (5 ng/ml) for 48 hours.

Activin A treatment and rt-qPCR

PDAC cell lines were plated in 6 well plates with their usual culture media and treated with 100 ng/ml Activin A (R&D System) for 3 and 6 days, as reported. After treatment RNA was collected using TRIzol (Life Technologies). RNA extraction was performed by column-based purification with the PureLink RNA Mini Kit (Ambion). 1 µg of RNA was retrotranscribed in cDNA using the SensiFAST cDNA Synthesis Kit (Bioline) following the manufacturer's protocol. Samples were diluted to a final concentration of 10 ng/µL. TaqMan was performed in triplicate using 20 ng of cDNA and the following TaqMan® probe (TaqMan® Gene Expression Assay): *GATA6* (Hs00232018_m1), *PDX1* (Hs00236830_m1), and *CDH1* (Hs01023894_m1). *HPRT1* (Hs02800695_m1) was used as reference gene. Relative gene expression quantification was performed using the ΔΔCt method with the Sequence Detection Systems Software, Version 1.9.1 (Applied Biosystems).

Histology and Immunohistochemistry

Tissues were fixed in 10% neutral buffered formalin and embedded in paraffin. Sections were subjected to Hematoxylin and Eosin as well as immunohistochemical staining. After deparaffinization and heat-induced antigen retrieval (performed with citrate buffer pH=6) slides were incubate with blocking solution for 1 hour at room temperature. The following primary antibodies were used for immunohistochemical staining of mouse tissues: Cleaved Caspase-3 (#9661, Cell Signaling Technology), Ki67 (#D2H10, Cell Signaling Technology), p-ERK (#9101; #4376, Cell Signaling Technology), GATA6 (#AF1700, Bio-techne; #ab175349, Abcam) KRT81 (sc-100929, Santa Cruz Biotechnology Inc.), and FAP (#ab53066, Abcam). The following primary antibodies were used for immunohistochemical staining of human tissues: PDX1 ([EPR3358(2)] #ab134150, Abcam), CK5 (#XM26, Novocastra), ΔNP63 (ACI3066C, Biocare), S100A2 (#109494, Abcam), GATA6 (#AF1700, Bio-techne), and p-ERK (#9101, Cell Signaling Technology). After overnight incubation with the primary antibody, slides were incubated with Rabbit-specific secondary antibody (Vector Laboratories) for 30 minutes at room temperature. The slides were then subjected to Fast Red or DAB chromogen development. Slides were scanned at 20x magnification and digitalized using the Aperio Scan-Scope XT Slide Scanner (Aperio Technologies). Quantification of FAP was performed in at least ten random nonoverlapping fields of visualization (FOV, 20x) in each tissue using ImageJ. To measure the percentage of brown pixels, DAB^+ particles were counted automatically by the software after colour deconvolution of the image. The percentage is relative to the number of nuclei present in each of the selected areas. Quantification of CC3 and Ki67 was performed in at least ten random nonoverlapping FOV (40x) by counting the number of brown nuclei/cells for each selected area. Areas of extensive immune cell infiltration (e.g., infiltrating lymph nodes or tertiary lymphoid structures) were avoided.

Multiplex Immunofluorescence

Opal Multiplex IHC Kit (Akoya) was used to perform multiplex immunofluorescence on human and mouse tissues. The following antibodies have been used: pan-Keratin (#4279, Cell Signaling Technology), p-ERK (#9101, Cell Signaling Technology), α-SMA (#ab5694, Abcam), CD68 (#76437, Cell Signaling Technology), and MAF (# A300-613A, Bethyl). Briefly, FFPE sections were deparaffinized and subjected to several sequential microwave treatments and stainings. Each cycle includes five steps: (i) antigen retrieval by heat-induced epitope retrieval with citrate buffer (pH6), (ii) aspecific sites blocking, (iii) primary antibody incubation, (iv) incubation with Secondary-HRP antibody, and (v) incubation with Opal Fluorophore for 10 min at room temperature. After all the sequential staining reactions, sections were counterstained with DAPI (Vector lab) and mounted with Fluoromount^{TM} mounting solution (Diagnostic BioSystem). Slides were scanned with Leica TCS SP5 laser scanning confocal (Leica) with 80x objective magnification and digitalized by the Leica Application Suite X (LAS X) software. Quantification was performed in at least three random nonoverlapping FOV (80x) by counting the number nuclei/cells with staining positivity for each selected area.

Multiplexed IF on PDAC tissue of figure 1C, was conducted using the Opal multiplex system (Perkin Elmer, MA) in accordance with manufacturer's instructions. In brief, FFPE sections were deparaffinized, then fixed with 4% paraformaldehyde, and the antigens were retrieved using tris/EDTA (pH9) to induce epitope retrieval by heat-induced epitope retrieval. Each section was put through multiple rounds of staining; each included endogenous peroxidase blocking and protein blocking, as well as primary antibody and the corresponding secondary horseradish peroxidase-conjugated polymer (Zytomed Systems, Germany or Perkin Elmer). Tyramide signal amplification was used to bind each horseradish peroxidase conjugated polymer with different fluorophores. To remove antibodies before the next round of staining, additional antigen retrieval in heated Tris/EDTA (pH9) was performed. Sections were counterstained with DAPI (Vector lab) after

all sequential staining reactions. With 10x objective magnification, slides were scanned and digitalized by Zeiss Axio Scanner Z.1 (Carl Zeiss AG, Germany).

Spatial imaging analysis

The binary information of cellular and nuclear signals was co-registered after generating intensity thresholds for each fluorescent channel. Java and R algorithms were used to automatically analyse cell distances. Using ImageJ, overlapping mask regions were employed to identify cells, which were marked with a point at the centre of the DAPI+ cell nucleus. This analysis was performed by using the R Package Spatstat1 for converting cell coordinates into Euclidian distances between cells. Using the algorithm, any two cells are ranked according to their average distance and number of unique neighbours. The threshold to pair up two cells was set to 100µm.

Immunofluorescence

$5x10^3$ mPSCs were plated in each well of a cell culture chamber slide (4 well, Corning). After 48 hours, cells were serum starved for 6 hours and treated for 10 minutes with conditioned media from cancer cell lines. 50 ng/ml mEGF was used as positive control for p-ERK nuclear translocation. After treatment, cells were fixed for 10 minutes with 4% PFA and permeabilized with 100% methanol for 10 minutes at -20°C. Slides were incubated with blocking solution for 1 hours and subsequently with the primary antibodies p-ERK (#9101, Cell Signaling Technology) and p-EGFR (#3777, Cell Signaling Technology) overnight at 4°C. The secondary antibody Alexa 488-labeled anti-rabbit (1:500) (Invitrogen) was incubated for 1 hour at room temperature. The slides were then incubated with DAPI (Vector Laboratories) for 30 minutes and mounted with FluoroMount® mounting medium (Clinisciences). Images were acquired at 20X using EVOS Cell Imaging System (Thermo Fisher Scientific). Quantification was performed by counting cells with nuclear signal for p-ERK per FOV divided by the total number of cells counted in the field (10 field of view per condition).

In Situ Hybridization

The *in-situ* hybridization (ISH) was performed on 4 μm section of mouse tissues. Briefly, slides were deparaffinized in xylene for 10 minutes followed by 100% ethanol for 2 minutes. After drying, slides were first incubated for 10 minutes with RNAscope® Hydrogen Peroxide (Advanced Cell Diagnostics) and then for 15 minutes at 99°C with RNAscope® 1X Retrieval Reagents (Advanced Cell Diagnostics). After dehydration in 100% ethanol, slides were dried and incubated at 40°C for 20 minutes with RNAscope® Protease Plus (Advanced Cell Diagnostics). The RNAscope® Probes (Mm-Mmp3 and Mm-Tnc-C2, Advanced Cell Diagnostics) were added to the slides following RNAscope® 2.5 Duplex Detection Reagents kit's instructions. Positive control probe 2.5 Duplex Positive Control Probe-Mm and 2-plex Negative Control Probe (Advanced Cell Diagnostics) were used as positive and negative control, respectively. After chromogens signal development, slides were counterstained with 1:5 diluted hematoxylin, dried and mounted with VectaMount® mounting medium (Vector Laboratories). Slides were scanned at 40x magnification and digitalized using the Aperio Scan-Scope XT Slide Scanner.

Immunoblotting

Protein lysates were obtained from cells using Cell Signaling Lysis Buffer (Cell Signaling Technology) supplemented with phosphatases and proteases inhibitors (PhosSTOP™ and cOmplete (TM) Mini Protease Inhibitor Co, Roche). Samples, prepared with NuPAGE™ LDS Sample Buffer (4X) (Novex) and NuPAGE™ Sample Reducing Agent (10X) (Novex), were incubated for 10 minutes at 99°C for proteins denaturation. For electrophoresis, sample were loaded in in 4%–12% Bis-Tris NuPage gels (Life Technologies). After separation, proteins were transferred on a PVDF membrane (Life Technologies) and blocked with Non-fat dry milk (Santa Cruz Biotechnology). Membranes were incubated overnight in agitation at 4°C with the following primary antibodies: p-ERK (#9101, Cell Signaling

Technology), total ERK (#9102, Cell Signaling Technology), p-AKT (#4060, Cell Signaling Technology), total AKT (#9272, Cell Signaling Technology), p-S6 (#D57.2.2E/4858, Cell Signaling Technology), total S6 (#54D2, Cell Signaling Technology), p-SMAD2 (#3108, Cell Signaling Technology), p-STAT3 (#9145, Cell Signaling Technology), total STAT3 (#12640, Cell Signaling Technology), and GATA6 (#ab175349, Abcam, 1:1000). Vinculin (#4650, Cell Signaling Technology) and GADPH (#5174, Cell Signaling Technology) were used as loading controls. Membranes were then incubated for 1 hour at room temperature with the following secondary antibodies: Goat anti-Rabbit IgG (HRP) (1:1000, Thermo Fisher Scientific) and HRP-Donkey Anti-Mouse IgG (1:5000, Jackson ImmunoReseach). The immunoblots were visualized with ECL Star Enhanced Chemiluminescent substrate (Sigma Aldrich).

RNA sequencing and data processing

RNA was extracted from cell lines (PDAC and mPSCs), organoids or freshly isolated tissues (isografts) using TRIzol (Life Technologies), followed by column-based purification with the PureLink RNA Mini Kit (Ambion). The quality of purified RNA samples was determined using a Bioanalyzer 2100 (Agilent) with RNA 6000 Nano Kit. RNAs with RNA Integrity Number (RIN) values greater than 7.5 were used to generate sequencing libraries using the TruSeq Stranded Total RNA Kit (Illumina) following manufacturer's instructions. RNA-Seq libraries prepared from cell lines treated with vehicle or MEKi for 2 and 7 days (n=6), organoids (n=5), mPSCs (n=6), and mice PDAC tissues were run by Eurofins genomics using the Illumina HiSeq2000 platform with paired-end reads of 75 bases with a final coverage of 3 million reads per sample. After quality control and adaptor trimming, reads were aligned to the GRCh38 genome using Salmon v1.4.0 (Patro et al., 2017). Transcripts quantification was imported in R through tximport package v4.0 and raw counts were normalized using the R/Biocondutor package DESeq2 v1.30.0 (Love et al., 2014). Differentially expression analysis has been performed using DESeq2 (Love et al., 2014). GSVA R package v1.38.2

(Hänzelmann et al., 2013) was used to calculate the main PDAC transcriptomics subtypes gene set scores (Moffitt et al., 2015).

Statistical Analysis and Data mining

For data mining and molecular classification of tumours we used different gene expression datasets. Four datasets were used: the PACA-AU cohort of the ICGC consortium (Bailey at al., 2016), the TCGA-PAAD (n=178), TCGA-LUAD (n=539), TCGA-UVM (n=80), and TCGA-BLCA (n=412) cohorts of the TCGA consortium (The Cancer Genome Atlas Research Network, 2017), PanCuRx (Chan-Seng-Yue et al., 2020) (EGA archive accession EGAS00001002543), and Cancer Cell line Encyclopedia (CCLE) (Barretina et al., 2012). The ICGC dataset contains normalized expression values (TMM normalized using edgeR Bioconductor package, converted to CPM and log2 transformed) of 96 pancreatic cancer patients. The TCGA-PAAD consists of the RNA-Seq gene expression profile of 178 pancreatic cancer patients. Samples number was restricted to 148 due to unclear histology of some samples. PanCuRx dataset contains data from 143 microdissected PDAC patients and it was pre-processed with STAR v2.7.6a (Dobin et al., 2013) and RSEM v1.3.1 (Li et al., 2011). CCLE dataset contains data about 25 pancreatic cell lines and the TPM matrix was downloaded. Dataset from Zhang et al. (n = 45) and Yang et al. (n = 69) contains human primary pancreatic tumour tissues from PDAC (fresh frozen) patients Affimetrix microarray data. Dataset from Chen et al. (n = 63) contains human primary pancreatic tumour tissues (macrodissected) from PDAC (fresh frozen) patients Affimetrix microarray data. Dtaset from Kirby et al. (n = 51) contains human primary pancreatic tumour tissues (microdissected) from PDAC (fresh frozen) patients RNA-seq data.

Survival analysis has been performed through the R packages survival v3.5.0 (https://CRAN.R-project.org/package=survival) and the graphical representation done with survminer v0.4.9 (). GraphPad Prism was used for graphical representation of data. Unless indicated, all the p-values refer to Student t test.

Mouse single cell RNA sequencing

Sample preparation and sequencing

Single cell RNA sequencing was performed on digested PDAC tissues from mice treated with either vehicle or MEKi for 2 or 7 days. For the digestion, tumour samples were collected in Splitting Medium (AdDMEM/F12 medium supplemented with HEPES (10 mM, Gibco), Glutamax (Gibco), and Pen/Strep (Gibco)) supplemented with 0.1% BSA and Rho Kinase Inhibitor (10.5uM, RhoKi). After washing with PBS (Gibco), specimens were cutted in small pieces (1 mm^3) and incubated for 20 minutes in a tube rotator at 37°C in warm Digestion Medium (PBS 1X, 2mg/mL Dispase I (Gibco), 1.25mg/mL Collagenase Type II (Gibco), 100ug/mL DNAse I (Sigma), and 0,05% FBS (Gibco)) supplemented with RhoKi. The cell suspension was pipetted and incubated on ice to let the larger tissue clumps settle to the bottom of the tube. The surnatant was collected, spun down and the pellet was resuspended in Splitting Medium supplemented with 0.1% BSA and 10mg/ml Soybean trypsin inhibitor and stored on ice (Fraction 1). Then, the larger undigested clumps were digested again for 10 minutes, and every step previously described was repeated twice until the collection of Fraction 2 and 3. After digestion, Fractions 1, 2, and 3 were combined, filtered (40um nylon cell strainer) and centrifuged. The pellet was then resuspended in ACK lysing buffer supplemented with DNAse I to remove red blood cells from the sample and spun down. Cells were washed twice with PBS supplemented with 10% FBS and $1x10^4$ cells (concentration 1.000 cells/ul) were submitted to sequencing. To generate single cell GEMs, cellular suspensions were loaded on a GemCode Single Cell Instrument (10x Chromium System) and libraries were generated with GemCode Single Cell 3' Gel Bead and Library Kit v3 (10x Genomics). After barcoding, GEMs were broken and cDNA was cleaned with with DynaBeads MyOne Silane Beads. cDNA was amplified, cleaned with the AMPure beads and the quality was checked using Fragment Analyzer HS NGS Assay. Libraries were quantified by quantitative PCR (qPCR) (KAPA Biosystems Library Quantification Kit for Illumina platforms) and the sequencing was performed on NextSeq500 (Illumina) with 75 paired-end kit.

Data processing

Binary base call (BCL) files, output of the NextSeq500 runs, were processed with the 10X proprietary software Cell Ranger, with default and recommended parameters. FASTQs files were aligned to reference transcriptome GRCm38 by count pipeline. Counts matrices for all samples were imported with Seurat (v3.2.3). Cells with low quality were filtered from counts matrices (200 <n° of genes x cell< 9000 & %mitochondrial gene count < 25%). Vehicle and treatment datasets were Integrated using Seurat integration pipeline (Stuart et al., 2019), clustering analysis were run on integrated dataset with Seurat FindCluster (Stuart et al., 2019) function using a resolution of 1. Annotation of the dataset were performed looking at the expression of well-known cell type markers. Copy number analysis was performed on Epithelial compartment with InferCNV R package (Tirosh et al., 2016) using as reference the non-epithelial cells of the samples.

Subtyping and enrichment analysis

Subtyping of epithelial and fibroblast compartment was performed using as reference respectively the signature from Moffitt et al (Moffit et al., 2015) and from Elyada et al (Elyada et al., 2019). Genes of the Moffitt signature were traduced in their orthologue mouse version using biomaRt R package (Durinck et al., 2009). To assess cell subtypes, an enrichment score was assigned for each gene set to each cell using UCell R package (Andreatta et al., 2021), the cell subtype was assigned based on maximum score achieved by a cell for a specific gene set. Other tested signatures were obtained through the msigdb packages (Bhuva et al., 2023) and from Hwang et al. (Hwang et al., 2022). The related single cell enrichment score was computed with UCell package (Andreatta et al., 2021).

## Analysis of the fibroblast subcluster

Differential gene expression analysis of fibroblast cluster subtypes treated with vehicle and MEKi in the two timepoint was performed with Seurat function FindMarkers (Stuart et al., 2019), the results were filtered according to pvalue<0.05 and 0.25<log2FoldChange<-0.25. Differentiation analysis of fibroblasts subtypes were performed with CytoTRACE package (Gulati et al., 2020) using default

parameters. Fibroblast compartment was extrapolated from the integrated atlas and was subclustered with FindCluster (Stuart et al., 2019) function of Seurat using a resolution of 0.4. Resolution value for subclustering was decided after evaluation with clustree (Zappia et al., 2018) (spanning in the range of 0:1.8 with pass 0.1) to have stable clustering results. Features of the CAFs subclusters were evaluated by marker genes expression. Of the 7 subclusters, 4 were annotated as CAFs due to expression of both subtype signature genes (Hwang et al., 2022) and other well-known panCAF genes expression; the three remaining clusters were annotated as Cycling, EMT-like and Myeloid-like. To perform velocity analysis, the matrices of spliced and unspliced RNA counts were obtained, for the four conditions, from raw data using velocyto pipeline (La Manno et al., 2018) under default parameters. The resulting matrices were uploaded in Seurat objects selecting cells from CAFs subclusters. The objects were integrated with Seurat integration pipeline by timepoints, regressing out cell cycle effect. Computation of velocity and velocity pseudotime values was performed through velociraptor R package, using default parameters and precomputed PCA values. sMEK signature was derived by filtering results of differential expression from Seurat function FindMarkers (Stuart et al., 2019) between vehicle and MEKi treated CAFs subclusters in 2 days timepoint, filtering according to pvalue<0.05 and 0.25<log2FoldChange<-0.25. Signature enrichment score were computed on fibroblast compartment using UCell R package (Andreatta et al., 2021). Vehicle CAFs were classified as sMEK^{high} CAF if their signature enrichment score were above the third quartile of the score's distribution among vehicle cells. The same value was then used on treated samples cell as threshold for classification of cells in sMEK high and low subclasses. Enrichment pathway analysis on the sMEK^{high} and sMEK^{low} CAFs subclass was performed both with PROGENy (Schubert et al., 2018), following the default steps, and with fgsea package using as input the ordered gene list from differential gene expression analysis performed with FindMarkers function and pathways from HALLMARK, REACTOME, and GO collections from msigDB.

Human single cell RNA sequencing datasets

Single cell RNA-seq dataset from Peng et al. (Peng et al., 2019) (primary PDAC = 24, ncells = 41964) was downloaded from Genome Sequence Archive (GSA) Project PRJCA001063 together with dataset annotation metadata. The data were preprocessed using Seurat (Hao et al., 2021) for quality control and filtering (percent_mt_max = 20, nFeature_min = 500, nCount_min = 500, nCount_max = 50000). Subtyping of tumor epithelial cells and fibroblast compartment was performed using as reference respectively the signature from Moffitt et al (Moffitt et al., 2017) and from Elyada et al (Elyada et al., 2019). Genes of the Elyada signature were traduced in their orthologue human version using biomaRt R package. To assess cell subtypes, an enrichment score was assigned for each gene set to each cell using UCell R package (Andreatta et al., 2021). Cell subtype was assigned based on maximum score achieved by a cell for a specific gene set. Pan cancer dataset from Han Luo et al. (Han Luo et al. 2022) (primary tumor = 148, ncells = 494610) was downloaded from Gene expression Omnibus (accession No.) together with annotation metadata. sMEK signature enrichment score was computed on dataset cells with UCell package (Andreatta et al., 2021).
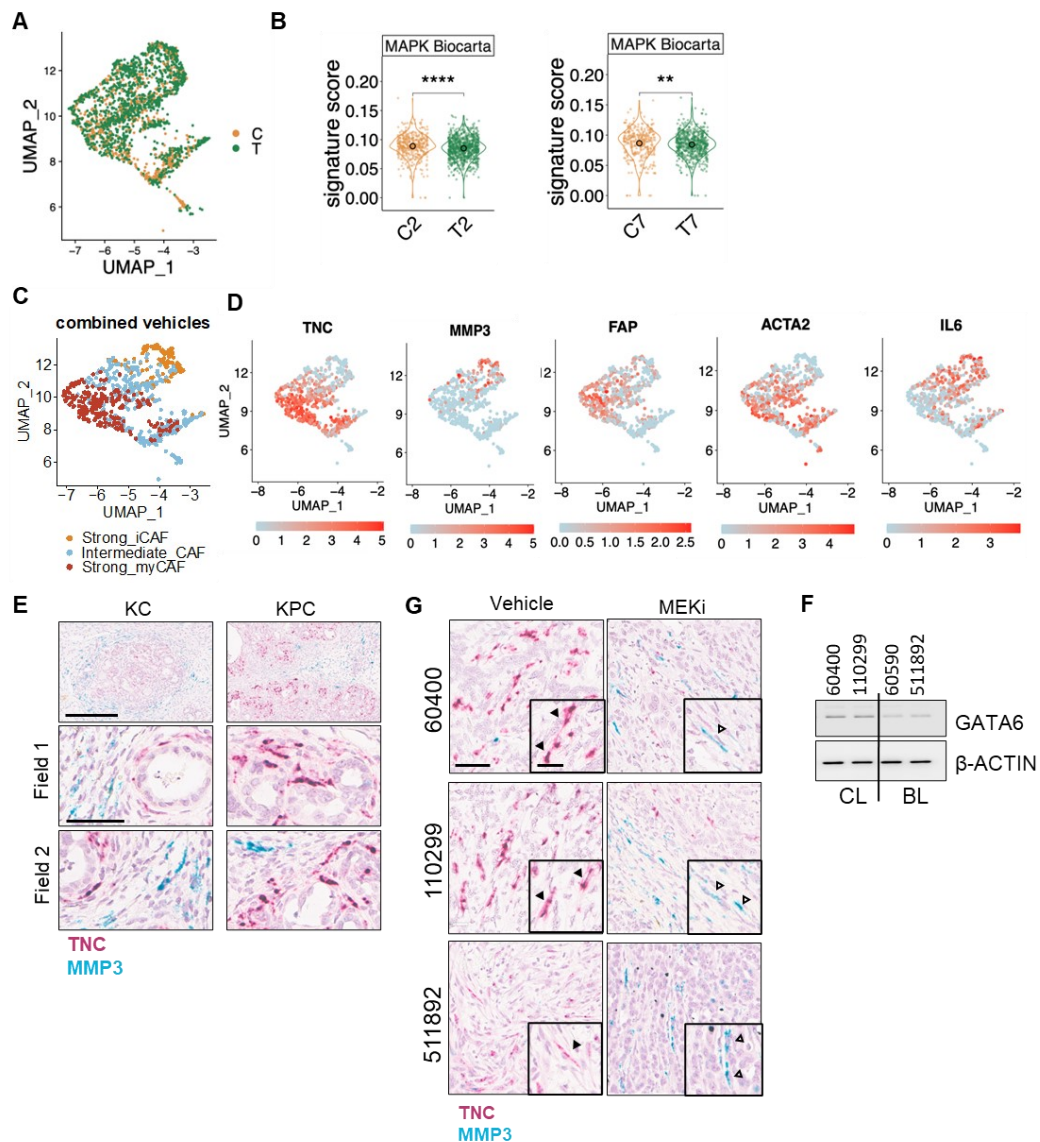
SUPPLEMENTARY FIGURES
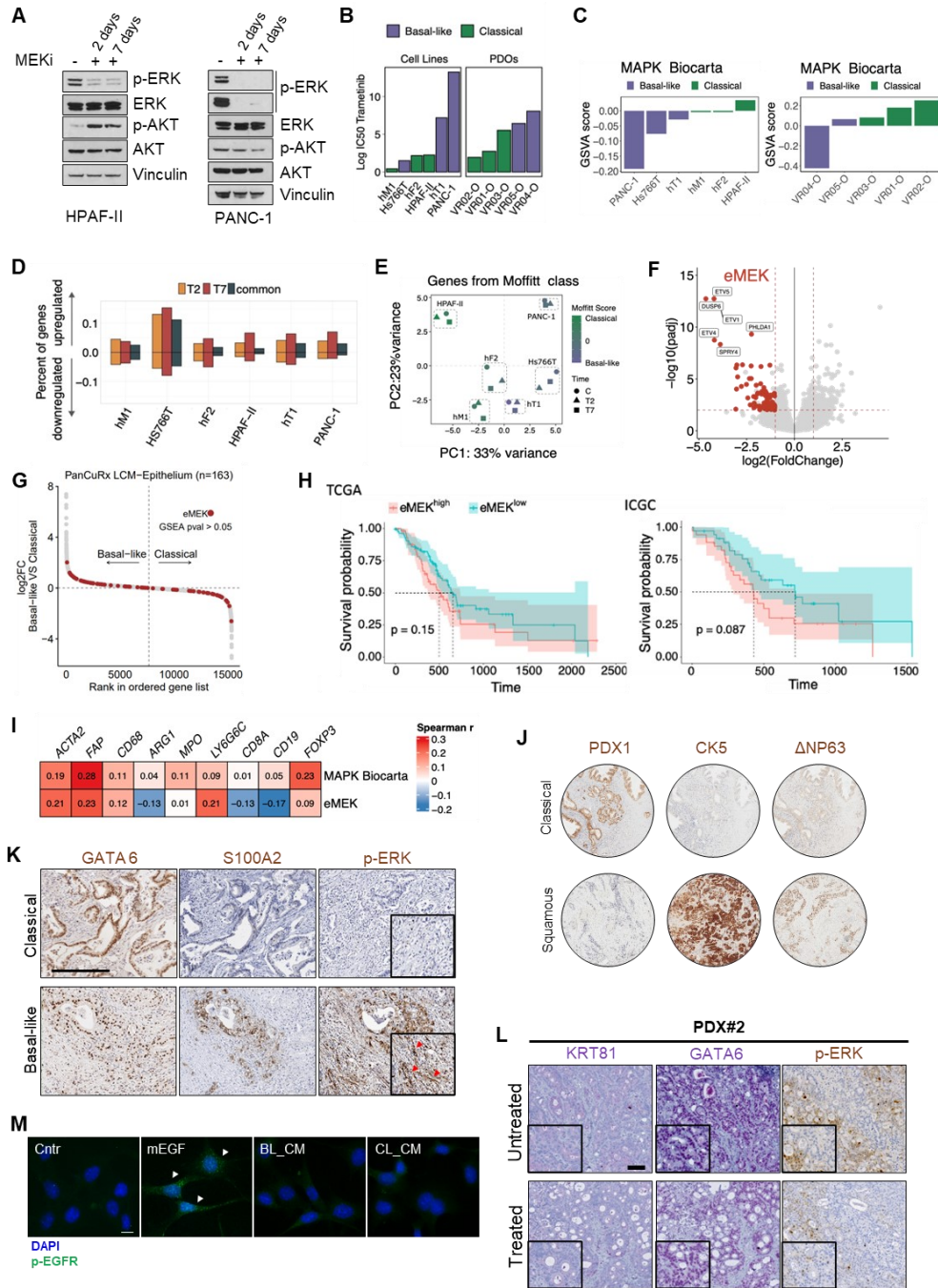
Supplementary Figure 1: Short-term MEK inhibition does not affect epithelial subtype A Immunoblot analyses of p-ERK, total ERK, p-AKT and total AKT in whole-cell lysate from HPAF-II (left) and PANC-1 (right) treated with either vehicle or MEKi (Trametinib) for 2 and 7 days. Vinculin was used as loading control. **B** Barplots showing the Log IC50 for Trametinib of 6 human cell lines (from left to right: hM1, Hs766T, hF2, HPAF-II, hT1, and PANC-1) and 5 human organoids (from left to right: VR02-O, VR01-

O, VR03-O, VR05-O, and VR04-O) classified as basal-like or classical according to Moffitt classification. **C** Waterfall plot showing the GSVA score for the MAPK Biocarta signature of 6 human cell lines and 5 human organoids classified as basal-like or classical according to Moffitt classification (Moffitt et al.,2015) and sorted by value, in ascending order. **D** Barplots showing the percentage of genes up- and down-regulated in 6 cell lines upon treatment with MEK inhibitor for 2 and 7 days. The grey bars display the number of genes in common between 2 and 7 days of treatment. **E** Principal component analysis (PCA) of RNA-seq data of 6 human cell lines treated with either vehicle (C) or MEK inhibitor for 2 (T2) and 7 (T7) days. The colour scale represents the score of Moffitt subtypes (Moffitt et al., 2015) (from classical to basal-like). **F** Volcano plot representing the genes down- and up-regulated upon treatment with MEKi for 2 days *in vitro.* The red dots are the genes that are part of the eMEK signature (n=89). Highlighted some of the genes with log2FC expression > 2 and adjusted *p* < 0.05. **G** Scatter plot showing the distribution of genes from the eMEK signature over the total number of genes ordered according to Moffit subtypes differential expression in the PanCuRx cohort. **H** Kaplan–Meier plot comparing the survival probability of patients from the TCGA (The Cancer Genome Atlas Research Network, 2017) (left) and ICGC (Bailey et al., 2016) (right) cohorts according to the expression of the eMEK signature. p, Log-rank (Mantel–Cox) test. **I** Heatmap showing correlation (Spearman's correlation) between gene signatures (MAPK Biocarta and eMEK) and selected gene markers for stromal populations: fibroblasts (*ACTA2, FAP*), macrophages (*CD68, ARG1*), neutrophils (*MPO, LY6G6C*), T lymphocytes (*CD8A*), B lymphocytes (*CD19*), and T reg lymphocytes (*FOXP3*). All boxes, p < 0.001. **J** Representative images of immunohistochemistry staining for PDX1, CK5, and ΔNP63 of classical (PDX1$^+$, CK5$^-$, ΔNP63$^-$) and squamous (PDX1$^-$, CK5$^+$, ΔNP63$^+$) tumours performed on human PDAC tissue macroarrays (TMA). **K** Representative images of immunohistochemistry staining for GATA6, S100A2, and p-ERK on classical and basal-like human PDAC tissues. Inserts showed 2X magnification of selected areas. Scalebar, 200 μm. Red arrows indicate p-ERK signal in stroma. **L** Representative images of immunohistochemistry for KRT81, GATA6 (purple) and p-ERK (brown) on patient derived xenograft (PDX#2) tissues treated with either vehicle or MEK inhibitor, Scalebar, 200 μm. Inserts showed 2X magnification of selected areas. **M** Representative immunofluorescence staining of p-EGFF (green) on mPSCs FBS-starved for six hours (Cntr) and treated for ten minutes with mEGF (50 ng/ml) and basal-like or classical conditioned media. Nuclei were counterstained with DAPI (blue). Scalebar, 10 μm. White arrows indicate nuclear p-EGFR signal.
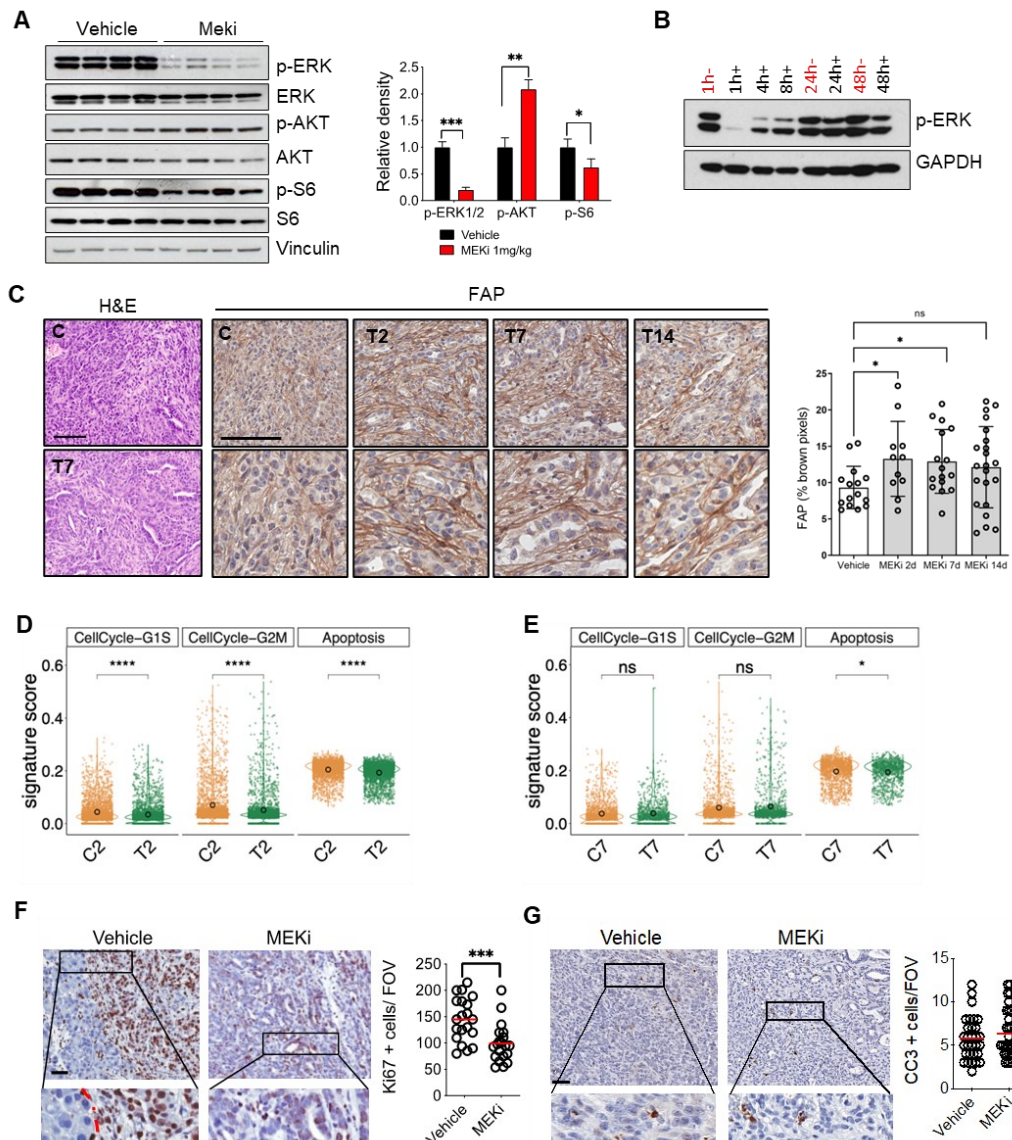
Supplementary Figure 2: MEK inhibition is efficient at 2 days of treatment and increases the stroma content *in vivo* A Immunoblot analyses of p-ERK, total ERK, p-AKT, total AKT, p-S6, and total S6 in whole-tumour lysate from mice treated for 2 days either with vehicle (n=4) or MEK inhibitor 1 mg/kg (n=4). Vinculin was used as loading control. Quantification of changes in the phosphorylated levels of proteins (p-ERK, p-AKT, and p-S6) is provided in the bar plots on the right. **B** Immunoblot analyses of p-ERK in whole-cell lysate from mPSCs treated with either vehicle (red) or MEK inhibitor. The duration of the treatment is reported in the labels on top. Vinculin was used as loading control. **C** On the left, representative Hematoxylin and Eosin staining of vehicle treated (V) and MEKi treated mice (T7) tumours for 7 days. Scalebar, 100 μm. Representative images of immunohistochemical staining for FAP of vehicle treated and MEKi treated mice tumours at different timepoints (from left to right: 2, 7, and 14 days). Scalebar, 100 μm. Lower panels show 2X magnifications of select areas. On the right, barplots showing the quantification provided as % of brown pixel per FOV. A minimum of 10 fields for each

condition have been analysed. *p < 0.05, ns as not significant as determined by Wilcoxon test. **D** Violin plots representing the signature score value (from left to right: CellCycle-G1S, CellCycle-G2M, and Apoptosis (HALLMARK)) of cells from mice treated with either vehicle (C2) or MEKi (T2) for 2 days. ****p < 0.0001 as determined by Wilcoxon test. **E** Violin plots representing the signature score value (from left to right: CellCycle-G1S, CellCycle-G2M, and Apoptosis (HALLMARK)) of cells from mice treated with either vehicle (C7) or MEKi (T7) for 7 days. *p < 0.05; ns as not significant as determined by Wilcoxon test. **F** Representative images of immunohistochemical staining for the proliferation marker Ki67 of vehicle treated (left panel) and MEKi treated tumours (right panel). On the right, quantification performed by counting Ki67 positive neoplastic cells in 5 field of visualization (FOV) for each mouse (n = 4/arm). ***, p<0.001, Student's t-test. Dashed red line separates normal pancreas (left) from PDA (right). Scalebar, 50 µm; insert magnification is 600x. **G** Representative images of immunohistochemical staining for the apoptotic marker cleaved caspase 3 (CC3) of vehicle treated (left panel) and MEKi treated tumours (right panel). On the right, quantification performed by counting CC3 positive neoplastic cells in 5 FOV for each mouse (n = 5/arm). ns, not significant Student's t-test. Scalebar, 50 µm; insert magnification is 600x.

Supplementary Figure 3: Identification of reliable markers for iCAFs and myCAFs using scRNA-seq data of mouse PDAC tumours A UMAP plot of cells from the fibroblast cluster of integrated samples from mice treated with either vehicle (C) or MEKi (T). **B** Violin plots representing the score value for MAPK Biocarta signature of cells from mice treated with either vehicle or MEKi for 2 (left) and 7 (right) days. ****p < 0.0001; **p < 0.01 as determined by Wilcoxon test. **C** UMAP plot of cells from the fibroblast cluster representing the CAFs subtype for each cell (classified as strong myCAFs, intermediate, or strong iCAFs using Elyada's classification (Elyada et al.,2019)) from vehicle treated mice. **D** UMAP plot of cells from the fibroblast cluster representing the score for selected markers (*TNC, MMP3, FAP, ACTA2,* and *IL6*) for each cell from vehicle treated mice. **E** Representative images of *in situ* hybridization showing expression of *TNC* (red; myCAFs) and *MMP3* (green; iCAFs) genes on tissue from KC and KPC mice. Scalebar, 300 μm. Lower panels show magnification of 2 fields. Scalebar, 60 μm. **F** Immunoblot analysis of GATA6 on whole cell lysate of 60400, 110299, 60590, and 511892 murine cell lines. β-ACTIN was used as loading control. **G** Representative images of *in situ* hybridization showing expression of *TNC* (red; myCAFs) and *MMP3* (green; iCAFs)

genes on PDAC tissue from mice treated with either vehicle (V) or MEKi for 2 days (T2). The upper panel shows the PDAC tissue derived from orthotopic transplantation of the classical murine cell line 60400, the middle panel shows the PDAC tissue derived from orthotopic transplantation of the classical murine cell line 110299, while the lower panel shows the PDAC tissue derived from orthotopic transplantation of the classical murine cell line 511892. Scalebar, 60 μm. Insert showed a 2X magnification of selected areas. Black arrowheads indicate myCAFs, while white arrowheads point iCAFs.
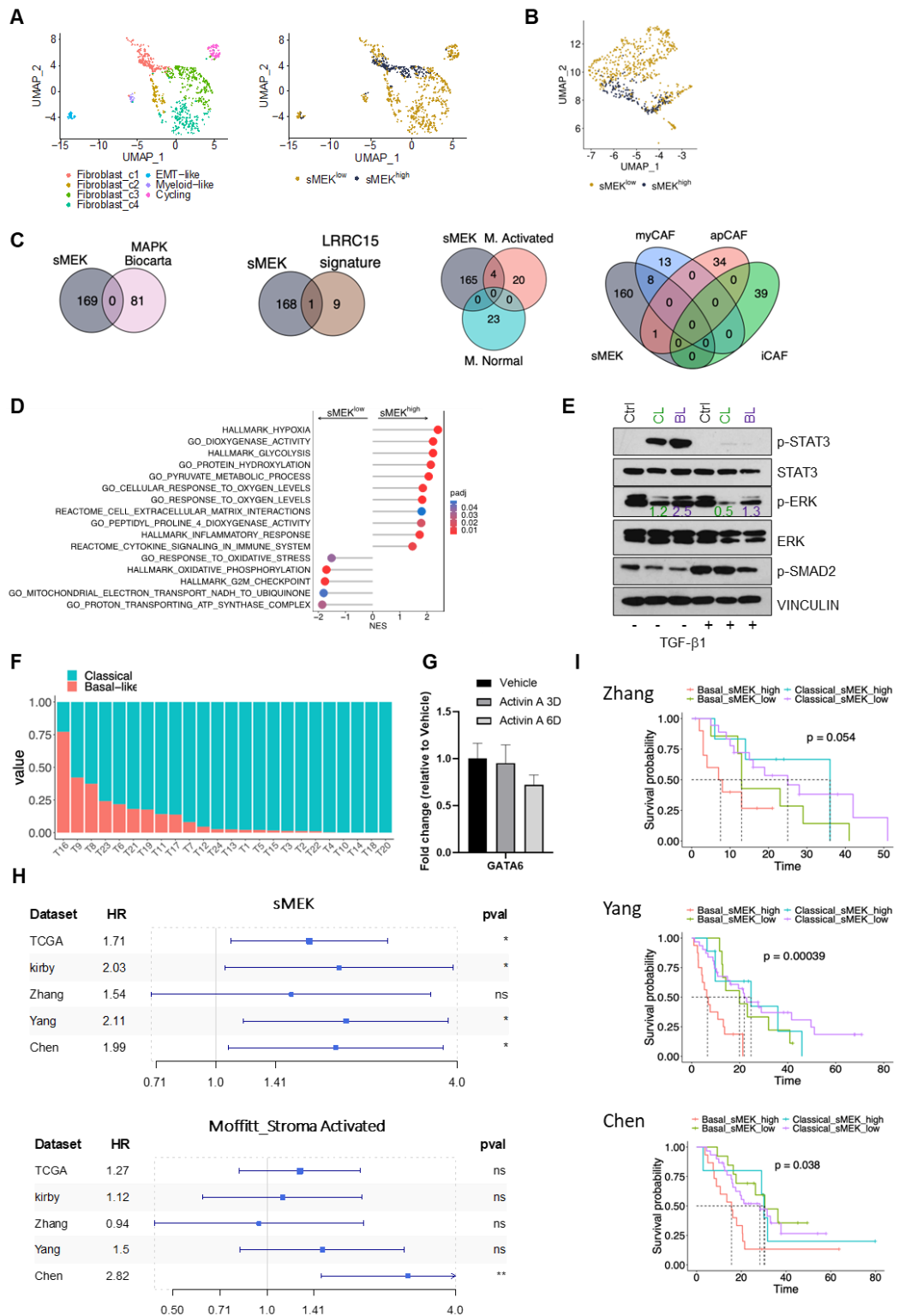
Supplementary Figure 4: Combination of the Basal-like and the sMEK signatures identify patients with poor prognosis A On the left, UMAP plot of fibroblast compartment after subclustering. Different cell type clusters are color-coded. On the right, UMAP visualization of cells from the fibroblast cluster stratified according to the sMEK signature (divided as high and low) from mice treated with vehicle for 2 and 7 days. **B**

UMAP plot of cells from the fibroblast cluster stratified according to the first 25 genes of the sMEK signature (divided as high and low) from mice treated with vehicle for 2 and 7 days. **C** Venn diagrams showing the number of genes of the sMEK signature that overlap with signatures reported in literature. From left to right: MAPK Biocarta, LRCC15 signature (Dominguez et al.,2020), Moffitt activated (Moffitt et al., 2015), and Elyada's CAFs subpopulations (myCAFs, iCAFs, and apCAFs (Elyada et al.,2019)). **D** EnrichR pathway analysis of significantly up-regulated pathways in sMEK^{high} (right) and sMEK^{low} (left) fibroblasts. **E** Immunoblot analyses of p-ERK, total ERK, p-STAT3, total STAT3 and p-SMAD2 in whole-cell lysate from mPSCs either untreated or pre-treated with TGFβ1 (5 ng/ml) for 48 hours and additionally treated with conditioned media from a classical and a basal-like cell line for 1 hour. Vinculin was used as loading control. The quantification is reported as numeric values on the blot. **F** Barplots showing the percentage of cells of the epithelial cluster classified according to Moffitt molecular classification (Moffitt et al.,2015) in samples of the Peng et al. cohort (Peng et al., 2019). Patients are ordered accordingly to decreasing basal-like cells content. **G** Barplots showing the fold change in expression of *GATA6* in Hs766t treated with Activin A (100 ng/ml) for 3 and 6 days. **H** Forest plots showing the hazard ratio for the sMEK signature (upper panel) and the Stroma Activated signature from Moffitt et al. (Moffitt et al.,2015) (lower panel) in 5 cohorts of human PDAC (TCGA (The Cancer Genome Atlas Research Network, 2017), Kirby et al. (Kirby et al., 2016), Zhang et al (Zhang et al., 2016), Yang et al. (Yang et al., 2016), and Chen et al (Chen et al., 2015)). *p<0.05; **p < 0.01; ns as not significant as determined by Wilcoxon test. **I** Combined Kaplan-Meier survival analysis comparing the survival probability of patients from 3 cohort (Zhang et al. (Zhang et al., 2016), Yang et al. (Yang et al., 2016), and Chen et al. (Chen et al., 2015)) according to the expression of the sMEK signature combined with Moffitt's molecular subtypes (basal-like, classical) (Moffitt et al., 2015). p, Log-rank (Mantel–Cox) test.

REFERENCES

- Acevedo VD, Gangula RD, Freeman KW, Li R, Zhang Y, Wang F, Ayala GE, Peterson LE, Ittmann M, Spencer DM. (2007) Inducible FGFR-1 activation leads to irreversible prostate adenocarcinoma and an epithelial-to-mesenchymal transition. *Cancer Cell.* 12(6):559-71. doi: 10.1016/j.ccr.2007.11.004.

- Adams CR, Htwe HH, Marsh T, Wang AL, Montoya ML, Subbaraj L, Tward AD, Bardeesy N, Perera RM. (2019) Transcriptional control of subtype switching ensures adaptation and growth of pancreatic cancer. *Elife*. 8:e45313. doi: 10.7554/eLife.45313.

- Aguirre AJ, Nowak JA, Camarda ND, Moffitt RA, …, Corcoran RB, Carter SL, Wolpin BM. (2018) Real-time Genomic Characterization of Advanced Pancreatic Cancer to Enable Precision Medicine. *Cancer Discov*. 8(9):1096-1111. doi: 10.1158/2159-8290.CD-18-0275.

- Andreatta M, Carmona SJ. (2021) UCell: Robust and scalable single-cell gene signature scoring. *Comput Struct Biotechnol J.* 19:3796-3798. doi: 10.1016/j.csbj.2021.06.043.

- Andricovich J, Perkail S, Kai Y, Casasanta N, Peng W, Tzatsos A. (2018) Loss of KDM6A Activates Super-Enhancers to Induce Gender-Specific Squamous-like Pancreatic Cancer and Confers Sensitivity to BET Inhibitors. *Cancer Cell.* 33(3):512-526.e8. doi: 10.1016/j.ccell.2018.02.003.

- Aran D, Looney AP, Liu L, Wu E, Fong V, Hsu A, Chak S, Naikawadi RP, Wolters PJ, Abate AR, Butte AJ, Bhattacharya M. (2019) Reference-based analysis of lung single-cell sequencing reveals a transitional profibrotic macrophage. *Nat Immunol*. 20(2):163-172. doi: 10.1038/s41590-018-0276-y.

- Atkinson, M. A., Campbell-Thompson, M., Kusmartseva, I. & Kaestner, K. H. (2020) Organisation of the human pancreas in health and in diabetes. *Diabetologia* vol. 63 1966–1973. doi: 10.1007/s00125-020-05203-7.

- Aung KL, Fischer SE, Denroche RE, …, Moore MJ, Gallinger S, Knox JJ. (2018) Genomics-Driven Precision Medicine for Advanced Pancreatic Cancer: Early Results from the COMPASS Trial. *Clin Cancer Res*. 24(6):1344-1354. doi: 10.1158/1078-0432.CCR-17-2994.

- Avery D, Govindaraju P, Jacob M, Todd L, Monslow J, Puré E. (2018) Extracellular matrix directs phenotypic heterogeneity of activated fibroblasts. *Matrix Biol*. 67:90-106. doi: 10.1016/j.matbio.2017.12.003.

- Bachem MG, Schneider E, Gross H, Weidenbach H, Schmid RM, Menke A, Siech M, Beger H, Grünert A, Adler G. (1998) Identification, culture, and characterization of pancreatic stellate cells in rats and humans. *Gastroenterology*. 115(2):421-32. doi: 10.1016/s0016-5085(98)70209-4.

- Bailey P, Chang DK, Nones K, Johns AL, Patch AM, Gingras MC, Miller DK, … Grimmond SM. (2016) Genomic analyses identify molecular subtypes of pancreatic cancer. *Nature*. 531(7592):47-52. doi: 10.1038/nature16965.

- Balli D, Rech AJ, Stanger BZ, Vonderheide RH. (2017) Immune Cytolytic Activity Stratifies Molecular Subsets of Human Pancreatic Cancer. *Clin Cancer Res*. 23(12):3129-3138. doi: 10.1158/1078-0432.CCR-16-2128.
- Barretina J, Caponigro G, Stransky N…, Sellers WR, Schlegel R, Garraway LA. (2012) The Cancer Cell Line Encyclopedia enables predictive modelling of anticancer drug sensitivity. *Nature*. 483(7391):603-7. doi: 10.1038/nature11003.
- Bhattacharjee S, Hamberger F, Ravichandra A, Miller M, Nair A, Affo S, Filliol A, … Schwabe RF. (2021) Tumour restriction by type I collagen opposes tumour-promoting effects of cancer-associated fibroblasts. *J Clin Invest*.131(11):e146987. doi: 10.1172/JCI146987.
- Bhushan A, Itoh N, Kato S, Thiery JP, Czernichow P, Bellusci S, Scharfmann R. (2001) Fgf10 is essential for maintaining the proliferative capacity of epithelial progenitor cells during early pancreatic organogenesis. *Development*. 128(24):5109-17. doi: 10.1242/dev.128.24.5109.
- Bhuva D, Smyth G, Garnham A (2023). msigdb: An ExperimentHub Package for the Molecular Signatures Database (MSigDB). R package version 1.8.0, https://davislaboratory.github.io/msigdb.
- Biffi G, Oni TE, Spielman B, Hao Y, Elyada E, Park Y, Preall J, Tuveson DA. (2019) IL1-Induced JAK/STAT Signaling Is Antagonized by TGFβ to Shape CAF Heterogeneity in Pancreatic Ductal Adenocarcinoma. *Cancer Discov*. 9(2):282-301. doi: 10.1158/2159-8290.CD-18-0710.
- Boj SF, Hwang CI, Baker LA, …, Clevers H, Tuveson DA. (2015) Organoid models of human and mouse ductal pancreatic cancer. *Cell*. 160(1-2):324-38. doi: 10.1016/j.cell.2014.12.021.
- Brunton H, Caligiuri G, Cunningham R, …, Bailey PJ, Biankin AV. (2020) HNF4A and GATA6 Loss Reveals Therapeutically Actionable Subtypes in Pancreatic Cancer. *Cell Rep*. 31(6):107625. doi: 10.1016/j.celrep.2020.107625.
- Buechler MB, Pradhan RN, Krishnamurty AT, Cox C, Calviello AK, Wang AW, Yang YA, Tam L, Caothien R, Roose-Girma M, Modrusan Z, Arron JR, Bourgon R, Müller S, Turley SJ. (2021) Cross-tissue organization of the fibroblast lineage. *Nature*. 593(7860):575-579. doi: 10.1038/s41586-021-03549-5.
- Cancer Genome Atlas Research Network. (2017) Integrated Genomic Characterization of Pancreatic Ductal Adenocarcinoma. *Cancer Cell*. 32(2):185-203.e13. doi: 10.1016/j.ccell.2017.07.007.
- Candido JB, Morton JP, Bailey P, …, Balkwill FR, Sansom OJ. (2018) CSF1R+ Macrophages Sustain Pancreatic Tumor Growth through T Cell Suppression and Maintenance of Key Gene Programs that Define the Squamous Subtype. *Cell Rep*. 23(5):1448-1460. doi: 10.1016/j.celrep.2018.03.131.
- Catenacci DV, Junttila MR, Karrison T, Bahary N, …, Kindler HL. (2015) Randomized Phase Ib/II Study of Gemcitabine Plus Placebo or Vismodegib, a

Hedgehog Pathway Inhibitor, in Patients With Metastatic Pancreatic Cancer. *J Clin Oncol*. 33(36):4284-92. doi: 10.1200/JCO.2015.62.8719.

- Chan-Seng-Yue M, Kim JC, Wilson GW, Ng K, Figueroa EF, O'Kane GM, Connor AA, …Notta F. (2020) Transcription phenotypes of pancreatic cancer are driven by genomic events during tumour evolution. *Nat Genet*. 52(2):231-240. doi: 10.1038/s41588-019-0566-9.
- Chen DT, Davis-Yadley AH, Huang PY, Husain K, Centeno BA, Permuth-Wey J, Pimiento JM, Malafa M. (2015) Prognostic Fifteen-Gene Signature for Early Stage Pancreatic Ductal Adenocarcinoma. *PLoS One*. 10(8):e0133562. doi: 10.1371/journal.pone.0133562.
- Chen Y, Kim J, Yang S, Wang H, Wu CJ, Sugimoto H, LeBleu VS, Kalluri R. (2021) Type I collagen deletion in αSMA+ myofibroblasts augments immune suppression and accelerates progression of pancreatic cancer. *Cancer Cell*. 39(4):548-565.e6. doi: 10.1016/j.ccell.2021.02.007.
- Chen YI, Chang CC, Hsu MF, Jeng YM, Tien YW, Chang MC, Chang YT, Hu CM, Lee WH. (2022) Homophilic ATP1A1 binding induces activin A secretion to promote EMT of tumor cells and myofibroblast activation. *Nat Commun*. 13(1):2945. doi: 10.1038/s41467-022-30638-4.
- Collisson EA, Sadanandam A, Olson P, Gibb WJ, Truitt M, Gu S, Cooc J, Weinkle J., … Gray JW. (2011) Subtypes of pancreatic ductal adenocarcinoma and their differing responses to therapy. *Nat Med*. 17(4):500-3. doi: 10.1038/nm.2344.
- Connolly EC, Freimuth J, Akhurst RJ. (2012) Complexities of TGF-β targeted cancer therapy. *Int J Biol Sci*. 8(7):964-78. doi: 10.7150/ijbs.4564.
- Conroy T, Desseigne F, Ychou M, Bouché O, Guimbaud R, Bécouarn Y, Adenis A.,…Groupe Tumeurs Digestives of Unicancer; PRODIGE Intergroup. (2011) FOLFIRINOX versus gemcitabine for metastatic pancreatic cancer. *N Engl J Med*. 12;364(19):1817-25. doi: 10.1056/NEJMoa1011923.
- D'Agosto S, Pezzini F, Veghini L, Delfino P, Fiorini C, Temgue Tane GD, Del Curatolo A, Vicentini C, Ferrari G, Pasini D, Andreani S, Lupo F, Fiorini E, Lorenzon G, Lawlor RT, Rusev B, Malinova A, Luchini C, Milella M, Sereni E, Pea A, Bassi C, Bailey P, Scarpa A, Bria E, Corbo V. (2022) Loss of FGFR4 promotes the malignant phenotype of PDAC. *Oncogene*. 41(38):4371-4384. doi: 10.1038/s41388-022-02432-5.
- de Andrés MP, Jackson RJ, Felipe I, Zagorac S, Pilarsky C, Schlitter AM, Martinez de Villareal J, Jang GH, Costello E, Gallinger S, Ghaneh P, Greenhalf W, Knösel T, Palmer DH, Ruemmele P, Weichert W, Buechler M, Hackert T, Neoptolemos JP, Notta F, Malats N, Martinelli P, Real FX. (2023) GATA4 and GATA6 loss-of-expression is associated with extinction of the classical programme and poor outcome in pancreatic ductal adenocarcinoma. *Gut*. 72(3):535-548. doi: 10.1136/gutjnl-2021-325803.
- Diaferia GR, Balestrieri C, Prosperini E, Nicoli P, Spaggiari P, Zerbi A, Natoli G. (2016) Dissection of transcriptional and cis-regulatory control of differentiation in human pancreatic cancer. *EMBO J*. 35(6):595-617. doi: 10.15252/embj.201592404.

- Distler M, Aust D, Weitz J, Pilarsky C, Grützmann R (2014). Precursor lesions for sporadic pancreatic cancer: PanIN, IPMN, and MCN. *Biomed Res Int.* 2014:474905. doi: 10.1155/2014/474905.
- Djurec M, Graña O, Lee A, Troulé K, Espinet E, …, Guerra C, Barbacid M. (2018) Saa3 is a key mediator of the protumorigenic properties of cancer-associated fibroblasts in pancreatic tumors. *Proc Natl Acad Sci U S A.* 115(6):E1147-E1156. doi: 10.1073/pnas.1717802115.
- Dobin A, Davis CA, Schlesinger F, Drenkow J, Zaleski C, Jha S, Batut P, Chaisson M, Gingeras TR. (2013) STAR: ultrafast universal RNA-seq aligner. *Bioinformatics.* 29(1):15-21. doi: 10.1093/bioinformatics/bts635.
- Dominguez CX, Müller S, Keerthivasan S, Koeppen H, …, Turley SJ. (2020) Single-Cell RNA Sequencing Reveals Stromal Evolution into LRRC15$^+$ Myofibroblasts as a Determinant of Patient Response to Cancer Immunotherapy. *Cancer Discov.* 10(2):232-253. doi: 10.1158/2159-8290.CD-19-0644.
- Dowling RJ, Topisirovic I, Alain T, Bidinosti M, Fonseca BD, Petroulakis E, Wang X, Larsson O, Selvaraj A, Liu Y, Kozma SC, Thomas G, Sonenberg N. (2010) mTORC1-mediated cell proliferation, but not cell growth, controlled by the 4E-BPs. *Science.* 328(5982):1172-6. doi: 10.1126/science.1187532.
- Dreyer SB, Upstill-Goddard R, Paulus-Hock V, …, Bailey PJ, Biankin AV, Chang DK. (2021) Targeting DNA Damage Response and Replication Stress in Pancreatic Cancer. *Gastroenterology.* 160(1):362-377.e13. doi: 10.1053/j.gastro.2020.09.043.
- Durinck S, Spellman PT, Birney E, Huber W. (2009) Mapping identifiers for the integration of genomic datasets with the R/Bioconductor package biomaRt. *Nat Protoc.* 4(8):1184-91. doi: 10.1038/nprot.2009.97.
- Elghazi L, Cras-Méneur C, Czernichow P, Scharfmann R. (2002) Role for FGFR2IIIb-mediated signals in controlling pancreatic endocrine progenitor cell proliferation. *Proc Natl Acad Sci U S A.* 99(6):3884-9. doi: 10.1073/pnas.062321799.
- Eser S, Schnieke A, Schneider G, Saur D. (2014) Oncogenic KRAS signalling in pancreatic cancer. *Br J Cancer.* 111(5):817-22. doi: 10.1038/bjc.2014.215.
- Feig C, Gopinathan A, Neesse A, Chan DS, Cook N, Tuveson DA. (2012) The pancreas cancer microenvironment. *Clin Cancer Res.* 18(16):4266-76. doi: 10.1158/1078-0432.CCR-11-3114.
- Filippini D, Agosto S, Delfino P, Simbolo M, Piro G, Rusev B, Veghini L, Cantù C, Lupo F, Ugel S, De Sanctis F, Bronte V, Milella M, Tortora G, Scarpa A, Carbone C, Corbo V. (2019) Immunoevolution of mouse pancreatic organoid isografts from preinvasive to metastatic disease. *Sci Rep.* 9(1):12286. doi: 10.1038/s41598-019-48663-7.
- Forsthuber A, Korosec A, Jacob T, …, Kasper M, M. Lichtenberger B (2023) CAF variants control the tumor-immune microenvironment and predict skin cancer malignancy *bioRxiv* .539213 doi: https://doi.org/10.1101/2023.05.03.539213.

- Frattini V, Pagnotta SM, Tala, Fan JJ, …, Lasorella A, Iavarone A. (2018) A metabolic function of FGFR3-TACC3 gene fusions in cancer. *Nature.* 553(7687):222-227. doi: 10.1038/nature25171.
- Galbo PM Jr, Zang X, Zheng D. (2021) Molecular Features of Cancer-associated Fibroblast Subtypes and their Implication on Cancer Pathogenesis, Prognosis, and Immunotherapy Resistance. *Clin Cancer Res*. 27(9):2636-2647. doi: 10.1158/1078-0432.CCR-20-4226.
- Garcia PE, Adoumie M, Kim EC, Zhang Y, …, Pasca di Magliano M. (2020) Differential Contribution of Pancreatic Fibroblast Subsets to the Pancreatic Cancer Stroma. *Cell Mol Gastroenterol Hepatol*. 10(3):581-599. doi: 10.1016/j.jcmgh.2020.05.004.
- Gil Y R, Sánchez P J, Muñoz Velasco R, García García A, Sánchez-Arévalo Lobo VJ.(2021) Molecular Alterations in Pancreatic Cancer: Transfer to the Clinic. *Int J Mol Sci*. 22(4):2077. doi: 10.3390/ijms22042077.
- Gobbi PG, Bergonzi M, Comelli M, Villano L, Pozzoli D, Vanoli A, Dionigi P. (2013) The prognostic role of time to diagnosis and presenting symptoms in patients with pancreatic cancer. *Cancer Epidemiol* 37(2):186-90. doi: 10.1016/j.canep.2012.12.002.
- Godfrey LK, Forster J, Liffers S-T, Schröder C, Köster J, Henschel L,…, Siveke JT (2022) Epigenetic plasticity via adaptive DNA hypermethylation and clonal expansion underlie resistance to oncogenic pathway inhibition in pancreatic cancer. *bioRxiv*. Doi: 10.1101/2022.05.20.492826.
- Gonçalves CA, Larsen M, Jung S, Stratmann J, …, Grapin-Botton A. (2021) A 3D system to model human pancreas development and its reference single-cell transcriptome atlas identify signaling pathways required for progenitor expansion. *Nat Commun*. 12(1):3144. doi: 10.1038/s41467-021-23295-6.
- Grün D, Muraro MJ, Boisset JC, Wiebrands K, Lyubimova A, Dharmadhikari G, van den Born M, van Es J, Jansen E, Clevers H, de Koning EJP, van Oudenaarden A. (2016) De Novo Prediction of Stem Cell Identity using Single-Cell Transcriptome Data. *Cell Stem Cell*. 19(2):266-277. doi: 10.1016/j.stem.2016.05.010.
- Grünwald BT, Devisme A, Andrieux G, Vyas F, Aliar K, McCloskey CW, … Khokha R. (2021) Spatially confined sub-tumor microenvironments in pancreatic cancer. *Cell.* 184(22):5577-5592.e18. doi: 10.1016/j.cell.2021.09.022.
- Guagnano V, Furet P, Spanka C, Bordas V, Le Douget M, Stamm C, Brueggen J, Jensen MR, Schnell C, Schmid H, Wartmann M, Berghausen J, Drueckes P, Zimmerlin A, Bussiere D, Murray J, Graus Porta D. (2011) Discovery of 3-(2,6-dichloro-3,5-dimethoxy-phenyl)-1-{6-[4-(4-ethyl-piperazin-1-yl)-phenylamino]-pyrimidin-4-yl}-1-methyl-urea (NVP-BGJ398), a potent and selective inhibitor of the fibroblast growth factor receptor family of receptor tyrosine kinase. *J Med Chem*. 54(20):7066-83. doi: 10.1021/jm2006222.
- Gulati GS, Sikandar SS, Wesche DJ, Manjunath A, Bharadwaj A, Berger MJ, Ilagan F, Kuo AH, Hsieh RW, Cai S, Zabala M, Scheeren FA, Lobo NA, Qian D, Yu FB, Dirbas FM, Clarke MF, Newman AM. (2020) Single-cell

transcriptional diversity is a hallmark of developmental potential. *Science.* 367(6476):405-411. doi: 10.1126/science.aax0249.

- Guo J, Xie K, Zheng S. (2016) Molecular Biomarkers of Pancreatic Intraepithelial Neoplasia and Their Implications in Early Diagnosis and Therapeutic Intervention of Pancreatic Cancer. *Int J Biol Sci.* 12(3):292-301. doi: 10.7150/ijbs.14995.

- Hackeng, W. M., Hruban, R. H., Offerhaus, G. J. A. & Brosens, L. A. A. (2016) Surgical and molecular pathology of pancreatic neoplasms. *Diagnostic Pathology* vol. 11. doi: 10.1186/s13000-016-0497-z.

- Hagel M, Miduturu C, Sheets M, Rubin N, …, Kohl NE, Guzi T. (2015) First Selective Small Molecule Inhibitor of FGFR4 for the Treatment of Hepatocellular Carcinomas with an Activated FGFR4 Signaling Pathway. *Cancer Discov.* 5(4):424-37. doi: 10.1158/2159-8290.CD-14-1029.

- Halbrook CJ, Lyssiotis CA, Pasca di Magliano M, Maitra A. (2021) Pancreatic cancer: Advances and challenges. *Cell.* 186(8):1729-1754. doi: 10.1016/j.cell.2023.02.014.

- Hallin J, Engstrom LD, Hargis L, Calinisan A, Aranda R, …, Christensen JG. (2020) The KRASG12C Inhibitor MRTX849 Provides Insight toward Therapeutic Susceptibility of KRAS-Mutant Cancers in Mouse Models and Patients. *Cancer Discov.* 10(1):54-71. doi: 10.1158/2159-8290.CD-19-1167.

- Han L, Wu Y, Fang K, Sweeney S, Roesner UK, …, Ostrowski MC, Leone G. (2023) The splanchnic mesenchyme is the tissue of origin for pancreatic fibroblasts during homeostasis and tumorigenesis. *Nat Commun.* 14(1):1. doi: 10.1038/s41467-022-34464-6.

- Hänzelmann S, Castelo R, Guinney J. (2013) GSVA: gene set variation analysis for microarray and RNA-seq data. *BMC Bioinformatics.* 14:7. doi: 10.1186/1471-2105-14-7.

- Hao Y, Hao S, Andersen-Nissen E, …, Gottardo R, Smibert P, Satija R. (2021) Integrated analysis of multimodal single-cell data. *Cell.* 84(13):3573-3587.e29. doi: 10.1016/j.cell.2021.04.048.

- Hayashi A, Fan J, Chen R, Ho YJ, …, Iacobuzio-Donahue CA. (2020) A unifying paradigm for transcriptional heterogeneity and squamous features in pancreatic ductal adenocarcinoma. *Nat Cancer.* 1(1):59-74. doi: 10.1038/s43018-019-0010-1.

- Hebrok M, Kim SK, Melton DA. (1998) Notochord repression of endodermal Sonic hedgehog permits pancreas development. *Genes Dev.* 12(11):1705-13. doi: 10.1101/gad.12.11.1705.

- Helms EJ, Berry MW, Chaw RC, DuFort CC, Sun D, …, Hingorani SR, Sherman MH. (2022) Mesenchymal Lineage Heterogeneity Underlies Nonredundant Functions of Pancreatic Cancer-Associated Fibroblasts. *Cancer Discov.* 12(2):484-501. doi: 10.1158/2159-8290.CD-21-0601.

- Hezel AF, Kimmelman AC, Stanger BZ, Bardeesy N, Depinho RA. (2006) Genetics and biology of pancreatic ductal adenocarcinoma. *Genes Dev.* 15;20(10):1218-49. doi: 10.1101/gad.1415606.

- Hingorani SR, Petricoin EF, Maitra A, Rajapakse V, King C, Jacobetz MA, Ross S, Conrads TP, Veenstra TD, Hitt BA, Kawaguchi Y, Johann D, Liotta LA, Crawford HC, Putt ME, Jacks T, Wright CV, Hruban RH, Lowy AM, Tuveson DA. (2003) Preinvasive and invasive ductal pancreatic cancer and its early detection in the mouse. *Cancer Cell*. 4(6):437-50. doi: 10.1016/s1535-6108(03)00309-x.

- Hingorani SR, Wang L, Multani AS, Combs C, Deramaudt TB, Hruban RH, Rustgi AK, Chang S, Tuveson DA. (2005) Trp53R172H and KrasG12D cooperate to promote chromosomal instability and widely metastatic pancreatic ductal adenocarcinoma in mice. *Cancer Cell*. 7(5):469-83. doi: 10.1016/j.ccr.2005.04.023.

- Ho WJ, Jaffee EM, Zheng L. (2020) The tumour microenvironment in pancreatic cancer - clinical challenges and opportunities. *Nat Rev Clin Oncol.* 17(9):527-540. doi: 10.1038/s41571-020-0363-5.

- Hruban RH, Adsay NV, Albores-Saavedra J, Compton C, Garrett ES, Goodman SN., … Offerhaus GJ. (2001) Pancreatic intraepithelial neoplasia: a new nomenclature and classification system for pancreatic duct lesions. *Am J Surg Pathol*. 25(5):579-86. doi: 10.1097/00000478-200105000-00003.

- Hruban RH, Maitra A, Goggins M. (2008) Update on pancreatic intraepithelial neoplasia. *Int J Clin Exp Pathol*. 1(4):306-16

- Huang H, Wang Z, Zhang Y, Pradhan RN, Ganguly D, Chandra R, Murimwa G, Wright S, Gu X, Maddipati R, Müller S, Turley SJ, Brekken RA. (2022) Mesothelial cell-derived antigen-presenting cancer-associated fibroblasts induce expansion of regulatory T cells in pancreatic cancer. *Cancer Cell*. 40(6):656-673.e7. doi: 10.1016/j.ccell.2022.04.011.

- Huch M, Bonfanti P, Boj SF, Sato T, Loomans CJ, van de Wetering M, Sojoodi M, Li VS, Schuijers J, Gracanin A, Ringnalda F, Begthel H, Hamer K, Mulder J, van Es JH, de Koning E, Vries RG, Heimberg H, Clevers H. (2013) Unlimited in vitro expansion of adult bi-potent pancreas progenitors through the Lgr5/R-spondin axis. *EMBO J*. 32(20):2708-21. doi: 10.1038/emboj.2013.204.

- Hutton C, Heider F, Blanco-Gomez A, Banyard A, Kononov A, Zhang X, … Jørgensen C. (2021) Single-cell analysis defines a pancreatic fibroblast lineage that supports anti-tumor immunity. *Cancer Cell.* 39(9):1227-1244.e20. doi: 10.1016/j.ccell.2021.06.017.

- Hwang WL, Jagadeesh KA, …, Ting DT, Jacks T, Regev A. (2022) Single-nucleus and spatial transcriptome profiling of pancreatic cancer identifies multicellular dynamics associated with neoadjuvant treatment. *Nat Genet*. 54(8):1178-1191. doi: 10.1038/s41588-022-01134-8.

- Ichihara R, Shiraki Y, Mizutani Y, Iida T, Miyai Y, Esaki N, Kato A, Mii S, Ando R, Hayashi M, Takami H, Fujii T, Takahashi M, Enomoto A. (2022) Matrix remodeling-associated protein 8 is a marker of a subset of cancer-associated fibroblasts in pancreatic cancer. *Pathol Int*. 72(3):161-175. doi: 10.1111/pin.13198.

- Iida T, Mizutani Y, Esaki N, Ponik SM, …, Takahashi M, Enomoto A. (2021) Pharmacologic conversion of cancer-associated fibroblasts from a protumor phenotype to an antitumor phenotype improves the sensitivity of pancreatic cancer to chemotherapeutics. *Oncogene*. 41(19):2764-2777. doi: 10.1038/s41388-022-02288-9.
- Jacobetz MA, Chan DS, Neesse A, Bapiro TE, Cook N, …, Skepper JN, Tuveson DA. (2013) Hyaluronan impairs vascular function and drug delivery in a mouse model of pancreatic cancer. *Gut*. 62(1):112-20. doi: 10.1136/gutjnl-2012-302529.
- Jones S, Zhang X, Parsons DW, Lin JC, Leary RJ, Angenendt P, Mankoo P, … Kinzler KW. (2008) Core signaling pathways in human pancreatic cancers revealed by global genomic analyses. *Science*. 321(5897):1801-6. doi: 10.1126/science.1164368.
- Juiz N, Elkaoutari A, Bigonnet M, Gayet O, Roques J, Nicolle R, Iovanna J, Dusetti N. (2020) Basal-like and classical cells coexist in pancreatic cancer revealed by single-cell analysis on biopsy-derived pancreatic cancer organoids from the classical subtype. *FASEB J.* 34(9):12214-12228. doi: 10.1096/fj.202000363RR.
- Kalisz M, Bernardo E, Beucher A, Maestro MA, …, Real FX, Ferrer J. (2020) HNF1A recruits KDM6A to activate differentiated acinar cell programs that suppress pancreatic cancer. *EMBO J.* 39(9):e102808. doi: 10.15252/embj.2019102808.
- Kalluri R, Zeisberg M. (2006) Fibroblasts in cancer. *Nat Rev Cancer* 6(5):392-401. doi: 10.1038/nrc1877.
- Kaufmann O, Fietze E, Mengs J, Dietel M. (2001) Value of p63 and cytokeratin 5/6 as immunohistochemical markers for the differential diagnosis of poorly differentiated and undifferentiated carcinomas. *Am J Clin Pathol*. 116(6):823-30. doi: 10.1309/21TW-2NDG-JRK4-PFJX.
- Kemp SB, Cheng N, Markosyan N, Sor R, Kim IK, Hallin J, …, Stanger BZ. (2023) Efficacy of a Small-Molecule Inhibitor of KrasG12D in Immunocompetent Models of Pancreatic Cancer. *Cancer Discov*. 13(2):298-311. doi: 10.1158/2159-8290.CD-22-1066.
- Kieffer Y, Hocine HR, Gentric G, Pelon F, Bernard C, Bourachot B, Lameiras S, Albergante L, Bonneau C, Guyard A, Tarte K, Zinovyev A, Baulande S, Zalcman G, Vincent-Salomon A, Mechta-Grigoriou F. (2020) Single-Cell Analysis Reveals Fibroblast Clusters Linked to Immunotherapy Resistance in Cancer. *Cancer Discov*. 10(9):1330-1351. doi: 10.1158/2159-8290.CD-19-1384.
- Kirby MK, Ramaker RC, Gertz J, Davis NS, Johnston BE, Oliver PG, Sexton KC, Greeno EW, Christein JD, Heslin MJ, …, Myers RM. (2016) RNA sequencing of pancreatic adenocarcinoma tumors yields novel expression patterns associated with long-term survival and reveals a role for ANGPTL4. *Mol Oncol*. 10(8):1169-82. doi: 10.1016/j.molonc.2016.05.004.
- Kitai H, Ebi H, Tomida S, Floros KV, Kotani H, Adachi Y, Oizumi S, Nishimura M, Faber AC, Yano S. (2016) Epithelial-to-Mesenchymal

Transition Defines Feedback Activation of Receptor Tyrosine Kinase Signaling Induced by MEK Inhibition in KRAS-Mutant Lung Cancer. *Cancer Discov.* 6(7):754-69. doi: 10.1158/2159-8290.CD-15-1377.

- Klein, A. P. (2021) Pancreatic cancer epidemiology: understanding the role of lifestyle and inherited risk factors. *Nature Reviews Gastroenterology and Hepatology* vol. 18 493–502 doi: 10.1038/s41575-021-00457-x.

- Kloesch B, Ionasz V, Paliwal S, Hruschka N, Martinez de Villarreal J, Öllinger R, Mueller S, Dienes HP, Schindl M, Gruber ES, Stift J, Herndler-Brandstetter D, Lomberk GA, Seidler B, Saur D, Rad R, Urrutia RA, Real FX, Martinelli P. (2022) A GATA6-centred gene regulatory network involving HNFs and ΔNp63 controls plasticity and immune escape in pancreatic cancer. *Gut.* 71(4):766-777. doi: 10.1136/gutjnl-2020-321397.

- Korsunsky I, Millard N, Fan J, Slowikowski K, Zhang F, Wei K, Baglaenko Y, Brenner M, Loh PR, Raychaudhuri S. (2019) Fast, sensitive and accurate integration of single-cell data with Harmony. *Nat Methods.*16(12):1289-1296. doi: 10.1038/s41592-019-0619-0.

- Krieger TG, Le Blanc S, Jabs J, Ten FW, Ishaque N, Jechow K, Debnath O, Leonhardt CS, Giri A, Eils R, Strobel O, Conrad C. (2021) Single-cell analysis of patient-derived PDAC organoids reveals cell state heterogeneity and a conserved developmental hierarchy. *Nat Commun.* 12(1):5826. doi: 10.1038/s41467-021-26059-4.

- Krishnamurty AT, Shyer JA, Thai M, …, Müller S, Turley SJ. (2022) LRRC15+ myofibroblasts dictate the stromal setpoint to suppress tumour immunity. *Nature.* 611(7934):148-154. doi: 10.1038/s41586-022-05272-1.

- Kuleshov MV, Jones MR, Rouillard AD, Fernandez NF, Duan Q, Wang Z, Koplev S, Jenkins SL, Jagodnik KM, Lachmann A, McDermott MG, Monteiro CD, Gundersen GW, Ma'ayan A. (2016) Enrichr: a comprehensive gene set enrichment analysis web server 2016 update. *Nucleic Acids Res.* 44(W1):W90-7. doi: 10.1093/nar/gkw377.

- La Manno G, Soldatov R, Zeisel A, Braun E, Hochgerner H, Petukhov V, Lidschreiber K, Kastriti ME, Lönnerberg P, Furlan A, Fan J, Borm LE, Liu Z, van Bruggen D, Guo J, He X, Barker R, Sundström E, Castelo-Branco G, Cramer P, Adameyko I, Linnarsson S, Kharchenko PV. (2018) RNA velocity of single cells. *Nature.* 560(7719):494-498. doi: 10.1038/s41586-018-0414-6.

- Lee JJ, Perera RM, Wang H, Wu DC, …, Beachy PA. (2014) Stromal response to Hedgehog signaling restrains pancreatic cancer progression. *Proc Natl Acad Sci U S A.* 111(30):E3091-100. doi: 10.1073/pnas.1411679111.

- Lemmon MA, Schlessinger J. (2010) Cell signaling by receptor tyrosine kinases. *Cell.* 141(7):1117-34. doi: 10.1016/j.cell.2010.06.011.

- Lin W, Noel P, Borazanci EH, Lee J, …, Han H. (2020) Single-cell transcriptome analysis of tumor and stromal compartments of pancreatic ductal adenocarcinoma primary tumors and metastatic lesions. *Genome Med.* 12(1):80. doi: 10.1186/s13073-020-00776-9.

- Lito P, Solomon M, Li LS, Hansen R, Rosen N. (2016) Allele-specific inhibitors inactivate mutant KRAS G12C by a trapping mechanism. *Science*. 351(6273):604-8. doi: 10.1126/science.aad6204.
- Lomberk G, Blum Y, Nicolle R, Nair A, Gaonkar KS, …, Dusetti N, Iovanna J, Urrutia R. (2018) Distinct epigenetic landscapes underlie the pathobiology of pancreatic cancer subtypes. *Nat Commun*. 9(1):1978. doi: 10.1038/s41467-018-04383-6.
- Love MI, Huber W, Anders S. (2014) Moderated estimation of fold change and dispersion for RNA-seq data with DESeq2. *Genome Biol*. 15(12):550. doi: 10.1186/s13059-014-0550-8.
- Luo H, Xia X, Huang LB,…, Park J, Xu H. (2022) Pan-cancer single-cell analysis reveals the heterogeneity and plasticity of cancer-associated fibroblasts in the tumor microenvironment. *Nat Commun*. 13(1):6619. doi: 10.1038/s41467-022-34395-2.
- Lupo F, Pezzini F, Fiorini E, Adamo A, Veghini L, Bevere M, Frusteri C, Delfino P, D'Agosto S, Andreani S, Piro G, Malinova A, De Sanctis F, Pasini D, Lawlor RT, Hwang C, Carbone C, Amelio I, Bailey P, Bronte V, Tuveson D, Scarpa A, Ugel S, Corbo V. (2023) The axon guidance cue SEMA3A promotes the aggressive phenotype of basal-like PDAC *bioRxiv* .529923; doi: https://doi.org/10.1101/2023.02.25.529923.
- Ma, Z.Y, Gong, Y-F., Zhuang H-K…(2020) Pancreatic neuroendocrine tumours: A review of serum biomarkers, staging, and management. *World Journal of Gastroenterology* vol. 26 2305–2322. doi:10.3748/wjg.v26.i19.2305.
- Magee CJ, Greenhalf W, Howes N, Ghaneh P, Neoptolemos JP. (2001) Molecular pathogenesis of pancreatic ductal adenocarcinoma and clinical implications. *Surg Oncol*. 10(1-2):1-23. doi: 10.1016/s0960-7404(01)00016-0.
- Mahadevan D, Von Hoff DD. (2007) Tumor-stroma interactions in pancreatic ductal adenocarcinoma. *Mol Cancer Ther*. 6(4):1186-97. doi: 10.1158/1535-7163.MCT-06-0686.
- Maitra A, Hruban RH. (2008) Pancreatic cancer. *Annu Rev Pathol*. 3:157-88. doi: 10.1146/annurev.pathmechdis.3.121806.154305.
- Mancinelli G, Torres C, Krett N, Bauer J, Castellanos K, McKinney R, Dawson D, Guzman G, Hwang R, Grimaldo S, Grippo P, Jung B. (2021) Role of stromal activin A in human pancreatic cancer and metastasis in mice. *Sci Rep*. 11(1):7986. doi: 10.1038/s41598-021-87213-y.
- Mariathasan S, Turley SJ, Nickles D, Castiglioni A, …, Bourgon R, Powles T. (2018) TGFβ attenuates tumour response to PD-L1 blockade by contributing to exclusion of T cells. *Nature*. 554(7693):544-548. doi: 10.1038/nature25501.
- Maurer C, Holmstrom SR, He J, Laise P, Su T, Ahmed A, Hibshoosh H, Chabot JA, Oberstein PE, Sepulveda AR, Genkinger JM, Zhang J, Iuga AC, Bansal M, Califano A, Olive KP. (2019) Experimental microdissection enables functional harmonisation of pancreatic cancer subtypes. *Gut*. 68(6):1034-1043. doi: 10.1136/gutjnl-2018-317706.

- Mazur PK, Herner A, Mello SS, …, Sage J, Siveke JT. (2015) Combined inhibition of BET family proteins and histone deacetylases as a potential epigenetics-based therapy for pancreatic ductal adenocarcinoma. *Nat Med*. 21(10):1163-71. doi: 10.1038/nm.3952.
- McAndrews KM, Chen Y, Darpolor JK, Zheng X…, LeBleu VS, Kalluri R. (2022) Identification of Functional Heterogeneity of Carcinoma-Associated Fibroblasts with Distinct IL6-Mediated Therapy Resistance in Pancreatic Cancer. *Cancer Discov*. 12(6):1580-1597. doi: 10.1158/2159-8290.CD-20-1484.
- Meyers N, Gérard C, Lemaigre FP, Jacquemin P. (2020) Differential impact of the ERBB receptors EGFR and ERBB2 on the initiation of precursor lesions of pancreatic ductal adenocarcinoma. *Sci Rep*. 10(1):5241. doi: 10.1038/s41598-020-62106-8.
- Michl P, Löhr M, Neoptolemos JP, Capurso G, Rebours V, Malats N, Ollivier M, Ricciardiello L. (2021) UEG position paper on pancreatic cancer. Bringing pancreatic cancer to the 21st century: Prevent, detect, and treat the disease earlier and better. *United European Gastroenterol J.* 9(7):860-871. doi: 10.1002/ueg2.12123.
- Miyabayashi K, Baker LA, Deschênes A, Traub B, …, Park Y, Tuveson DA. (2020) Intraductal Transplantation Models of Human Pancreatic Ductal Adenocarcinoma Reveal Progressive Transition of Molecular Subtypes. *Cancer Discov*. 10(10):1566-1589. doi: 10.1158/2159-8290.CD-20-0133.
- Mizutani Y, Kobayashi H, Iida T, Asai N, Masamune A, Hara A, Esaki N, … Takahashi M. (2019) Meflin-Positive Cancer-Associated Fibroblasts Inhibit Pancreatic Carcinogenesis. *Cancer Res*. 79(20):5367-5381. doi: 10.1158/0008-5472.CAN-19-0454.
- Moffitt RA, Marayati R, Flate EL, Volmar KE, Loeza SG, Hoadley KA, Rashid NU, Williams LA, Eaton SC, Chung AH, Smyla JK, Anderson JM, Kim HJ, Bentrem DJ, Talamonti MS, Iacobuzio-Donahue CA, Hollingsworth MA, Yeh JJ. (2015) Virtual microdissection identifies distinct tumour- and stroma-specific subtypes of pancreatic ductal adenocarcinoma. *Nat Genet*. 47(10):1168-78. doi: 10.1038/ng.3398.
- Motoda N, Matsuda Y, Onda M, Ishiwata T, Uchida E, Naito Z. (2011) Overexpression of fibroblast growth factor receptor 4 in high-grade pancreatic intraepithelial neoplasia and pancreatic ductal adenocarcinoma. *Int J Oncol*. 38(1):133-43.
- Mucciolo G, Araos Henríquez J, Pinto Teles S, S. Manansala J, Jihad M, Li W, G. Lloyd E, S.W. Cheng P, Biffi G (2022) ERBB-activated myofibroblastic cancer-associated fibroblasts promote local metastasis of pancreatic cancer *bioRxiv*. 519080; doi: https://doi.org/10.1101/2022.12.05.519080.
- Muckenhuber A, Berger AK, Schlitter AM, Steiger K, …, Springfeld C, Weichert W. (2018) Pancreatic Ductal Adenocarcinoma Subtyping Using the Biomarkers Hepatocyte Nuclear Factor-1A and Cytokeratin-81 Correlates with Outcome and Treatment Response. *Clin Cancer Res*. 24(2):351-359. doi: 10.1158/1078-0432.CCR-17-2180.

- Muniraj T, Jamidar PA, Aslanian HR. (2013) Pancreatic cancer: a comprehensive review and update. *Dis Mon*. 59(11):368-402. doi: 10.1016/j.disamonth.2013.08.001.
- Muraro MJ, Dharmadhikari G, Grün D, Groen N, Dielen T, Jansen E, van Gurp L, Engelse MA, Carlotti F, de Koning EJ, van Oudenaarden A. (2016) A Single-Cell Transcriptome Atlas of the Human Pancreas. *Cell Syst*. 3(4):385-394.e3. doi: 10.1016/j.cels.2016.09.002.
- Neben CL, Lo M, Jura N, Klein OD. (2019) Feedback regulation of RTK signaling in development. *Dev Biol*. 447(1):71-89. doi: 10.1016/j.ydbio.2017.10.017.
- Nicolle R, Blum Y, Duconseil P, Vanbrugghe C, …, Iovanna J, Dusetti N. (2020) Establishment of a pancreatic adenocarcinoma molecular gradient (PAMG) that predicts the clinical outcome of pancreatic cancer. *EBioMedicine*. 57:102858. doi: 10.1016/j.ebiom.2020.102858.
- Nones K, Waddell N, Song S, …, Scarpa A, Pearson JV, Biankin AV, Grimmond SM. (2014) Genome-wide DNA methylation patterns in pancreatic ductal adenocarcinoma reveal epigenetic deregulation of SLIT-ROBO, ITGA2 and MET signaling. *Int J Cancer*. 135(5):1110-8. doi: 10.1002/ijc.28765.
- Öhlund D, Elyada E, Tuveson D. (2014) Fibroblast heterogeneity in the cancer wound. *J Exp Med*. 211(8):1503-23. doi: 10.1084/jem.20140692.
- Öhlund D, Handly-Santana A, Biffi G, Elyada E, Almeida AS, Ponz-Sarvise M, Corbo V, Oni TE, Hearn SA, Lee EJ, Chio II, Hwang CI, Tiriac H, Baker LA, Engle DD, Feig C, Kultti A, Egeblad M, Fearon DT, Crawford JM, Clevers H, Park Y, Tuveson DA. (2017) Distinct populations of inflammatory fibroblasts and myofibroblasts in pancreatic cancer. *J Exp Med*. 214(3):579-596. doi: 10.1084/jem.20162024.
- Olive KP, Jacobetz MA, Davidson CJ, Gopinathan A, …, Iacobuzio-Donahue C, Griffiths J, Tuveson DA. (2009) Inhibition of Hedgehog signaling enhances delivery of chemotherapy in a mouse model of pancreatic cancer. *Science*. 324(5933):1457-61. doi: 10.1126/science.1171362.
- Özdemir BC, Pentcheva-Hoang T, Carstens JL, …, Kalluri R. (2014) Depletion of carcinoma-associated fibroblasts and fibrosis induces immunosuppression and accelerates pancreas cancer with reduced survival. *Cancer Cell*. 25(6):719-34. doi: 10.1016/j.ccr.2014.04.005.
- Patro R, Duggal G, Love MI, Irizarry RA, Kingsford C. (2017) Salmon provides fast and bias-aware quantification of transcript expression. *Nat Methods*. 14(4):417-419. doi: 10.1038/nmeth.4197.
- Peng J, Sun BF, Chen CY, Zhou JY, …, Wu W. (2019) Single-cell RNA-seq highlights intra-tumoral heterogeneity and malignant progression in pancreatic ductal adenocarcinoma. *Cell Res*. 29(9):725-738. doi: 10.1038/s41422-019-0195-y.
- Porter RL, Magnus NKC, Thapar V, Morris R, …, Haber DA, Ting DT. (2019) Epithelial to mesenchymal plasticity and differential response to therapies in pancreatic ductal adenocarcinoma. *Proc Natl Acad Sci U S A*. 116(52):26835-26845. doi: 10.1073/pnas.1914915116.

- Principe DR, Park A, Dorman MJ, Kumar S, Viswakarma N, Rubin J, Torres C, McKinney R, Munshi HG, Grippo PJ, Rana A. (2019) TGFβ Blockade Augments PD-1 Inhibition to Promote T-Cell-Mediated Regression of Pancreatic Cancer. *Mol Cancer Ther*. 18(3):613-620. doi: 10.1158/1535-7163.MCT-18-0850.
- Provenzano PP, Cuevas C, Chang AE, Goel VK, Von Hoff DD, Hingorani SR. (2012) Enzymatic targeting of the stroma ablates physical barriers to treatment of pancreatic ductal adenocarcinoma. *Cancer Cell*. 21(3):418-29. doi: 10.1016/j.ccr.2012.01.007.
- Puleo F, Nicolle R, Blum Y, …, Maréchal R. (2018) Stratification of Pancreatic Ductal Adenocarcinomas Based on Tumour and Microenvironment Features. *Gastroenterology*. 155(6):1999-2013.e3. doi: 10.1053/j.gastro.2018.08.033.
- Raghavan S, Winter PS, Navia AW, Williams HL…, Aguirre AJ, Shalek AK. (2021) Microenvironment drives cell state, plasticity, and drug response in pancreatic cancer. *Cell*. 184(25):6119-6137.e26. doi: 10.1016/j.cell.2021.11.017.
- Rahib L, Wehner MR, Matrisian LM, Nead KT. Estimated Projection of US Cancer Incidence and Death to 2040. (2021) *JAMA Netw Open*. 4(4):e214708. doi: 10.1001/jamanetworkopen.2021.4708.
- Rajalingam K, Schreck R, Rapp UR, Albert S. (2007) Ras oncogenes and their downstream targets. *Biochim Biophys Acta*. 1773(8):1177-95. doi: 10.1016/j.bbamcr.2007.01.012.
- Raoof S, Mulford IJ, Frisco-Cabanos H, …, Engelman JA, Hata AN. (2019) Targeting FGFR overcomes EMT-mediated resistance in EGFR mutant non-small cell lung cancer. *Oncogene*. 38(37):6399-6413. doi: 10.1038/s41388-019-0887-2.
- Rhim AD, Oberstein PE, Thomas DH, …, Olive KP, Stanger BZ. (2014) Stromal elements act to restrain, rather than support, pancreatic ductal adenocarcinoma. *Cancer Cell*. 25(6):735-47. doi: 10.1016/j.ccr.2014.04.021.
- Riopel MM, Li J, Liu S, Leask A, Wang R. (2013) β1 integrin-extracellular matrix interactions are essential for maintaining exocrine pancreas architecture and function. *Lab Invest*. 93(1):31-40. doi: 10.1038/labinvest.2012.147.
- Sarkar FH, Banerjee S, Li Y. (2007) Pancreatic cancer: pathogenesis, prevention and treatment. *Toxicol Appl Pharmacol*. 224(3):326-36. doi: 10.1016/j.taap.2006.11.007.
- Sasaki N, Gomi F, Yoshimura H, Yamamoto M, Matsuda Y, Michishita M, Hatakeyama H, Kawano Y, Toyoda M, Korc M, Ishiwata T. (2020) FGFR4 Inhibitor BLU9931 Attenuates Pancreatic Cancer Cell Proliferation and Invasion While Inducing Senescence: Evidence for Senolytic Therapy Potential in Pancreatic Cancer. *Cancers (Basel)*. 12(10):2976. doi: 10.3390/cancers12102976.
- Schubert M, Klinger B, Klünemann M, …, Nils Blüthgen & Julio Saez-Rodriguez (2018) Perturbation-response genes reveal signaling footprints in cancer gene expression. *Nat Commun, 9* 20 doi: https://doi.org/10.1038/s41467-017-02391-6

- Segerstolpe Å, Palasantza A, Eliasson P, Andersson EM, Andréasson AC, Sun X, Picelli S, Sabirsh A, Clausen M, Bjursell MK, Smith DM, Kasper M, Ämmälä C, Sandberg R. (2016) Single-Cell Transcriptome Profiling of Human Pancreatic Islets in Health and Type 2 Diabetes. *Cell Metab*. 24(4):593-607. doi: 10.1016/j.cmet.2016.08.020.
- Shaashua L, Ben-Shmuel A, Pevsner-Fischer M, …, Scherz-Shouval R. (2022) BRCA mutational status shapes the stromal microenvironment of pancreatic cancer linking clusterin expression in cancer associated fibroblasts with HSF1 signaling. *Nat Commun*. 13(1):6513. doi: 10.1038/s41467-022-34081-3.
- Shah P, Ding Y, Niemczyk M, Kudla G, Plotkin JB. (2013) Rate-limiting steps in yeast protein translation. *Cell*. 153(7):1589-601. doi: 10.1016/j.cell.2013.05.049.
- Shinkawa T, Ohuchida K, Mochida Y, Sakihama K, Iwamoto C, Abe T, Ideno N, Mizuuchi Y, Shindo K, Ikenaga N, Moriyama T, Nakata K, Oda Y, Nakamura M. (2022) Subtypes in pancreatic ductal adenocarcinoma based on niche factor dependency show distinct drug treatment responses. *J Exp Clin Cancer Res*. 41(1):89. doi: 10.1186/s13046-022-02301-9.
- Siegel RL, Miller KD, Fuchs HE, Jemal A. (2022) Cancer statistics, 2022. *CA Cancer J Clin*. 72(1):7-33. doi: 10.3322/caac.21708.
- Somerville TD, Biffi G, Daßler-Plenker J, Hur SK, He XY, …, Tuveson DA, Vakoc CR. (2020) Squamous trans-differentiation of pancreatic cancer cells promotes stromal inflammation. *Elife*. 9:e53381. doi: 10.7554/eLife.53381.
- Somerville TDD, Xu Y, Miyabayashi K, Tiriac H, Cleary CR, Maia-Silva D, Milazzo JP, Tuveson DA, Vakoc CR. (2018) TP63-Mediated Enhancer Reprogramming Drives the Squamous Subtype of Pancreatic Ductal Adenocarcinoma. *Cell Rep*. 25(7):1741-1755.e7. doi: 10.1016/j.celrep.2018.10.051.
- Somerville TDD, Xu Y, Wu XS, Maia-Silva D, Hur SK, de Almeida LMN, Preall JB, Koo PK, Vakoc CR. (2020) ZBED2 is an antagonist of interferon regulatory factor 1 and modifies cell identity in pancreatic cancer. *Proc Natl Acad Sci U S A*. 117(21):11471-11482. doi: 10.1073/pnas.1921484117
- Soneson C, Love MI, Robinson MD. (2015) Differential analyses for RNA-seq: transcript-level estimates improve gene-level inferences. *F1000Res*. 4:1521. doi: 10.12688/f1000research.7563.2.
- Steele CW, Karim SA, Leach JDG, Bailey P, Upstill-Goddard R, Rishi L, Foth M, Bryson S, McDaid K, Wilson Z, Eberlein C, …, Morton JP. (2016) CXCR2 Inhibition Profoundly Suppresses Metastases and Augments Immunotherapy in Pancreatic Ductal Adenocarcinoma. Cancer Cell. 29(6):832-845. doi: 10.1016/j.ccell.2016.04.014.
- Steele NG, Biffi G, Kemp SB, …, Tuveson DA, Allen BL, Pasca di Magliano M. (2021) Inhibition of Hedgehog Signaling Alters Fibroblast Composition in Pancreatic Cancer. *Clin Cancer Res*. 27(7):2023-2037. doi: 10.1158/1078-0432.CCR-20-3715.
- Steele NG, Carpenter ES, Kemp SB, Sirihorachai VR, …, Pasca di Magliano M. (2020) Multimodal Mapping of the Tumor and Peripheral Blood Immune

Landscape in Human Pancreatic Cancer. *Nat Cancer*. 1(11):1097-1112. doi: 10.1038/s43018-020-00121-4.

- Stuart T, Butler A, Hoffman P, Hafemeister C, Papalexi E, Mauck WM 3rd, Hao Y, Stoeckius M, Smibert P, Satija R (2019). Comprehensive Integration of Single-Cell Data. *Cell*. 177(7):1888-1902.e21. doi: 10.1016/j.cell.2019.05.031.

- Subramanian A, Tamayo P, Mootha VK, Mukherjee S, Ebert BL, Gillette MA, Paulovich A, Pomeroy SL, Golub TR, Lander ES, Mesirov JP. (2005) Gene set enrichment analysis: a knowledge-based approach for interpreting genome-wide expression profiles. *Proc Natl Acad Sci U S A*. 102(43):15545-50. doi: 10.1073/pnas.0506580102.

- Szalai B, Saez-Rodriguez J. (2020) Why do pathway methods work better than they should? *FEBS Lett*. 594(24):4189-4200. doi: 10.1002/1873-3468.14011.

- Tape CJ, Ling S, Dimitriadi M, McMahon KM, …, Jørgensen C. (2016) Oncogenic KRAS Regulates Tumor Cell Signaling via Stromal Reciprocation. *Cell*. 165(4):910-20. doi: 10.1016/j.cell.2016.03.029.

- Topham JT, Karasinska JM, Lee MKC, Csizmok V, …, Renouf DJ, Schaeffer DF. (2021) Subtype-Discordant Pancreatic Ductal Adenocarcinoma Tumors Show Intermediate Clinical and Molecular Characteristics. *Clin Cancer Res*. 27(1):150-157. doi: 10.1158/1078-0432.CCR-20-2831

- Thoreen CC, Chantranupong L, Keys HR, Wang T, Gray NS, Sabatini DM. (2012) A unifying model for mTORC1-mediated regulation of mRNA translation. *Nature*. 485(7396):109-13. doi: 10.1038/nature11083.

- Tirosh I, Izar B, Prakadan SM, …, Shalek AK, Regev A, Garraway LA. (2016) Dissecting the multicellular ecosystem of metastatic melanoma by single-cell RNA-seq. *Science*. 352(6282):189-96. doi: 10.1126/science.aad0501.

- Togashi Y, Kogita A, Sakamoto H, Hayashi H, Terashima M, de Velasco MA, Sakai K, Fujita Y, Tomida S, Kitano M, Okuno K, Kudo M, Nishio K. (2015) Activin signal promotes cancer progression and is involved in cachexia in a subset of pancreatic cancer. *Cancer Lett*. 356(2 Pt B):819-27. doi: 10.1016/j.canlet.2014.10.037.

- Turner N, Grose R. (2010) Fibroblast growth factor signalling: from development to cancer. *Nat Rev Cancer*. 10(2):116-29. doi: 10.1038/nrc2780.

- Ulaganathan VK, Sperl B, Rapp UR, Ullrich A. (2015) Germline variant FGFR4 p.G388R exposes a membrane-proximal STAT3 binding site. Nature. 528(7583):570-4. doi: 10.1038/nature16449.

- Vennin C, Mélénec P, Rouet R, Nobis M, …, Cox TR, Timpson P. (2019) CAF hierarchy driven by pancreatic cancer cell p53-status creates a pro-metastatic and chemoresistant environment via perlecan. *Nat Commun*. 10(1):3637. doi: 10.1038/s41467-019-10968-6.

- Von Hoff DD, Ervin T, Arena FP, Chiorean EG, Infante J, Moore M, Seay T, …, Renschler MF.(2013) Increased survival in pancreatic cancer with nab-paclitaxel plus gemcitabine. *N Engl J Med*. 31;369(18):1691-703. doi: 10.1056/NEJMoa1304369.

- Waddell N, Pajic M, Patch AM, Chang DK, Kassahn KS, Bailey P, Johns AL, Miller D, …, Grimmond SM. (2015) Whole genomes redefine the mutational landscape of pancreatic cancer. *Nature*. 518(7540):495-501. doi: 10.1038/nature14169.
- Wang Y, Liang Y, Xu H, Zhang X, Mao T, Cui J, Yao J, Wang Y, Jiao F, Xiao X, Hu J, Xia Q, Zhang X, Wang X, Sun Y, Fu D, Shen L, Xu X, Xue J, Wang L. (2021) Single-cell analysis of pancreatic ductal adenocarcinoma identifies a novel fibroblast subtype associated with poor prognosis but better immunotherapy response. *Cell Discov*. 7(1):36. doi: 10.1038/s41421-021-00271-4.
- Waters AM, Der CJ. (2018) KRAS: The Critical Driver and Therapeutic Target for Pancreatic Cancer. *Cold Spring Harb Perspect Med*. 8(9):a031435. doi: 10.1101/cshperspect.a031435.
- Yang S, He P, Wang J, Schetter A…, Alexander HR, Hussain SP. (2016) A Novel MIF Signaling Pathway Drives the Malignant Character of Pancreatic Cancer by Targeting NR3C2. *Cancer Res*. 76(13):3838-50. doi: 10.1158/0008-5472.CAN-15-2841.
- Yi Z, Wei S, Jin L, Jeyarajan S, Yang J, Gu Y, Kim HS, Schechter S, Lu S, Paulsen MT, Bedi K, Narayanan IV, Ljungman M, Crawford HC, Pasca di Magliano M, Ge K, Dou Y, Shi J. (2022) KDM6A Regulates Cell Plasticity and Pancreatic Cancer Progression by Noncanonical Activin Pathway. *Cell Mol Gastroenterol Hepatol*. 13(2):643-667. doi: 10.1016/j.jcmgh.2021.09.014.
- Yu SY, Luan Y, Tang S, Abazarikia A, Dong R, Caffrey TC, Hollingsworth MA, Oupicky D, Kim SY. (2023) Uncovering Tumor-Promoting Roles of Activin A in Pancreatic Ductal Adenocarcinoma. *Adv Sci (Weinh)*. 10(16):e2207010. doi: 10.1002/advs.202207010.
- Zappia L, Oshlack A. (2018) Clustering trees: a visualization for evaluating clusterings at multiple resolutions. *Gigascience*. 7(7):giy083. doi: 10.1093/gigascience/giy083.
- Zhang G, Schetter A, He P, Funamizu N, Gaedcke J, Ghadimi BM, Ried T, Hassan R, Yfantis HG, Lee DH, Lacy C, Maitra A, Hanna N, Alexander HR, Hussain SP. (2012) DPEP1 inhibits tumor cell invasiveness, enhances chemosensitivity and predicts clinical outcome in pancreatic ductal adenocarcinoma. *PLoS One*. 7(2):e31507. doi: 10.1371/journal.pone.0031507.
- Zhang Q, Zeng L, Chen Y, Lian G, Qian C, Chen S, Li J, Huang K. (2016) Pancreatic Cancer Epidemiology, Detection, and Management. *Gastroenterol Res Pract*.;2016:8962321. doi: 10.1155/2016/8962321.
- Zhang W, Liu HT. (2002) MAPK signal pathways in the regulation of cell proliferation in mammalian cells. *Cell Res*. 12(1):9-18. doi: 10.1038/sj.cr.7290105.
- Zhou X, Hu K, Bailey P, Springfeld C, Roth S, …, Neoptolemos JP. (2021) Clinical Impact of Molecular Subtyping of Pancreatic Cancer. *Front Cell Dev Biol*. 9:743908. doi: 10.3389/fcell.2021.743908.